FACULDADE DE ENGENHARIA DA UNIVERSIDADE DO PORTO

Mechanical Characterization of CFRP Tubes

Afonso Manuel Calheno Costa Soares

Mestrado Integrado em Engenharia Mecânica

Supervisor: Professor Doutor António Torres Marques

Second Supervisor: Doutor Pedro Teixeira

July 23, 2021

Mechanical Characterization of CFRP Tubes

Afonso Manuel Calheno Costa Soares

Mestrado Integrado em Engenharia Mecânica

July 23, 2021

Abstract

The aerospace industry has been, since its foundation, defying the *status quo* regarding material limits, due to the need of extremely light and at the same time strong and stiff components. The most recent evolution in this path have been composite materials, which are extremely light, and have great specific stiffness and strength. However, the development of composites which challenge yesterday's limits is constant, and the work here presented is framed in this scope. While designing a new layup and selecting the fibre and matrix to be used that could withstand significant stresses with high stiffness, challenges arose for the testing procedures.

The work here presented, is focused on establishing a testing campaign for high strength and stiff CFRP tubes, and determining a setup which can test them, in this case in both bending and compression. This work must be done as there are no standards defined for determining these properties for tubes. To define these setups a study of standard ASTM D6272 (bending) and ASTM D695-15 (compression) was done, keeping in mind the fact both standards have been designed for flat specimen.

Some accessories were proposed to allow a smoother load transfer between the loading cell and the tube, with reduced crushing at the load application points. These setups were then simulated in ABAQUS^{TM} to have a prediction of the tubes' behaviour, and to assess their validity, and when acceptable results were achieved the experimental tests were performed. The experimental tests resulted in a successful testing campaign as the rupture in most specimen was valid, and the stress/strain graphics are similar for the different specimen.

Keywords: CFRP, Mechanical Properties Testing, Bending, Compression, Numerical Simulation

Resumo

Desde a sua criação, a indústria aeroespacial tem vindo a desafiar o *status quo* relativamente aos limites dos materiais dada a necessidade de componentes extremamente leves, que, ao mesmo tempo, sejam dotados de elevada rigidez e resistência mecânica. A mais recente evolução nesta direção são os materiais compósitos, que são extremamente leves e apresentam elevada resistência e rigidez específicas, no entanto, o desenvolvimento de compósitos que superem os valores máximos atingidos no passado é constante.

É neste âmbito que este trabalho se enquadra, já que ao escolher a fibra, a matriz e a orientação, o número e a espessura das camadas, por forma a que consigam suportar uma tensão elevada e apresentem uma rigidez elevada, surgem vários desafios ao nível dos testes.

O trabalho aqui apresentado foca-se no desenvolvimento de uma campanha experimental de testes para tubos de um compósito de fibra de carbono com elevada resistência e rigidez, bem como uma configuração para os ensaios, neste caso à flexão e à compressão. Este trabalho é importante devido à inexistência de normas padronizadas definidas para determinar estas propriedades para amostras tubulares. Para definir estas configurações um estudo das normas ASTM D6272 (flexão) e ASTM D695-15 (compressão) foi efetuado, tendo sempre presente que estas foram definidas para amostras planas.

Alguns acessórios foram propostos para permitir uma transferência de carga da célula de carga para o tubo mais suave, sem causar esmagamento nos pontos de aplicação de contacto. Posteriormente, estas configurações foram simulados no software ABAQUS^{TM} por forma a testar a sua validade e a prever o comportamento do tubo e, quando resultados admissíveis foram atingidos, prosseguiu-se para os testes experimentais. Estes foram bem-sucedidos, já que resultaram numa campanha experimental em que a rutura na maioria das amostras foi válida, ou seja, no centro das mesmas, e os gráficos tensão/deformação também se apresentam similares para as diferentes amostras o que retrata a precisão dos testes.

Keywords: Polímeros Reforçados com Fibra de Carbono, Ensaio de Propriedades Mecânicas, Flexão, Compressão, Simulação Numérica

Acknowledgements

First of all, I would like to thank my supervisor, Professor Doutor António Torres Marques, for helping me throughout this process, namely with all his invaluable knowledge regarding composite materials and the underlying manufacturing process, without it, this work would not have been possible.

To Frezite High Performance, for the opportunity of developing this thesis in a corporate environment in such an interesting and vibrant industry and namely to Doutor Pedro Teixeira, Eng. Nuno Vieira, Eng. José Cerqueira and Eng. Nuno Moreira for all their guidance and help throughout the project.

I would like to extend my gratitude to my family and friends who were present throughout this path.

Afonso Soares

Contents

List of Figures

List of Tables

Abbreviations

CFRP	Carbon Fibre Reinforced Polymer
FRP	Fibre Reinforced Polymer
ISO	International Organization for Standardization
ASTM	American Society for Testing and Materials
T_g	Glass Transition Temperature
T_c	Critical Temperature
FVF	Fibre Volume Fraction
θ	Winding Angle
FPF	First Ply Failure
FEA	Finite Element Analysis
FEM	Finite Element Method
G_I	Energy Release Rate for Mode I
G_{II}	Energy Release Rate for Mode II
E_t	Elasticity Modulus obtained from Tensile Tests
ν	Poisson Coefficient
E_c	Elasticity Modulus obtained from Compressive Tests
T_d	Resin Decomposition Temperature
DSC	Differential Scanning Calorimetry
TMA	Thermomechanical Analysis
DMA	Dynamic Mechanical Analysis
micro-CT	X-ray micro-Computed Tomography
SEM	Scanning Electron Microscope
DCB	Double Cantilever Beam
CDCB	Curved Double Cantilever Beam

Chapter 1

Introduction

Mankind has forever tried to achieve the unachievable, reaching for new goals and always dreaming of greater things. This feeling has remained present until today, despite the multitude of achievements and progress made. Nowadays, one of the greater challenges is to dare into Space, either to discover what has not been discovered or to gather further information on what is already known, namely the Earth, in order to improve our quality of life and to demystify the unknown.

1.1 Project Framing

The work here presented was done in partnership with Frezite High Performance (FHP) and is related to its involvement on the Copernicus Programme.

Copernicus is a programme developed by the European Space Agency to gather information on our planet and its environment. The ultimate goal of the programme is to improve European citizens' quality of life by measuring specific parameters that can be used by the appropriate authorities or service providers of each member state[1]. In order to provide this service, several antennas are going to be deployed to the Earth's orbit and each of them is going to monitor one property of our planet.

The present thesis will focus on the mechanical characterization of Carbon Fibre Reinforced Polymer tubes, namely those to be used in the supports of the expansible antenna that collects data as the ones on figure 1.1.

1.2 Objectives

This work aims at determining and conducting an experimental campaign for testing different mechanical properties of Carbon Fibre Reinforced Polymer tubes which can then be used as a methodology for assessing the material quality and the quality of the manufacturing process. This presents itself as a difficulty due to the lack of standardized tests for determining the mechanical

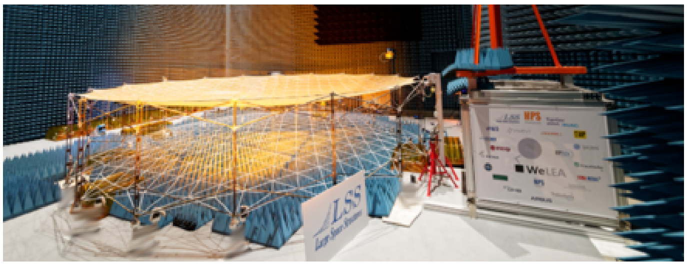

Figure 1.1: Large European Antenna [2]

properties of CFRP tubes. Both ASTM and ISO standards focus only on flat laminates, when it comes to determining mechanical properties, not having standardized tests for tubular specimen, thus, a modification of these standards should be done in order to guarantee the results' repeatability. To validate the proposed setups, numerical simulations were performed, in this case in ABAQUS^{TM}.

The tests developed in this dissertation and the assessed properties are further explained in the following chapters and have been thought to determine the properties significant for the desired application, aerospace. Regarding the numerical simulation, a study of the models for determining the lamina properties and to define the composites' failure were performed to have confidence in the proposed solutions.

1.3 Thesis Outline

In this section, the overall structure of this thesis will be presented, as it is divided into five chapters:

Chapter 1

This chapter presents the problem and defines both the objectives, as well as the context of the work done. Finally, an exposure regarding the overall structure of this document is done.

Chapter 2

In this chapter, information regarding the parameters which influence the composites' properties and the manufacturing parameters with influence on the mechanical performance of the manufactured part are exposed. Furthermore, information regarding the properties that should be measured to provide an in-depth characterisation of a composite specimen, and the respective tests are explored.

Chapter 3

This chapter is focused on the numerical simulations done (bending and uniaxial compressive tests) both to validate the proposed setups and to predict the mechanical behaviour of the tube in each test. Attention is also given to some models to define the properties of the lamina and failure models to have either a quicker or a more accurate prediction of the tubes' behaviour.

Chapter 4

Here, the results from the experimental tests are presented and a comparison between these and the numerical results is done. Afterwards, a discussion regarding the former and the differences between both is developed.

Chapter 5

In this chapter, the conclusions of the different parts of the project, and a suggestion of the work that should still be performed is presented.

Chapter 2

State of the Art

The tubes that are the scope of the present dissertation are intended for aerospace use. One of the greatest constraints this field endures is the extreme cost of sending each satellite into orbit, namely due to the amount of energy needed to withstand the Earth's gravitational force, as a comparison metric, each kilogram of matter that is sent into space costs about 50.000€[3]. Moreover, this type of application is also subjected to great stresses, thus the materials used need great specific strength and specific stiffness properties. In order to fulfill both these impositions, one of the best responding materials mankind has found are Carbon Fibre Reinforced Polymers (CFRP) and, as such, this type of material has been increasingly used in this field.

In this section, the state of the art regarding the manufacturing technique used, filament winding, the relevant mechanical properties for this application, and the tests for defining these properties will be exposed.

2.1 Composite Parameters

Several factors impact the performance of a composite. Of those, some should be highlighted[4]:

- Fibre Properties;
- Resin Properties;
- Resin Glass Transition Temperature;
- Fibre Volume Fraction;
- Geometry and orientation of the fibres;
- Void content;
- Bond strength between the fibre and the matrix;
- Residual stresses, namely due to thermal expansion[4].

2.1.1 Fibre Properties

There are a few different types of fibres that can be used while applying the filament winding technique. Naturally, if we change the type of fibre, the mechanical properties of the final FRP will be significantly different. These fibres can be[5]:

- Glass;
- Aramid;
- Carbon/Graphite;
- Boron;
- Ceramic;
- Fibres for Lightning Protection[5].

2.1.1.1 Glass Fibres

Fibreglass is often used in secondary structural aircraft applications and in helicopter rotor blades. There are several types of fibreglass. One of which is Electrical glass, or E-glass, highly appropriate for electrical applications due to its great resistance to current flow. It is made from borosilicate glass. S-glass and S2-glass are other types of glass fibre which are appropriate for structural applications, as they have a higher strength than E-glass, being produced from magnesia-alumina-silicate. The main advantages of this type of reinforcement are the lower cost, compared to other types of fibres, its increased resistance to either chemical and galvanic corrosion and its electrical properties (non-conductive)[5].

2.1.1.2 Aramid Fibres

The most well-known aramid fibres are those manufactured by *DuPont*, commercially named Kevlar®. These are light, strong and tough and due to their high impact resistance are usually used in areas prone to impact damage. Their main disadvantages are compression resistance, which is weak, and hygroscopy. Some data reported an 8% absorption of water in weight, therefore parts made of aramid fibres need to be protected from the environment. It is also a rather hard material to drill and cut and is usually used in ballistic and body armor applications. In aviation industry two types of aramid fibres are used, Kevlar®49 (high stiffness) and Kevlar®29 (low stiffness)[5].

2.1.1.3 Carbon/Graphite Fibres

Carbon and graphite fibres are both made from graphene (hexagonal) layer networks present in carbon, however, if the graphene layers are stacked with three dimensional order, we are in the presence of graphite. On the other hand, if there is only two dimensional ordering, the material at hand is carbon fibre. For graphite to be formed, a large amount of time and temperature processing is needed, making these fibres more expensive[5].

Carbon fibres present great stiffness, usually 3 to 10 times more than glass fibres, as such they are used in aircraft and aerospace applications, usually in structural parts. Their main advantages are their high specific strength and stiffness, as well as corrosion resistance. Among the disadvantages we can state the high cost and their high potential for galvanic corrosion in the adjacent metal fasteners. This material also presents a lower conductivity than aluminum, thus a lightning protection coating may be needed to protect from lightning strikes[5].

2.1.1.4 Boron Fibres

These fibres are very stiff and have a very high tensile and compressive strength, however do not flex well due to the fibres' high diameter. These fibres are commonly used in aluminium aircraft skin repairs, because of their thermal expansion, which is similar to aluminium and there is no galvanic corrosion potential. Boron fibres are difficult to use if the parent material surface has a contoured shape. These fibres are also rather expensive[5].

2.1.1.5 Ceramic Fibres

This type of fibre is only used for high-temperature applications, such as turbine blades, as these types of fibres can be used until temperatures of about 1200ºC[5].

2.1.1.6 Lightning Protection Fibres

This type of fibre is used when dealing with structures that are made of other fibres but also need to be conductive, for example aircrafts. Carbon fibres have a resistance 1,000 times greater than aluminium and epoxy resin is 1,000,000 more resistive than aluminium, thus a layer of lightning protection fibre is needed to protect the aircraft from lightning strikes. Many different materials are used for this application, such as nickel-coated graphite cloth, or metal meshes, or aluminized fibreglass[5].

2.1.2 Resin Properties

Resin is a generic term used to refer to a polymer and its chemical composition and physical properties have significant impact in the manufacturing and mechanical properties of a composite material[5].

2.1.2.1 Thermosetting Resins

These are the most diverse and broadly-used of all synthetic materials, as they are easily moulded into any shape, are compatible with most other materials and cure rapidly by heat or by hardener into an insoluble solid. These types of resins also have properties which allow them to be successfully used as adhesives[5].

However, recycling these resins is a problem that should be taken into account while designing composites with a thermosetting matrix, as it poses an extreme hardship. Thermosetting polymers are cross-linked, thus cannot be remoulded, as opposed to thermoplastics, which can be remelted. Some thermosetting polymers can be converted back to their original monomer form, as is the case with polyurethane, however, the most frequently used, such as epoxy or unsaturated polyester are not so practical to depolymerize back to their original form[6].

There are several types of thermosetting resins[5]:

- **Unsaturated Polyester Resins** - Relatively inexpensive and fast processing resins, usually used for low cost applications[5];
- **Vinyl Ester Resin** - The appearance, handling properties and curing characteristics are similar to those of unsaturated polyester resins, however vinyl ester resins have significantly better corrosion resistance and mechanical properties[5];
- **Phenolic Resin** - Resins with low flammability and low smoke characteristics[5];
- **Epoxy** - These are high strength and modulus resins, and exhibit a low level of volatiles, and excellent adhesion. They also have good chemical resistance and ease of processing, and are low shrinkage. The major disadvantages are their brittle behaviour and the decrease of their mechanical properties in the presence of moisture. The curing of this type of resins is slower than those of unsaturated polyester[5];
- **Polyimides** - These resins are suitable for high temperature environments, where thermal resistance, oxidative stability, low coefficient of thermal expansion and solvent resistance are beneficial, such as circuit boards. The cure temperatures are usually high, around 290ºC. These resins can be thermosetting or thermoplastic[5];
- **Polybenzimidazoles (PBI)** - Extremely high temperature resin[5];
- **Bismaleimides (BMI)** - This type of resin has higher temperature capability and is tougher when compared to epoxy resins. They also provide excellent performance at both ambient and elevated temperatures. The curing process is similar to that of epoxy resins[5].

2.1.2.2 Thermoplastic Resins

Thermoplastic materials can be softened repeatedly by increasing the temperature and hardened by the decrease of the same parameter. The main advantage of this group of materials is processing speed. There are some types of thermoplastic resins[5]:

- **Semicrystalline Thermoplastics** - These resins have superior toughness and good mechanical properties at high temperatures and after impact. Moreover they provide low moisture absorption. Fibres with which this resin is used include carbon, nickel-coated carbon, aramid and glass, among others. One semicrystalline thermoplastic which has great high-temperature performance and outstanding thermal and combustion characteristics, besides resistance to a wide range of solvents is PEEK[5];

- **Amorphous Thermoplastics** - The advantages of these resins depend upon the polymer. Usually the are fast and easy to process, have good mechanical properties, excellent toughness, impact strength and chemical stability, and some are capable of withstanding high temperatures. The stability results in unlimited shelf life, thus not needing the typical cold storage requirements of thermoset prepregs[5].

2.1.3 Glass Transition Temperature

When Fibre Reinforced Polymer materials are heated they tend to mollify and creep. This effect causes a significant reduction in their properties, namely their strength and stiffness[7]. The property that measures this behaviour is the glass transition temperature, T_g, usually in the range of 65-120ºC, although in space applications, special resins are used to achieve higher values. The decrease in strength and stiffness occurs in a range of temperatures and is progressive, as shown in figure 2.1, as such, in order to clearly define the interval, another temperature is recorded, the critical temperature, T_c which is the one at which the FRP loses 50% of its mechanical properties[8]. It is worth mentioning in some cases the literature does not clearly differentiate T_g and T_c[9].

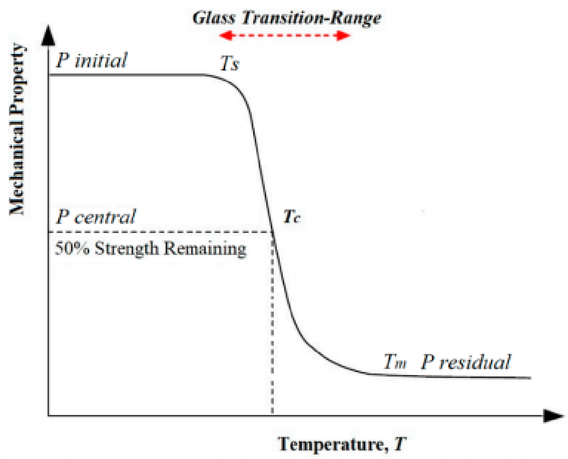

Figure 2.1: FRP mechanical properties changes with temperature[8].

In table 2.1 we can see a comparison between some resins regarding their T_g, tensile strength and modulus, and their flexural strength and modulus. These resins were chosen so that it was possible to compare three different epoxy resins, one whose temperature range was closer to ambient temperature, *Resoltech 1080S*, other which was able to operate in harsher environments with higher temperatures, as will happen in aerospace application, *Resoltech HTG160*, and a third which, besides being able to operate in environments with high temperatures, also has space heritage, *Araldite LY556*. The two other resins chosen were some that had been designed for high and

Table 2.1: Comparison of properties between some resins[10, 11, 12, 13, 14]

Resin	Resin Type	T_g	Tensile Strength	Tensile Modulus	Flexural Strength	Flexural Modulus
Resoltech 1080S	Epoxy	54-110ºC	59.9-72 MPa	2780-3450 MPa	80-116 MPa	2610-3030 MPa
Resoltech HTG160	Epoxy	160ºC	70 MPa	3000 MPa	120 MPa	3804 MPa
Araldite LY556	Epoxy	130-180ºC	45-60 MPa	2700-3000 MPa	100-140 MPa	2900-3100 MPa
Extrem Resin VH1003	Polyimide	247ºC	96 MPa	3510 MPa	159 MPa	3170 MPa
Cycoloy FR Resin CS9610	Polycarbonate/ acrylonitrile butadiene styrene one	124ºC	64 MPa	2600 MPa	98 MPa	2440 MPa

medium temperature application, *Extrem Resin VH1003* and *Cycoloy FR Resin CS9610*, respectively. All the resins were chosen in order to have good mechanical properties, as for application in composite structures, those properties are extremely important. It should be noted in the case of *Resoltech 1080S* and for *Araldite LY556*, all the parameters are expressed as an interval rather than as a definite value, this happens as these parameters vary according to the hardener used, the cure temperature and the cure time[10, 11, 12, 13, 14, 15]. The values presented in columns 4 to 7 are valid below T_g.

Robert et al.[16] studied the impact that temperature had on the mechanical properties of GFRP, by measuring the tensile, shear and the flexural strengths at different temperatures, ranging from -100ºC to 325ºC. Although this research has been done with a glass fibre reinforced polymer, rather than with CFRP, the same principle and tendency applies to this material. The results achieved by Robert et al.[16] are displayed in figures 2.2, 2.3 and 2.4, where the blue line corresponds to the observed values, while the orange one is the value according to the resin's data-sheet, here shown as a comparison metric.

2.1.4 Fibre Volume Fraction

This parameter is highly dependent on the resin used and the manufacturing process, namely the form in which the fibres are incorporated in the matrix due to the higher or lower likelihood of each process to generate voids. As an example, we can state that hand lay-up processes tend to achieve a Fibre Volume Fraction (FVF) equal to or lower than 40%, while higher quality processes can achieve FVF values of 70%[17].

The higher this parameter, the higher the mechanical properties tend to be, as if in a predetermined volume the quantity of fibre increases, the volume of resin must decrease. However, owing

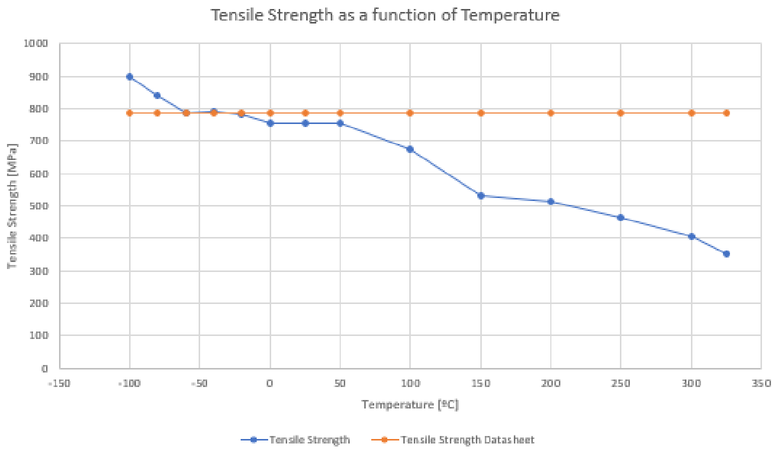

Figure 2.2: Tensile Strength as a function of Temperature[16]

to the fact the fibres must be fully coated in resin, this parameter has a maximum which must be lower than 100%[17].

If we assume a composite has been manufactured without voids, we can calculate the FVF according to equation 2.1 where ρ_c is the density of the composite, ρ_m the matrix density, ρ_f the fibre density[17], V_f is the volume of fibre and V_c is the volume of composite.

$$FVF = \frac{\rho_c - \rho_m}{\rho_f - \rho_m} = \frac{V_f}{V_c} \tag{2.1}$$

2.1.5 Fibre Orientation

The strength and stiffness of a composite structure is strongly dependent on the orientation of the fibres relative to the load, due to the anisotropic properties of composites, thus proper selection of its orientation is of extreme importance in the design phase. Composites tend to have higher properties along the fibre direction[17].

The anisotropic properties of composites can be beneficial since it is possible to optimise the design for the required loads, thus requiring less material and achieving lighter structures[17].

Another aspect worth mentioning related to composite materials is that the fibre's properties depend almost exclusively on the material supplier, not being possible to resort to heat treatments, or others, like in metals[17].

The influence that this parameter has on mechanical properties was clearly demonstrated by Naseva et al.[18] in the paper where the influence of the winding angle in the tensile strength obtained from the hoop tensile strength was studied. In this study, the material used was an epoxy resin reinforced with E-glass, nevertheless the effect occurs on all types of fibres. The study was conducted in such a way that would allow the results to be comparable so, the winding tension, winding speed, FVF and curing time and temperature were kept constant in order to have only one variable, the winding angle. On table 2.2, it is only shown the average value for the hoop tensile strength for each value of the winding angle achieved in this work.

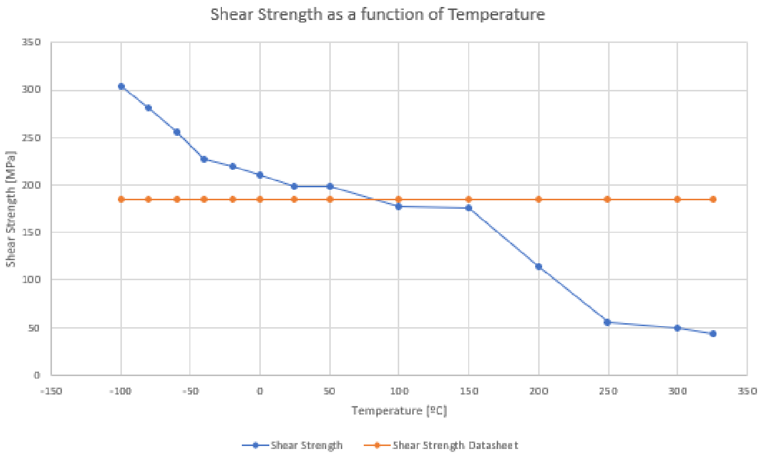

Figure 2.3: Shear Strength change with Temperature[16]

Table 2.2: Effect of fibre orientation on hoop tensile strength[18]

Winding Angle	Hoop Tensile Strength
10º	27.45 MPa
45º	277.3 MPa
90º	901.15 MPa

Marinucci et al.[19] also studied the effect different fibre orientations have on mechanical properties of filament wound CFRPs and have reached the results on table 2.3. These results were obtained by performing tests according to ASTM D3039. For this study, the authors used a composite in which the reinforcement was the *Tenax HTA 6k* carbon fibre, and the matrix was the *Vântico GY260* epoxy resin. On this table, it is also clear the impact the fibres orientation has on the performance of this material.

Table 2.3: Effect of fibre orientation on some mechanical properties[19]

Winding Angle	Tensile Strength [MPa]	Modulus of Elasticity [GPa]	Poisson Ratio
0º	2509 ± 100	153.0 ± 4.0	0.30 ± 0.01
± 10º	854 ± 45	134.0 ± 4.0	0.60 ± 0.02
± 20º	537 ± 8	83.0 ± 2.0	1.44 ± 0.02
± 30º	292 ± 3	34.0 ± 1.0	1.62 ± 0.02
± 60º	83 ± 3	10.9 ± 0.3	0.48 ± 0.04
± 70º	64 ± 1	9.7 ± 0.8	0.15 ± 0.04
± 80º	68 ± 3	9.3 ± 0.3	0.05 ± 0.02
90º	73 ± 6	10.5 ± 0.6	0.02 ± 0.01

Moreover Datta et al.[20] analysed the winding angle's influence on several properties in E-glass fibre reinforced unsaturated polyester resin tubes, namely the impact this parameter has on

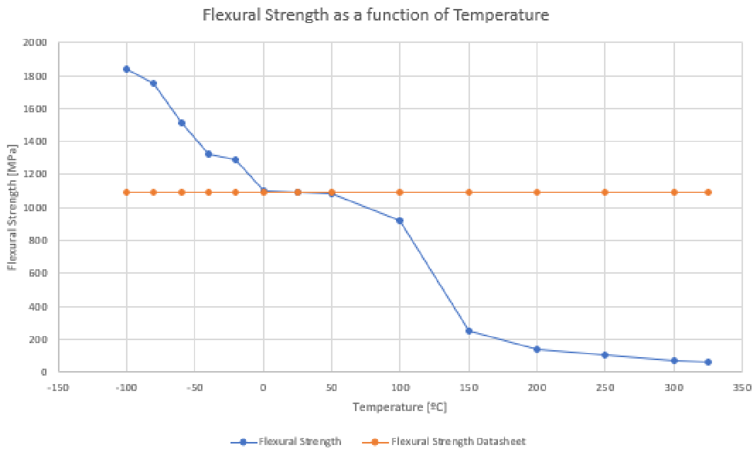

Figure 2.4: Flexural Strength as a function of Temperature[16]

flexural strength. The glass fibre used was a two ply *Goa Glass Fibre Limited 2400 tex* and the matrix was the commercial grade *General Purpose (GP)* unsaturated polyester resin. The flexural strength was measured according to ASTM D790, which is the standardized version of the common three-point bending test. The values achieved in this study are on table 2.4.

Table 2.4: Effect of fibre orientation on flexural strength[20]

		Winding Angle					
		40º	50º	60º	70º	80º	90º
Flexural strength [MPa]	Hoop	139.77	161.87	209.93	363.34	499.65	555.42
	Axial	103.21	82.22	69.49	38.49	45.52	43.71

The values of table 2.4 are also demonstrated in figures 2.5 and 2.6.

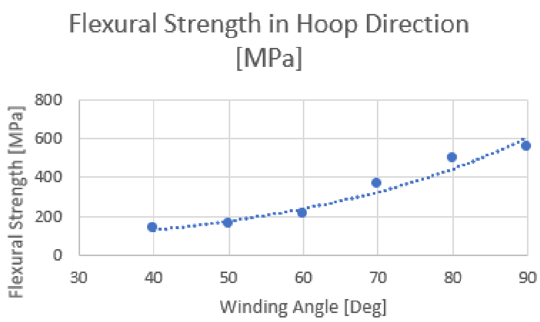

Figure 2.5: Flexural Strength in Hoop direction as a function of Winding Angle[20]

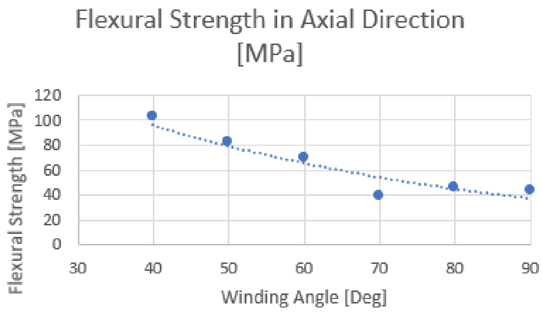

Figure 2.6: Flexural Strength in Axial direction as a function of Winding Angle[20]

2.1.6 Voids

One other important parameter is the void quantity in a CFRP. This amount is dependent on the manufacturing process, and some are more prone to void formation than others, as the main reason for this flaw is air entrapment, which usually occurs during resin flow. Nevertheless, void quantity can also be due to the gas created as a result of chemical reactions which occur during cure, or nucleation of dissolved gases in the resin[21].

Some of the parameters that have the greater impact in the formation of voids are:

- Vacuum pressure;
- Cure temperature;
- Autoclave pressure;
- Resin viscosity[22].

Voids, even at low volume fraction, have a huge impact on the mechanical performance of CFRPs[23], as is confirmed by the fact CFRP parts with a void volume fraction of more than 1% are considered unsuitable for aerospace[24]. Moreover, it has been stated that, in addition to the volume fraction, knowing the defect microstructure is important[22].

According to Zhuang[25], who studied void effects according to a fracture mechanics approach, the presence of voids has a significant impact after G_I reaches its maximum value. Its impact is influenced by both the size and location of voids, however no clear trend has been found to correlate location and G_I.

According to the same author[25], for composites with a thermosetting matrix, G_{II} increases with void size, and with the closer the void is to the delamination front.

G_I and G_{II} are the values which define the strain energy release rate, for mode I and mode II testing, respectively. This property is studied as the driving force for delamination growth, thus having extreme importance in the mechanical resistance of the CFRP tubes[25].

2.2 Filament Winding

Filament Winding is a manufacturing technology developed in the late 1960s, which is based on the creation of helical patterns. This technique is usually used for the creation of hollow composite structures by cross-weaving polymer impregnated continuous fibres around a cylindrical mandrel[4].

When manufacturing objects with this technique, continuous fibres are usually used as they ensure uniformity in the direction of the fibre arrangement. Through the use of a cylindrical mandrel, it is possible to ensure the consistency of the inside diameter of pipes. This technique also allows not using pre-impregnated fibres, which can either be seen as an advantage or a disadvantage[4].

In order to manufacture the filament wound tubes considered, Frezite High Performance relies on the wet filament winding technique. In this variant, a number of fibre rovings are pulled from creels and tensioners. These control the tension of the fibres through the liquid resin bath which contains both the resin, the hardeners and the accelerators. Before the manufacturing of the final product, the rovings must be pulled through a winding device where the excess resin is removed from them. Afterwards, the rovings can be applied around the mandrel and after all the layers been applied, cure can take place[26]. A schematic of the filament winding process is displayed in figure 2.7.

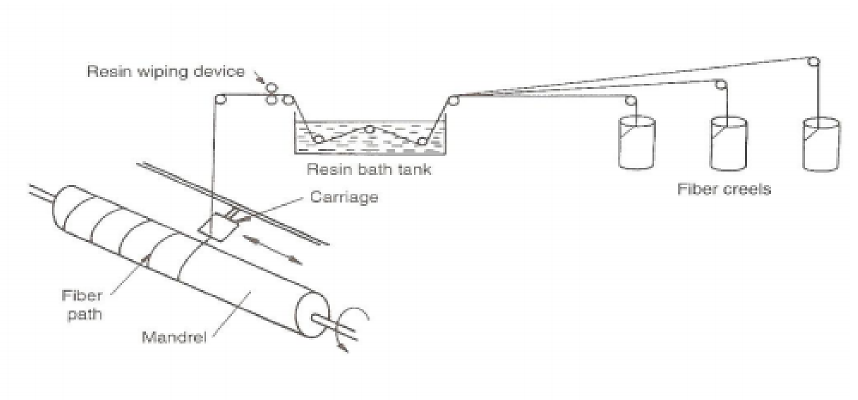

Figure 2.7: Filament Winding process schematic [26]

2.2.1 Winding Angle

This parameter, θ, relates to the angle between the fibres and the longitudinal direction. The rotation speed of the mandrel and the longitudinal speed of the head dispensing tows are the parameters which control the winding angle. This parameter typically presents an angle between 20º and 87º[4].

In order for the designer to choose the best angle for the production, the stresses induced at the pipe wall should be taken into account. The changes of longitudinal loads that may be caused by boundary conditions or changes in the operative conditions, for example, must also be taken into account as these modify the stress state into the pipe[4].

2.2.2 Winding Tension

The winding tension determines the force squeezing the roving on the winding mandrel or on the roving layers during winding, therefore the adjustment of the amount of fibres for a unitary volume through the regulation of the winding tension is possible. It also directly influences both the compaction and the alignment of the fibres[27].

This value also must be kept constant in order to guarantee the desired geometry on the final part. The deposition system should move along a critical winding trajectory, which is the one where bending and sharp direction shifts cause fibre unfastenings or speed variations during placement that cause dishomogeneities of a manufactured part. The winding trajectory should consider winding tension loosen, which is particularly evident in rectilinear segments. A convenient value for the winding tension must be chosen and it must be kept constant in order to limit the two problems stated[28].

2.2.3 Winding Speed

This parameter influences both the accuracy and the repeatability of the process to perform the winding trajectories, as the location error of the deposition head in every point of the winding trajectory increases with the increased speed. High values for the winding speed mean the robot joints jerk along the winding trajectory by increasing stresses on the rovings and vibrations on robot joints, thus the manufactured part would have different fibre distribution than the designed one and, consequently, there would be a deterioration of the structural characteristics. However, maximizing the winding speed, respecting the quality requirements, is important in order to guarantee the lowest possible cost for the product[27].

2.2.4 Advantages

The filament winding technique has diverse advantages, namely:

1. Creation of a highly repetitive pattern;
2. Possibility of obtaining a high fibre volume fraction, FVF;
3. Ease of the curing process and the removal of the need for it to happen in an autoclave or in other designated system[4];
4. Low void content;
5. Process automation[29].

2.2.5 Disadvantages

On the other hand, it also presents itself with a few disadvantages, of which some must be pointed out:

1. Limited to convex shapes;
2. The winding angle must vary gradually;
3. The mandrel could be removable and its cost must be accounted;
4. The greater tendency for voids[4].

The manufacturing parameter that has the most influence on mechanical properties of the finished tube is the winding angle[4].

2.3 Failure Mechanisms

According to the literature several failure mechanisms can occur in filament wound tubes. These mechanisms are a function of the applied axial-to-hoop stress ratio:

1. Tensile axial failure;
2. Compressive axial failure;
3. Bending failure;
4. Shear failure;
5. Weepage (When applicable);
6. Local leakage (When applicable);
7. Burst (When applicable);
8. Intralaminar cracks and interlaminar delamination;
9. Transverse micro-cracking;
10. Buckling [30, 4, 31, 29, 17].

It should be noted that weepage, local leakage and burst failure mechanisms do not apply to the case at hand, as these tubes do not hold any fluid.

Before discussing the different loads applied to CFRP tubes, it should be assessed how a composite system fails.

The ultimate strength is the point at which thousands of elementary phenomena of three types occur. These three types are[32]:

- Fibre rupture;
- Matrix crack;
- Fibre-matrix debonding[32].

However, before this extreme failure occurs, one other phenomenon should be noted, when applying load to the specimen there is a point when the resin will begin to crack away from the fibre reinforcement not aligned with the applied load. These cracks will spread through the matrix and at this point the breakdown process has started, despite the specimen still being able to withstand a greater load. This phenomenon is known as "transverse micro-cracking". In order to develop a long-lasting structure, engineers should design the composite parts so that this point is never exceeded in service[17].This phenomenon is portrayed in figure 2.8.

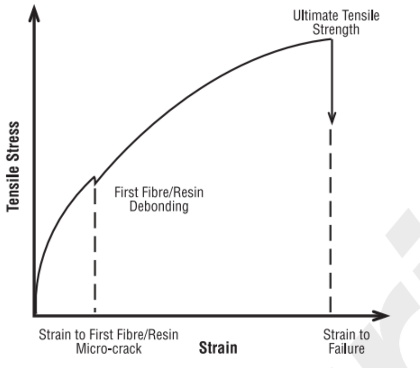

Figure 2.8: Typical FRP stress/strain graph[17]

The strain that a composite system can achieve before micro-cracking is severely influenced by the toughness and adhesive properties of the resin. For brittle resins, such as most unsaturated polyester resins, this point occurs for a strain significantly lower than the ultimate one, severely limiting the strains to which the composite can be subjected. As an example, tests have shown that for unsaturated polyester/glass woven roving laminate, micro-cracking typically occurs at 0.2% strains, with ultimate failure only occurring at 2.0% strain. This means only 10% of the ultimate strength is usable[17].

The adhesion between the resin and the fibre is generally a result of both the resin's chemistry and its compatibility with the surface treatments, usually chemical, applied to the fibres. The adhesive properties of epoxy helps composite systems achieve higher micro-cracking strains[17].

It should be mentioned, for a tensile loading, to achieve the full-mechanical properties of the fibre, the resin must be able to deform to the same extent as the fibre[17].

2.4 Failure Modes

Damage processes in composite structures often occur rapidly and with great complexity, consisting of several interacting defects[33]. Several damage evolutions and failure modes can occur in a composite structure, namely[34]:

- Matrix cracking;
- Fibre-matrix interfacial bond failure;

- Fibre breakage;
- Void growth;
- Matrix crazing;
- Delamination[34].

Matrix cracking tends to be the first form of damage that appears in composite systems, and it is not a catastrophic one. The use of thin plies is also widely accepted as a good design practice, as it is easier to manufacture laminates with no cracks, however the mismatch of elastic properties and the thickness of outer plies are also important[35]. In composite systems, the strain to failure of the fibres is much smaller than the matrix's one[36].

In general, composite structures are designed using the First Ply Failure (FPF) criterion which states the composite is considered to have failed once a single ply has failed[37]. When matrix cracking is the failure mode for FPF, the composite structure still has the ability of withstanding higher loads after the first failure, thus cannot be assumed to have failed. That being said, some properties have some modifications, specifically the Young's modulus and the coefficient of thermal expansion[37]. However, multiple cracking can produce several problems for the composite system:

1. Reduces the effective stiffness of cracked plies, causing a stress redistribution;
2. Modification of thermal expansion properties;
3. Leads to delamination between plies;
4. Allows fluid weepage in pressure vessels and allows moisture to infiltrate[37].

Depending on the properties of fibres, matrix, and the interface between the two, a fibre-matrix failure could be due to:

- Crack propagation from the fibre into the matrix, until is arrested by neighboring fibre, causing a fibre break;
- Shear yielding of the matrix until the fibre break tip, blunting the crack;
- A debond crack may grow from fibre break along the fibre-matrix interface[37].

Fibre breakage is amongst the most common failures under low velocity impact testing, due to the high stress field and indentation effects in the specimen. In this test a shear force and high bending stresses are induced in the side opposite to the impacted side of the specimen. This type of failure severely impacts the mechanical performance of the composite material, opposed to matrix cracking[38].

For glassy polymers, blends and semi-crystalline polymers with a glassy matrix, crazing is the first stage of fracture. It is a localized tensile yielding process that produces thin sheets of "crazed" material. The sheets are perpendicular to the principal stress axis. Within a craze there are fine fibrils of oriented polymer parallel to the stress axis that extend across the craze, and the continuous phase is void. The density of craze polymer is about 20% of the bulk polymer, which translates to 80% of the craze being void. Crazes eventually evolve to form cracks, and when the cracks grows significantly, the sample fails[39].

Delamination is a dangerous kind of failure as it develops inside the material, thus, it may not be obvious by looking at its surface[40]. The cause for this type of failure is high interlaminar stresses with the typically very low through-thickness strength. It occurs because of the lack of through the thickness strength of fibres, thus, the composite has to rely on the matrix, which is relatively weak, to carry the loads in that direction. This is compounded to the usual brittleness of the resin[41].

2.5 Tensile Strength

2.5.1 Ultimate Tensile Strength

In order to determine this parameter, a tensile load must be applied. The composite's response to this load is extremely dependent on the tensile stiffness and strength of the reinforcement fibres in the direction of the load[17].

According to Liebig et al.[42] in order to correctly determine the ultimate tensile strength, a traction load must be applied until failure. If at that point the specimen is damaged in a multitude of points, the ultimate tensile strength has been determined. If failure occurs in only one designated point, the longer piece of the specimen should be prepared for testing again and tested in order to determine the ultimate tensile strength. This is to evaluate if the first failure is due to the most critical defect or because the ultimate tensile strength has been reached.

Liebig et al.[42] also defend the strength under uniform stress is dominated by the largest defect. Admitting defects are randomly distributed, the larger the volume, the greater the probability of containing defects, thus the greater likelihood of the part having a lower strength. This information must be taken into account in the design phase.

In laminates, two ultimate tensile strengths can be determined, the ultimate longitudinal tensile strength and the ultimate transverse tensile strength. The difference in both is the angle between the applied load and the fibre orientation. The former refers to the load in the same direction as the fibres and the latter to a 90º angle between the fibres and the load. Therefore, while in the longitudinal direction the fibre strength and the fibre volume fraction are the main determinants of the composite strength, in the transverse direction the interface between the fibres and matrix is the main responsible for composite strength[43]. As such, a CFRP is expected to have a higher ultimate longitudinal tensile strength, typically 10 to 20 times the ultimate transverse tensile strength. From this, we can expect that for filament wound tubes the winding angle will impact the final result of the ultimate tensile strength.

When using CFRP, another important aspect is the quality of the used fibres. This is of extreme importance as carbon fibre is extremely brittle, meaning there is a significant decrease in its strength properties with the increase in defects. According to Mouritz[43] a surface crack of only 0.3-0.4μm reduces breaking strength by more than 50 %.

As reported by Adams[44], stress concentrations are much harder to predict for composite materials than they are for metals, even when relying in FEM analysis, due to the fact stiffness properties, for the first, are directionally dependent and the damage states around the holes are more complex in composite materials. As such, if the final product is hollowed, tests with hollowed specimen should be done in order to assess the ultimate tensile strength. It should also be stated in this scenario a test is only deemed valid if the failure mode is one that passes through the hole, despite this test not being standardized for tubes neither by ASTM neither by ISO.

According to the study performed by Barile et al.[45], who studied the impact temperature has on CFRP-Epoxy composites' properties with different fibre orientations, the temperature does not have a significant effect with regard to the ultimate tensile strength, namely due to the thermal stability of the reinforcement.

2.5.2 Elasticity Modulus obtained from Tensile Tests

One other important parameter to define the mechanical behaviour of a CFRP tube is the Elasticity Modulus obtained from tensile tests, E_t. This property correlates the traction loading and the correspondent displacement.

It is also extremely dependent on the temperature at which the load occurs, as discovered by Barile et al.[45] in Carbon Fibre Reinforced Epoxy, as at cold temperature (-54ºC) this parameter was approximately twice that at both hot (71ºC) or room (23ºC) temperatures. One reason given for this is the fact epoxy (the polymer in the CFRP tested) tends to become brittle at low temperatures.

2.5.3 Poisson Ratio

Poisson's ratio is an important engineering constant for determining the stress and deflection properties of materials (FRP, metals, etc.). When dealing with polymers, temperature changes or the magnitude of stresses may be enough for this parameter to change. Nevertheless, this variations are usually small enough so that the typical range of values does not affect most practical calculations[46].

When a material is stretched, its cross-sectional area changes, as well as its length. The Poisson ratio, ν is the constant relating this changes[46], according to:

$$\nu_{xy} = -\frac{\varepsilon_y}{\varepsilon_x} \tag{2.2}$$

However, due to the anisotropy of composites there are two values for the Poisson ratio where the reader's attention should focus, the major Poisson ratio and the minor Poisson ratio. The major Poisson ratio is the ratio between the transverse strain and the axial strain, when the composite is loaded in the axial direction. On the other hand, the minor Poisson ratio is the ratio between the axial strain and the transverse strain, when the composite is loaded in the transverse direction[47].

2.6 Compressive Strength

The compressive stress-strain curve describes the behaviour of a composite material, in this case, when a compressive loading is applied at its ends. This load must be applied at a low and uniform rate, so as to have an analysis as close as possible to a static one, and not a dynamic analysis. Compressive properties include compressive strength, compressive modulus, yield stress, deformation beyond yield point, and compressive strain. Nevertheless, compressive strength and modulus are the two most important ones[48].

2.6.1 Ultimate Compressive Strength

This property resembles the ultimate tensile strength, already mentioned, however in this case the load is compressive, as opposed to being tensile.

When applying a compressive load, the stiffness properties of the resin are crucial, as the resin is responsible for maintaining the fibres straight, preventing buckling[17].

Barile et al.[45] realized for CFRPs with an epoxy matrix the ultimate compressive strength is greater at cold temperature (-54ºC) when compared to either room (23ºC) or hot (71ºC) temperatures.

Asaro et al.[49] also studied the impact a combined thermal and compressive load has in FRP composites. This work indicated both the exposure time and temperature have a degrading impact on the composite and, consequently, the composite's performance, namely its strength and failure mode, especially during fire.

2.6.2 Elasticity Modulus obtained from Compressive Tests

This parameter, E_c has some similarities to the Elasticity Modulus obtained from tensile tests, in the way it is also measured as the slope of the elastic trend of the stress-strain curve, however, in this case, both stress and strain are negative, due to the load nature and the material's response. According to the study done by Barile et al.[45] this value does not show the same tendency as the Elasticity Modulus obtained from tensile tests, as it is similar at all three tested temperatures (-54ºC, 23ºC and 71ºC).

2.6.3 Buckling

Messager et al. [50] studied compressive-dominant loads on shell composite structures, and concluded the most important load is the ultimate one. This load can be achieved either when the structure collapses or when the material fails plastically, however this mechanism presents a sudden transition between well behaved to buckled.

Moon et al. [51] reported maximum buckling pressure for a thick cylinder wound when the winding angle is ±60º.

Almeida et al. [29] developed a numerical model in which they realised tubes with a diameter-to-thickness ratio lower than 20:1 fail by buckling, as opposed to [90 $\pm 55_{12}/90$] ones which, as a result of their higher d/t ratio, failed primarily due to in-plane shear with delaminations. They also compared these results with experimental tests and found a great correlation, as relative pressure strengths were lower than 8.4%.

Bai et al.[52] carried out compressive tests on GFRP laminates under temperatures of up to 180ºC and reported a buckling load reduction up to 60% at 180ºC.

2.7 Shear Strength

The shear strength of a composite material is its ability to withstand a load to shear the specimen, so that the moving portion would completely clear the stationary one. This property is determined by the ratio between the force required to shear the specimen and the area of the sheared edge[48]. There are two different measures for the shear strength, the in-plane shear strength and the interlaminar shear strength, being the former the shear strength in a laminate plane, and the latter the strength between laminate planes.

2.7.1 Shear Modulus

In a shear situation the multiple layers of CFRP are trying to slide against the adjacent ones. Under this type of load the resin plays a major role transferring stresses along the composite. In order to have a composite system which performs well under shear loads, the resin must have good mechanical properties, however it is also of extreme importance to have a good adhesion between the reinforcement fibres and the resin[17], and having a resin which can withstand heat without severe damage[53].

Analysing the complex stress state caused by a shear loading is rather complicated, namely due to the multiaxial stress state for each ply orientation[54].

According to Adams[54], unlike tensile and compressive strengths, which are carried most efficiently along the fibre direction, shear stresses are carried most efficiently when fibres are aligned ± 45º. This concept can be demonstrated by analysing a laminate. If the shear element is rotated 45º, we can clearly assess the ± 45º fibres are actually carrying stresses in tension and compression, as is demonstrated in figure 2.9.

2.8 Flexural Strength

Flexural strength is the ability of the material to withstand bending forces. This force should be applied perpendicular to its longitudinal axis[48].

When a composite system is submitted to bending loads, it is subjected to a mix of tensile, compressive and shear stresses. The upper face is under compression, while the lower side is

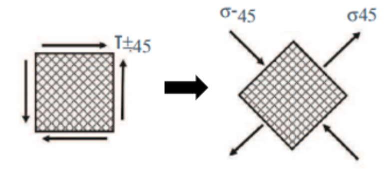

Figure 2.9: Shear Stresses[54]

under tension and the central portion under shear[17]. This stress distribution is developed further along, on section 2.12.7, in figure 2.13.

According to Bazli et al.[8], when composite systems are not subjected to high temperatures, laminates behave linearly and eventually fail due to delamination fracture. However, as the temperature increases, so does the nonlinearity of their load-displacement curve near the ultimate bending load. At 200ºC this nonlinearity can be noticed, but it is more prominent at 300ºC.

According to Bazli et al.[53], the thinner the laminates, the more vulnerable they are to bending failure, when compared to thicker ones. Moreover, it was demonstrated that laminates with continuous unidirectional fibres showed better performance than those made of woven and chopped strand mat fibres.

Shekarchi et al.[55] also studied the bending performance of CFRP laminates after exposure to different temperatures and realised there is a significant reduction in strength at 350ºC that was gradually assessed with the increase in temperature.

Bazli et al.[8] also defend matrix degradation affects the strength of FRP's bending properties, especially interlaminar shear strength. The maximum temperature the FRP laminates tested in this study could withstand during bending test was less than 400ºC, which was lower than the one that could be withstood in tensile tests. These tests were performed both with glass reinforced and carbon reinforced polymers, and various matrices were used, namely epoxy, unsaturated polyester, vinyl ester and phenolic. It should be noted the higher temperatures were achieved in specimens in which there was an epoxy matrix. In order to assess the behaviour of the resin in FRPs, Bazli[53] defends the temperature range must be defined according to the resin. There are 4 different ranges:

1. Below the glass transition temperature;

2. Above the latter, but lower than the resin decomposition temperature, T_d;

3. Temperature ranges near the resin decomposition temperature;

4. Temperatures above T_d, usually when fire is involved[53].

Bazli et al.[53] analysed the failure mechanisms under three-point bending loading of FRP specimens after being exposed to temperature values in the ranges 1, 2 and 3 of the previous enumeration. The thickness effect was also studied. It should be noted all the tests were performed at room temperature (25ºC). The conclusions of this study can be found on table 2.5.

Table 2.5: Failure Mechanisms under three-point bending[53]

Temperature	Failure Mechanism	Comment
T = 60ºC < T_g	All specimen failed in the tension zone through fibre rupture	Failure mechanism similar to the one experienced if the composite had not been heated
T_g < T=120ºC < T_d	Almost all specimen failed due to local compression failure besides fibre fracture in the tension zone	Thin unidirectional laminated specimens were not sufficiently degraded, so their failure mechanism had not changed
	Woven laminates failed by a mix of compression and buckling	This was due to resin degradation
T≥200ºC > T_d	Almost all specimen failed due to interlaminar shear delamination	This was mainly due to the significant damage done to the matrix during heating, which led to a decrease in the mechanical properties of the resin, thus diminishing the load transferring capacity between resin and reinforcement
	Thinner (2mm) woven laminated specimen failed by compression and fibre buckling	This may have been due to the relative lower compressive strength than the interlaminar shear strength of the laminates

One other conclusion Bazli et al.[53] took from their study was the time of exposure to each temperature, 20 or 120 minutes, didn't have any effect on the failure mechanism.

According to Hu[56] the flexural load-deflection responses of multiaxial warp-knitted fabrics exhibits less nonlinearity when compared to the tensile and compressive responses. All the laminates studied showed brittle failure, as is expected when dealing with CFRP with an epoxy matrix. When assessing the failure for laminates along the fibre direction, the delamination started in the middle of the specimen, and then it propagated outwards until significant fibre rupture occurred at the middle section. When the fibres were oriented ±45º to the specimen direction, ductile failure was observed.

2.8.1 Bending Modulus

Bending modulus is a measure of stiffness during the first or initial step of the bending process. Some authors, namely Campo[48], defend this parameter should be called "modulus of elasticity in bending", because of its physical meaning. This value is the slope of the initial straight line portion of the stress-strain curve, and is the ratio between the change in stress and the change in strain. In these graphs, the initial part of the stress-strain curve is seldom straight, so in order to mitigate this problem, one should consider the straight line that intersects the origin and the point at which the strain is 0.02[48].

2.9 Torsion Strength

Torsion strength is the ability of a material to withstand torsion forces, or a momentum, applied along its longitudinal axis.

Several studies, especially on CFRP-strengthened reinforced concrete/steel sections have proved the torsional effect must be taken into consideration[57, 58].

According to Wang et al.[59], increasing the number of CFRP layers has steady effects on the mechanical properties. This was proven by comparing a 6 layer CFRP with a 1 layer CFRP, where it was shown an increase in torsional capacity of 8.55%

Panchacharam et al.[60] also stated, when studying the effect of CFRP as reinforcement in reinforced concrete, that spiral wrapping at 45º is more efficient than 90º wrapping.

Loughlan[61] analysed the buckling effect on thin CFRP square tubes while in torsion, among other stresses and realised the ply modulus ratio E_1/E_2, being E_1 the Young modulus in the fibre direction and E_2 the same property in the direction perpendicular to the fibre in-plane, has a significant effect on the torsional local buckling performance, and by increasing this ratio, higher levels of the degrading influence of bending anisotropy in CFRP walls were observed. Besides this ratio, the number of plies, the length of the tubes and the direction of the applied torsional load was also found to be of some importance, albeit clearly lower when compared to the E_1/E_2 ratio.

Gonçalves et al.[62] studied the buckling effect of thin-walled regular polygonal tubes subjected to torsion, among others, and stated the buckling coefficient decreases when the relation L/b increases, L being the length of the tube and b the width of each side of the polygon, although this value tends to stabilize when the ratio is greater than 10, with an error margin of only 2% between infinitely long tubes and those in which $L/b = 10$.

2.10 Impact Strength

Impact strength is a complex phenomenon, sensitive to a multitude of parameters. It is the ability a material has to resist high rate loading and is related to the product performance, service life and impacts issues of product safety[48].

This property can also be used as a production quality control tool, namely for resins. Several characteristics affect the performance on these tests of a material, namely[48]:

- Stress concentrations;
- Shape and geometry of the impact striker;
- Thickness of the specimen;
- Geometry of the specimen;
- Exposure to environmental stress (creep, temperature, UV, among others);
- Molding process variables[48].

Charpy impact test is a low velocity impact one. It is of extreme importance for composite materials because a significant decrease in their performance may be caused by an internal fracture, even if there is no obvious failure at the impacted area. The low velocity nature of this test leads the specimen to be highly dependent on both the fibre configuration and the sample thickness[48].

According to Bazli et al.[53], who did impact tests to determine the variation in impact resistance after laminates had been exposed to different temperatures, laminates that had been exposed to temperatures below 200ºC fail due to the rupture, pull-out of the fibres and sample fracture, while samples exposed to temperatures grater than 200ºC show considerable delamination, despite the reinforcement being unidirectional, woven or a chopped strand mat. This study also proved unidirectional laminates had the best behaviour, however thick woven laminates also had appropriate performance, which meant its thickness was appropriate, moreover fibres perpendicular to the load orientation may have considerable contribution in load carrying. It was also demonstrated the longer the exposure time to temperature was, the lower the impact resistance of each specimen was. Thickness had a small impact in the absorbed energy for both exposure times, however the lower the exposure time, the higher the thickness' importance.

2.11 Fatigue Characteristics

Fatigue describes the failure of materials after being subjected to repeated loads or stresses lower than the ultimate strengths. These repeated loads can be[48]:

- Bending;
- Tension;
- Compressing;
- Impacting;
- Twisting[48].

After being subjected to such forces under various cycles, the material may break under a significantly lower load than the one obtained for a single loading test. The purpose of defining these properties is to determine the highest level of repeated loading that a material can withstand in long-term use[48], which is a value much more representative of the conditions it will be subjected to in service. In these tests, the predictable result would be for specimens subjected to high loads failing in a shorter time than those subjected to lower loads.

Two different types of test can be done, constant load, where the deformation would increase constantly, or constant deformation, where the load would decrease[48].

2.12 Tests

In this section, the different tests for defining the aforementioned properties will be elaborated.

Few ASTM or ISO standards have been defined for tubes, so for the mechanical properties with no standard defined for tubes, an analysis of the standards designed for laminates and a proposal of the necessary adjustments should be done, in order to allow the characterization of these properties[45].

2.12.1 Glass Transition Temperature Tests

The glass transition temperature can be determined by testing different mechanical properties at increasing temperature until a sudden and significant drop in the measured property occurs. However, proceeding this way is rather time-consuming and expensive, so, in order to mitigate this problem, tests are usually performed with a single specimen subjected to repeated or continuous loading while the test temperature is slowly increased[63].

For thermosetting polymers, typically used in composite solutions, three material properties are commonly used to determine the glass transition temperature[63].

1. **Heat capacity** - This method, which is developed in ASTM D7426, uses Differential Scanning Calorimetry (DSC) to measure the changes in the heat needed to increase the temperature of a sample. This is a simple and economical method for determining T_g based on heat capacity changes. Despite this method being frequently used for polymeric materials, it is harder to use on composites due to the low (usually less than half) volume percentage of resin in a composite material, thus the change in heat capacity is lower and harder to detect using DSC[63].

2. **Coefficient of thermal expansion (CTE)** - This method focus on the measure of the dimensional change a polymer suffers with increased temperature. During their glass transition, polymers suffer a dramatic CTE increase. Thermomechanical analysis (TMA) methods are used to measure the increase in length of a polymer sample with the increase in temperature, as described in ASTM E1545. Similarly to what happens with the heat capacity test, reinforcement fibres significantly reduce the change in CTE associated with the polymer's glass transition[63].

3. **Stiffness under mechanical loading** - This method focus on the assessment of a polymer's decrease in mechanical stiffness when the glass transition temperature is reached. Dynamic Mechanical Analysis (DMA) methods apply an oscillating force to the specimen with an increase in temperature, while measuring the displacement. The stiffness is then determined and used to identify the glass transition. This method is standardized for different mechanical loads such as tension (ASTM D5026), compression (ASTM D5024), torsion (ASTM D5279), three-point bending (ASTM D5023) and dual cantilever beam flexure (ASTM D5418). Procedures for polymeric materials are provided in ASTM D4065[63].

For composite systems, the magnitudes of stiffness reductions at T_g are reduced significantly, when compared to polymeric materials, due to the reinforcing fibres. However, bending stiffness decreases are still present. The use of DMA under bending loading is the most commonly used method for T_g determination of FRP[63].

Although this test establishes a limit for the temperature for each FRP, a lower value is chosen as the maximum allowable for a particular application[63].

2.12.2 Void Percentage Tests

Techniques for characterization of voids have evolved over time, from simple methods such as density determination (Archimedes principle) and matrix burn-off, to more advanced ones, such as X-ray micro-Computed Tomography (micro-CT).

2.12.2.1 Density Determination

This technique gives the void volume fraction. According to ASTM D2734, the void volume (V_v) can be achieved by the relative difference between theoretical (ρ_c^T) and measured (ρ_c^m) composite density, which can be expressed according to equation 2.3, where W is the weight percentage, the density is ρ, and the subscripts r and f stand for resin and fibre, respectively[21].

$$V_v = 100 - \rho_c^m \left(\frac{W_r}{\rho_r} + \frac{W_f}{\rho_f} \right) \tag{2.3}$$

The density of both resin and composite can be measured by water buoyancy through the Archimedes principle (ASTM D792), the density-gradient technique (ASTM D1505), and directly measuring weight and volume. The density of the fibers should be measured through water buoyancy or through gas pycnometry, in case water absorption by the fibres occurs. The measurement of the matrix and fiber weight and volume percentages can be done either through digestion, through ignition of the matrix (ASTM D3171 and ASTM D2584) or by microscopy followed by image analysis methods[21].

Accurate void content measurement requires precise knowledge of the physical properties of the components, so the accuracy this process gives is, at best, $\pm 0.5\%$. One other disadvantage this technique presents is its lack of ability to reveal other void characteristics such as size and shape. Albeit this being a destructive technique, it is still suitable for quality control purposes as it is applicable to large samples and is relatively fast[21].

2.12.2.2 Matrix Burn-off

This method, standardized in ASTM D2584[64], uses a furnace to remove the laminate's matrix surrounding the fibres, which permits the fibre weight fraction to be determined. Both fibre degradation and convection currents affect the precision of this technique, as fibre mass can be removed inadvertently. This error occurs with extreme significance when dealing with CFRPs, as the temperatures for achieving matrix burn are above those for carbon fibre oxidation[65].

After the matrix is removed, the volume fractions are calculated from the weights and densities of the constituents. The volume fraction of fibres, V_f, is determined from equation 2.4, where

W_f and W_m are the weights of the fibres and matrix, and ρ_f and ρ_m are their known densities, respectively[64].

$$V_f = \frac{\rho_m W_f}{\rho_f W_m + \rho_m W_f} \tag{2.4}$$

In order to determine the void volume, V_v we should resort to equation 2.5, where ρ_c is the composite density, obtained through equation 2.6[64].

$$V_v = 1 - \frac{(W_f/\rho_f + W_m/\rho_m)\rho_c}{W} \tag{2.5}$$

$$\rho_c = \frac{W}{V} \tag{2.6}$$

2.12.2.3 Matrix digestion

This process, standardized in ASTM D3171, is similar to matrix burn-off, however, instead of thermal degradation, acid is used to eliminate the matrix from around the fibres[64]. It is also a dangerous technique, due to the toxic fumes which are produced during the chemical break down of the matrix[65].

The selected medium must be chosen carefully in order to use one that attacks the matrix, but not the fibres. Similarly to matrix burn-off, after the matrix being dissolved, fibres are weighted to enable calculations of fibre volume fractions[64].

The volume fraction of fibres is determined from equation 2.4 and to determine the void volume we should resort to equation 2.5[64].

2.12.2.4 Microscopy

Void characterization is also possible through optical and electron microscopic techniques such as Scanning Electron Microscope (SEM). The volume of voids can be determined through optical counting and area fraction. Hsu et al.[66] confirmed the area fractions obtained from this process on cross-sections are a good approximation to volume fractions obtained by density determination, while Rousseau et al.[67] found this process achieved a higher void content than the one obtained by density determination.

However, this technique provides dramatically section-biased results, meaning they are influenced by the two-dimensional section chosen for analysis and different views can provide different results. Thickness view (perpendicular to plies) provides more accurate results for void content, while planar view (parallel to plies) provided more reliable results when it came to void size distribution. In order to assess the shapes of voids a combination of both views must be incorporated[21].

2.12.2.5 Ultrasonic Testing

The velocity and attenuation of an ultrasonic pulse traveling through or reflecting from the back surface of a FRP depend on void content and FVF. This type of test, which is probably one of the most common non-destructive testing methods for evaluating voids in composite materials, measures the attenuation of an ultrasonic pulse passing through the specimen[21].

Stone and Clarke[68] noted a bilinear relationship between void content and the ultrasonic attenuation coefficient in unidirectional CFRPs. They realised that for a void content up to 1.5%, the voids were mainly volatile-induced, which appear as small spheres within plies, while for a void content greater than 1.5%, air entrapped inter-laminar voids are predominant, which are larger. This change in the type of voids results in a particular curve for the relation between void content and ultrasonic attenuation, as portrayed in figure 2.10.

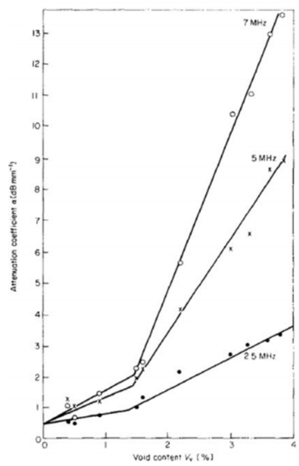

Figure 2.10: Ultrasonic attenuation coefficient as a function of void content[68]

However, in some studies only a linear relationship is reported, which can be due to the presence of only one void scale, either lower or higher than roughly 1.5% void content, or due to a modification in either reinforcement or matrix[21].

For given materials, calibration curves could be built by which the measurement of two or more ultrasonic wave velocities could be translated into an estimate of the voids content[69]. Stone and Clark [68] also demonstrated the attenuation is greater with the increase in the frequency and laminate thickness.

Ultrasonic polar scans can also be used for void inspection in composites, either in transmission, reflection or backscatter mode. This technique informs on the local characteristics of the material, which have great utility for analysing the internal structure. On the other hand, it faces more difficulties with in-service inspection and is not appropriate for quantitative explorations[21].

The main disadvantage of direct ultrasonic techniques is the need for a coupling agent between the material and the ultrasonic transducer, such as water. This poses as an issue especially for larger composites whose mechanical properties are sensitive to moisture, but can be overcame by using air coupling[21].

Air-coupled ultrasonic inspection methodologies comprise surface topography, transmission analysis and guided wave inspection. Using lamb waves is the most frequent approach. These waves are transmitted to the plate through one surface and interact with the defects inside the plate. Afterwards they are detected by a receiver above the same surface, but outside the reflection field[21].

Another variant of this process is laser-generated ultrasound, which has an edge due to the possibility of non-contact inspection[21].

The drawbacks of conventional ultrasound techniques are[21]:

1. Limited to flat samples;
2. Samples must have low surface roughness;
3. Need of a coupling agent;
4. Slow;
5. Low-flexibility performance[21].

Most of these drawbacks have already been surpassed by studies with laser-generated ultrasound, and so it is claimed this methodology can provide direct data on void amount, similarly to X-ray tomography, while being portable and cheap. Moreover, laser-generated ultrasound creates broadband acoustic pulses which allow to excite a wide range of frequencies, ans thus, provide a wide range of information, through a B-scan. The drawbacks of this variant is being hardware-intensive and the potentially dangerous operation[21].

One other solution which is proposed to solve items 4 and 5 of the previous enumeration is phased array ultrasound technique which uses an ultrasound transducer composed of several small piezoelectric elements (opposed to conventional ultrasound transducers with only one element) and, as such, allow multiple examinations from a single location providing greater flexibility. Furthermore, this technique prizes itself by being significantly faster than conventional ultrasound technique. The constraint this technique provides is the fact it can only be used with thin samples[21].

2.12.2.6 Micro-CT

Micro-CT or X-ray micro-Computed Tomography is the most advanced and most accurate technique for assessing the quantity of voids in a composite structure. It consists of obtaining several X-ray images from different angles of an object, and creating a three-dimensional image of it[23]. The images are achieved due to the difference in both the absorption and scattering of X-ray by different materials, thus allowing to analyse the internal structure of the object[21].

It has an edge by being a non-destructive test which provides full three-dimensional analysis of voids, as it provides information on voids, such as[23]:

- Shape;
- Size;
- Orientation;
- Spacial orientation of mainly interlaminar voids[23].

Nevertheless, it also has some shortcomings, namely its high cost and the fact on systems only with geometric magnification (as opposed to optical magnification), the resolution is inversely dependent on sample size, which means if a resolution of only several micrometers/pixel is to be achieved, the sample should be, at most, only a few millimeters in the maximum dimension[23]. Due to the results dependency on density and atomic number of the scanned material, this technique is challenging for the analysis of similar materials in this regard[21].

The addition of a contrasting agent to the resin before it is impregnated increases the absorption coefficient, which eases the analysis, as it provides results an histogram with a more distinct peak of both air and polymer[21].

Little et al.[65] confirmed that micro-CT is the most reliable and accurate technique available for analysis of both shape, size, distribution and content of voids in composites, as this technique is not section-bias, and has less location-bias error.

Other tomographic approaches exist, such as optical coherence tomography, which uses optical light as opposed to X-ray[21].

2.12.2.7 X-ray Radiography

This method, which produces a two-dimensional projection of a volume, can reveal important information regarding voids, albeit these can only be detected through thickness and they must have appreciable size, when compared to the specimen's thickness. One solution to improve the quality of the results is through the impregnation of radio-opaque substances into the voids, as the contrast improves with those. Nevertheless, difficult penetration of large parts and the effect of penetrant on the mechanical properties are the main drawbacks of this approach[21].

2.12.2.8 Thermography

This is a fast, reliable and non-contacting technique which enables the detection of voids in large FRP parts. Through the application of heat, either directly or not, to the part, the temperature of the composite increases. This parameter is monitored both on the side of the heat application and on the opposite one, and anomalies in its distribution reveal the existence of voids. It has been proved that for samples with high void amounts, smaller temperature rises were recorded on the opposite side. Both the conductivity and anisotropy of the composite, and the depth at which the defect is located are important[21].

2.12.2.9 Shearography

This technique requires a very high stability of the test specimen and inspection instrument in relation to each other, thus is hardly ever used in industry. This technique identifies the strain concentrations induced by the defects to identify them, as these concentrations result in anomalies in the fringe pattern. Shearography does not require fluid coupling and is a full-field, non-contacting, non-destructive test[21].

2.12.2.10 Terahertz [THz] Time Domain Spectroscopy

This technique makes use of the terahertz domain of electromagnetic radiation to penetrate into the tested specimen. Air has a lower THz absorption than the composite, so this difference is used to detect voids, provided THz waves can penetrate the composite[21].

2.12.3 Axial Tensile Test

The measure of the tensile strength and modulus are among the most important indications of strength in a material. A tensile test is design to measure the material's ability to withstand forces which pull it apart and determine how much the material can stretch before rupture occurs. The tensile modulus is an indicator of the relative stiffness of a material and is determined from a stress-strain curve, as the slope of the initial portion of the curve[48].

Several standards exist for testing composite laminates, both according to ISO and according to ASTM. In table 2.6 the differences are exposed[48].

Table 2.6: Comparison between ISO and ASTM standards for laminates tensile testing [48]

	ISO Standard	**ASTM Standard**
Standard	527-1:1993 and ISO 527-2:1993	ASTM D-638
End-gate	Mandatory	Optional
Cross-section	4.0 mm x 10.0 mm	0.125 in (3.17mm) x 0.50 in (12.7mm)
Cross-head speed	1.0 mm/min	5.0 mm/min
Determination of the testing cross-head speed	Based on the elastic properties of the materials	Based on the time to complete the test or by relevant material standard

In these tests, a tight clamping force on the specimen might create stress concentration points, influencing the results.

An axial tensile test done by Martins de Brito[32] with a FRP composite tube is shown in figure 2.11. This test allows for the determination of the Elasticity Modulus obtained from tensile tests, E_t, and the Poisson coefficient, ν. These are obtained by positioning a set of extensometers, one in the axial direction and other in the circumferential. Each set of extensometers is composed by 3 extensometers with an angle of 120º. Through this test it is also possible to assess the ultimate tensile strength[32].

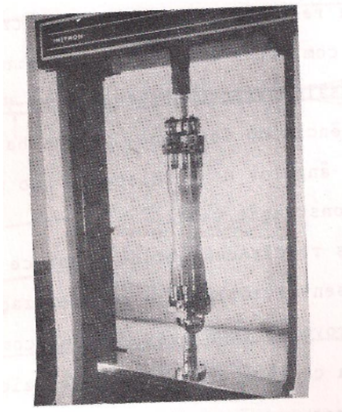

Figure 2.11: Axial Tensile Test [32]

2.12.4 Tensile Creep Test

Creep testing is designed to validate the materials' response to a constant load with time. For it to be performed, a specially designed extensometer should be used and constant stress and temperature should be applied to the specimen[48].

Creep is the time-dependent deformation of a material while under a constant load which is below its yield strength and is caused by diffusion processes and dislocation movements. It is most frequent at high temperatures, however some materials suffer creep at room temperature. Creep has three stages[48].

1. **Primary Creep (Stage I)** - Occurs in the beginning of the test. The creep rate is high, but is decreasing slowly with time[48].

2. **Secondary Creep (Stage II)** - It is represented by the stable part of the curve. The creep rate is low and stable[48].

3. **Tertiary Creep (Stage III)** - Final creep stage. The creep rate is increasing at the same rate as elongation until rupture occurs[48].

2.12.4.1 Standard Tensile Creep Test

The procedures for this test are only defined in ASTM D-674 standard for laminates. Thermoplastics are viscoelastic materials, this is, their strength and deformation under stress is dependent on load duration. Thermosettings also have a viscoelastic property, albeit being less evident when compared with thermoplastics. In order to be possible to predict the behaviour of a composite material, such as CFRP, it must be tested for tensile strength properties that include time and temperature as independent variables[48].

When a polymeric material is subjected to a constant load, its deformation increases gradually with time. This deformation is greater than the one predicted by its modulus, therefore, in the design phase, creep must be considered[48].

This test consists on the application of a constant load and measuring the extension of the specimen with time. The creep strain is the ratio between the extension and the initial gauge length, which can then be multiplied by 100 to achieve this value as a percentage. This value (percentage of creep strain) is plotted against time, thus obtaining a tensile creep curve. This test should be done in a laboratory in order to condition the temperature of the specimen so as to evaluate the temperature impact on tensile creep properties[48].

2.12.4.2 Tensile Creep Rupture Test

Creep or stress rupture test data tend to be plotted as stress versus rupture time, where each point corresponds to one test at a specific temperature and stress level[70]. This test differs from the previous one due to its accountability of the time until rupture and the effect of temperature on long-time load-bearing characteristics[71]. Moreover, the deformations at hand are much greater than the ones in the standard tensile creep test[72]. The results achieved in this test are important for the selection of materials for parts whose dimensional tolerances are not critical, but where break must not occur[71].

2.12.5 Axial Compression Test

The compression test procedures for laminates is only defined by ASTM D-695, not existing an ISO standard[48].

This test can provide information on several properties, such as compressive strength, modulus, yield stress, deformation beyond yield point, and compressive strain. However, the first and second properties mentioned are the most important and most used[48].

In order to guarantee the quality of the results, attention should be given to the properties which are being assessed. While for testing the compressive modulus, a long specimen can be used, as it depicts a scenario closer to the desired application, for testing the ultimate compressive strength, shorter and sometimes supported specimen should be used in order to have a purely compressive failure, as opposed to a buckling one, which would result in a lower value for this property[48].

2.12.6 Impact Strength Test

For impact strength testing there are several test procedures:

- ISO 179:1993 Charpy impact strength uses a hammer that strikes the edge opposite the notched edge of the specimen. In neither ISO nor ASTM D-256 procedures is the specimen clamped. Due to the different notch geometries and specimen dimensions between ISO and ASTM standards, the results cannot be compared;

- ISO 8256:1990 employs a specimen of 4.0 mm by 10.0 mm, notched on both 4.0 mm edges. The ASTM D-1822 tensile impact test uses long specimens. This test is only used if the material does not break under ISO 179:1993. The test results of both these standards are not comparable;

- ASTM D-3029 states a procedure for the Gardner falling weight impact test, while ISO ignores this test. In this test, a weight is dropped free-falling from a height of 20 cm and, after testing, the specimen are analysed for failure[73].

2.12.7 Bending Test

ISO 178:1993 and ASTM D790 test standards for laminates have similar testing procedures. The flexural stress is generally higher than either compression, tensile or shear stresses[48].

ASTM D7264 is another standard for assessing flexural properties, which assumes the specimen will fail due to bending stress. It requires the length-to-thickness ratio, l/t, to be 32:1 for either three-point or four-point loading. A schematic with the distance between loads according to this standard is portrayed in figure 2.12[74].

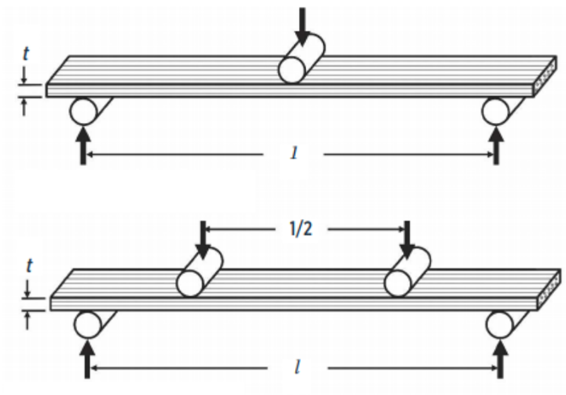

Figure 2.12: Flexural test configurations[74]

The greatest difference between three and four-point bending tests is the length of the region which experiences the maximum bending stress. While in three-point bending tests that value is only achieved in the central cross section located below the loading cylinder, in four-point bending tests the maximum stress is experienced along the bottom part of the tube along entire inner loading span. In both configurations, in the zone that suffers the maximum bending stress, the stresses along its thickness are represented in figure 2.13 and, in that zone, are maximum for the whole specimen[74]. Due to this reason, the specimen tend to fail along either top or bottom surface. It should be noted these stresses have the same magnitude, thus the failure mode and location is strongly dependent on the tensile and compressive strengths of the material[74].

The property measured in ASTM D7264 is referred to as flexural strength, which is the maximum stress in the outer surface of the specimen when the maximum force is applied[74].

Another standard important in this consideration is ASTM D6272, which refers to the flexural properties of unreinforced and reinforced plastics for four-point bending. This standard, however, has one limitation regarding the desired application, it has been designed for flat specimen as opposed to tubular ones. This presents itself as a difficulty because the contact surface between the cylindrical noses and a flat specimen is given by a line, while the contact surface between the cylindrical nose and the tube is given by a single point, provided geometrically perfect pieces and

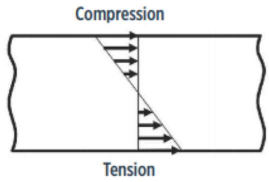

Figure 2.13: Through-the-thickness bending stress distribution[74]

without any deformation, this being a cause for crushing which may invalidate the test. Solutions for this problem will be further developed in chapter 3.

2.12.8 Flexural Creep Test

Investigators have tried to define tests that can comprehensively study this property. Flexural creep measurements are made through the application of a constant load to the specimen while measuring the deflection with time. The percentage of creep strain is plotted against time to obtain a flexural creep curve. In order to obtain a deep assessment of this property tests should be carried out for different stress levels and temperatures[48].

2.12.9 Torsion Test

This test is shown in figure 2.14. While performing this test, the ratio R/e, being R the average radius and e the thickness, and the ratio L/R, being L the length of the tube, need to be analysed in order to define if the tension gradient along the width is significant or not. If this gradient is not significant, the stress state is uniform in the reference zone and τ_{12} can be calculated according to:

$$\tau_{12} = \frac{T}{2\pi R^2 e} \tag{2.7}$$

Where T is the torsion moment and τ_{12} is the shear stress. To determine the shear modulus, G_{12}, strain gauges or extensometers need to be inserted in the central section of the tube in order to determine the distortions[32].

2.12.10 Fracture Mechanics Approach

Another approach which can be suitable to determine the mechanical properties of a composite tube is a fracture mechanics approach. This approach is based on the tube's response based on the crack propagation. On this work only a brief introduction will be made, however, it is also a possible path to achieve valid results.

2.12.10.1 Mode I

One method for assessing a pipe's susceptibility to interlaminar delamination is by measuring the interlaminar fracture toughness. [31]

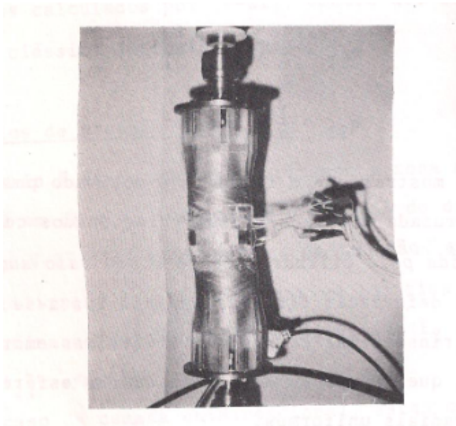

Figure 2.14: Torsion Test [32]

In order to assess delamination events correctly, a fracture mechanics approach is the most convenient choice. In order to do so, the critical energy release rate must be evaluated, G_{Ic}. No standard either by ISO neither by ASTM exist for measuring this property for filament wound tubes, as ASTM D5528 and ISO 15024 require the specimen to be flat, unidirectional and symmetric. [31]

The Double Cantilever Beam (DCB) is the most used test for the characterization of the mode I energy release rate, which is standardized for unidirectional laminates both in ASTM D5528 and ISO 15024[31].

Testing filament wound materials according to the mentioned standards presents a number of constraints that make it impossible to use said standard. Some should be highlighted:

1. Curved geometry of test pieces;
2. Classical angle-ply,$[\pm\Theta]_n$, stacking sequence that produces a mixed-mode stress field at the crack tip;
3. Non-unidirectional interwoven layup;
4. fibre bridging[31].

The DCB test has the purpose of evaluating pure opening fracture (mode I). However, because of the curved geometry, a mixed-mode stress field is achieved at the crack tip of test pieces. In the case of axially symmetric components, it is possible to have two different sample geometries. One is obtained by cutting the pipe in the axial direction (longitudinal) and the other in the hoop direction (transverse), as shown in figure 2.15. Naturally, due to the different curvature and layup which can influence crack propagation, the results are expected to differ, as shows the literature, namely by Ozdil et al.[75] and Davies et al.[76] who tested specimen in the longitudinal direction, while Lauke et al.[77] tested samples which were cut in the transverse direction[31].

The longitudinal samples presented a curved crack with a straight crack propagation path while the transverse samples showed the opposite behaviour, a straight crack with a curved propagation path[31]. Increasing the winding angle also has a significant effect on the scatter of the evaluated value of G_{Ic}[31].

According to Lucas[78] and Laksimi et al.[79] the measured value of G_{Ic} increases with the increase in the mismatch in the fibre orientations of different layers, between which cracks propagate.

According to Perillo et al.[31] both longitudinal and transverse samples from filament wound pipes present a mixed-mode stress field at the crack tip. Mode II and Mode III can reach up to 1.5% and 10.2% of magnitude of the mode I component, respectively.

Perillo et al.[31] also concluded that transverse samples showed a lower fibre angle, thus yielding a lower G_{Ic} than the longitudinal samples, which provided a more conservative value for structural calculation, thus being more appropriate.

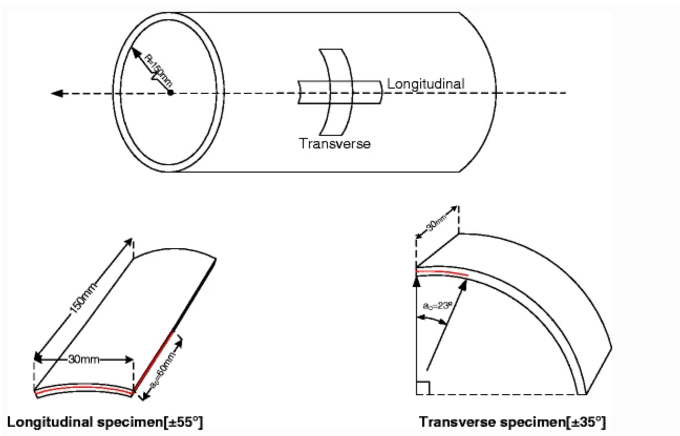

Figure 2.15: Different specimen geometries of a composite pipe [31]

Curved Double Cantilever Beam

The Curved Double Cantilever Beam (CDCB), proposed by Lauke[77] and Foral[80] is a method that is equivalent to DCB, but that has been adapted for curved surfaces. In this case, a curved piece is tested using a sample cut in the hoop direction.

The test consists of using as a specimen a segment of the tube for which the properties want to be known and using special fixtures contoured to fit the specimen diameter, grip the specimen on either side of a pre-induced crack and pull it apart, as demonstrated in figure 2.16.

According to Foral[80] acoustic emission monitoring was found to be a valuable supplement in this test so as to reliably identify failure modes.

Ozdil et al.[75] also used a curved filament wound sample for mode I, mode II and mixed-mode tests. Regarding this experiment, samples were cut in a direction parallel to the cylinder axis and the specimens were clamped using a support clamp for the tests. Davies et al.[76] assessed G_{Ic} both on filament wounded plates (unidirectional) and tubes (with three different winding angles). Davies concluded the results of G_{Ic} were similar for the different tests, but the scatter increased with the winding angle[31].

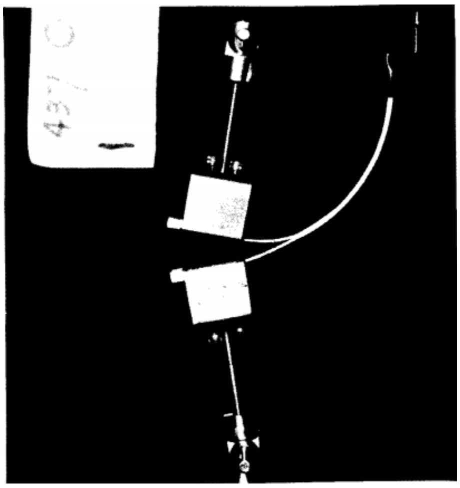

Figure 2.16: Curved Double Cantilever Beam test[80]

2.12.10.2 Mode II

The study of the dynamics in delamination of composite structures subjected to impact or cyclic actions are even more complicated for tubes than for laminates due to two reasons[81]:

1. The curved structure makes it more difficult to test and formulate the governing equations;

2. As it is a non-static phenomenon it is difficult to observe, for being nearly instantaneous, but also due to its invisibility at first glance, as it leaves no trace on the surface[81].

Chapter 3

Numerical Simulation

In this chapter, the numerical simulation will be discussed. This simulation will concern a numerical approach for the tests that will be done in the laboratory. The main purpose of these simulations is not to predict the material behaviour, but rather to test the different setups that can be used in order to validate the changes proposed to each standard to have valid tests with tubular specimen. The main reason for this is the fact the properties for the fibres and matrix or for the lamina are not fully known, this is, some approximations must be done as there are no tests for unidirectional composites for the required parameters, as will be explained further along. That being said, in the following chapter a comparison between the experimental and the numerical results will be performed.

3.1 Properties of the Lamina

In order to design a composite tube, the first step is to determine the mechanical properties of the lamina. This can be done either by estimation, through one of various analytical or semi-empirical models based on micromechanics, or through mechanical tests[4]. Some of those models will be developed in this section. The experimental tests are important to validate the model choice in the earlier stages.

In this section, the longitudinal direction is the fibre direction, in the equations identified by the subscript 1, while the transversal direction is the direction perpendicular to the former, identified with the subscript 2. Furthermore, the lamina is assumed to be transversely isotropic. When estimating the transversal properties, big micromechanics challenges arise due to a number of issues, namely fibre interwoven arrangement, the thickness effect and interface properties, thus, ideally, some additional properties may be needed, such as the interface strength and the critical dilatational energy. These properties are usually unknown so, an investigation about the reasonable average values needs to be carried out[82].

3.1.1 Rule of Mixtures

The rule of mixtures is probably the model to predict the mechanical properties of a composite with the simplest mechanical relations. It is based on Voigt's assumption, which states both the fibres and the matrix experience the same strain[83]. For the application of this model, in order to define the properties of the composite, identified with the subscript c, both the value of the studied property of the matrix, identified with the subscript m, and of the fibre, defined with the subscript f, alongside the FVF need to be known. Despite the ease of the mathematical relations, the experimental observations confirm that its predictions are, in several cases, unsatisfactory, namely in directions different than the longitudinal one. The relations according to this model are[84]:

Longitudinal Young's Modulus:

$$E_{1c} = E_f \times FVF + E_m(1 - FVF) \tag{3.1}$$

Transverse Young's Modulus:

$$\frac{1}{E_{2c}} = \frac{FVF}{E_f} + \frac{1 - FVF}{E_m} \tag{3.2}$$

Major Poisson's Ratio:

$$\nu_{12c} = \nu_f \times FVF + \nu_m(1 - FVF) \tag{3.3}$$

In-Plane Shear Modulus:

$$\frac{1}{G_{12c}} = \frac{FVF}{G_f} + \frac{1 - FVF}{G_m} \tag{3.4}$$

Ultimate Stresses[83]:

$$\sigma_c = \alpha\sigma_f \times FVF + \sigma_m(1 - FVF) \tag{3.5}$$

Where α is an harmonic coefficient based on the orientation of the fibres in the composite. This equation is valid for both longitudinal and transverse strengths and for compressive and tensile properties, provided the inputs (σ_f, σ_m and α) are correct for the property that is being studied[83].

Another equation according to the rule of mixtures to determine the Young's Modulus is expressed in Cao et al.[83]:

$$E_c = \alpha E_f \times FVF + E_m(1 - FVF) \tag{3.6}$$

3.1.2 Inverse Rule of Mixtures

This model, although being similar to the rule of mixtures, is based on Reuss' assumption, which asserts the transverse stress is the same at both the fibre and the matrix[83]. According to this model, the stress and Young's modulus can be predicted according to the following equations.

Stress:

$$\sigma_c = \frac{\sigma_f \sigma_m}{\sigma_f(1-FVF)+\sigma_m \times FVF} \tag{3.7}$$

Young's Modulus:

$$E_c = \frac{E_f E_m}{E_f(1-FVF)+E_m \times FVF} \tag{3.8}$$

According to Palsule et al.[85], the predictions according to this model provide more accurate results, when compared with experimental ones, than the ones predicted by the Rule of Mixtures.

3.1.3 Hirsch Model

This model finds its basis on both the rule of mixtures and the inverse rule of mixtures, and was proposed by Hirsch. According to this theory, elastic modulus and mechanical strength can be estimated by[83]:

Stress:

$$\sigma_c = \alpha[\sigma_f \times FVF + \sigma_m(1-FVF)] + (1-\alpha)\frac{\sigma_f \sigma_m}{\sigma_f(1-FVF)+\sigma_m \times FVF} \tag{3.9}$$

Young Modulus:

$$E_c = \alpha(E_f \times FVF + E_m(1-FVF)) + (1-\alpha)\frac{E_f E_m}{E_f(1-FVF)+E_m \times FVF} \tag{3.10}$$

3.1.4 Halpin-Tsai

Halpin and Tsai developed a semi-empirical model as simple equations by curve fitting to results that are based on elasticity. These equations are semi-empirical due to the physical meaning of the parameters in the curve fitting. The relations according to this model are[84]:

Longitudinal Young's Modulus:

$$E_{1c} = E_f \times FVF + E_m(1-FVF) \tag{3.11}$$

Transverse Young's Modulus:

$$\frac{E_{2c}}{E_m} = \frac{1+\xi\eta \times FVF}{1-\eta \times FVF}, \quad \eta = \frac{\left[\frac{E_f}{E_m}\right]-1}{\left[\frac{E_f}{E_m}\right]+\xi} \tag{3.12}$$

Where the term ξ is the reinforcing factor and depends on:

- Fibre Geometry;
- Packing Geometry;
- Loading Condition[84].

Major Poisson's Ratio:

$$\nu_{12c} = \nu_f \times FVF + \nu_m \times FVF \tag{3.13}$$

In-Plane Shear Modulus:

$$\frac{G_{2c}}{G_m} = \frac{1 + \xi\eta \times FVF}{1 - \eta \times FVF}, \quad \eta = \frac{\left[\frac{G_f}{G_m}\right] - 1}{\left[\frac{G_f}{G_m}\right] + \xi} \tag{3.14}$$

Another form of expressing the Halpin-Tsai model is described in [83], and is:

Ultimate Stresses:

$$\sigma_c = \sigma_f \left(\frac{1 + B\eta(1 - FVF)}{1 - \eta(1 - FVF)} \right), \quad B = 2\frac{L}{D}, \quad \eta = \frac{\frac{\sigma_f}{\sigma_m} - 1}{\frac{\sigma_f}{\sigma_m} + B} \tag{3.15}$$

Young's Modulus:

$$E_c = E_f \left(\frac{1 + B\eta(1 - FVF)}{1 - \eta(1 - FVF)} \right), \quad B = 2\frac{L}{D}, \quad \eta = \frac{\frac{E_f}{E_m} - 1}{\frac{E-f}{E_m} + B} \tag{3.16}$$

Where L is the specimen span, and D its diameter[84].

3.1.5 Comparison between Rule of Mixtures, Halpin-Tsai and Finite Element Analysis

Bhaskar et al.[84] worked on a comparison between the results provided by the rule of mixtures, the Halpin-Tsai and a finite element analysis for a polypropylene fibre matrix composite, while also comparing the evolution of each parameter with the fibre volume fraction, to compare which was the most suitable technique to be used. The results they faced are exposed in figure 3.1.

From figure 3.1, it is clear that while the rule of mixtures provides an accurate result for the longitudinal Young Modulus, its prediction for the transverse Young Modulus has significant error, especially with the increase in the fibre volume fraction. On the other hand, the Halpin-Tsai criterion provides accurate results in both cases and almost independently from the fibre volume fraction chosen. Nevertheless, an analysis according to the rule of mixture provides results for the transverse Young Modulus lower than the ones expected for the final laminate. Due to this fact, even tough the results have some error, the estimate is more conservative, thus, by considering this value the material response considered is below its limits.

Analysing figure 3.1a, it is also possible to verify the linear dependence of the longitudinal Young Modulus with the FVF, as the former increases with the latter.

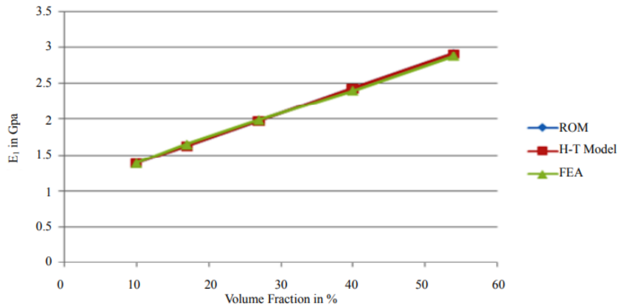

(a) Longitudinal Young Modulus

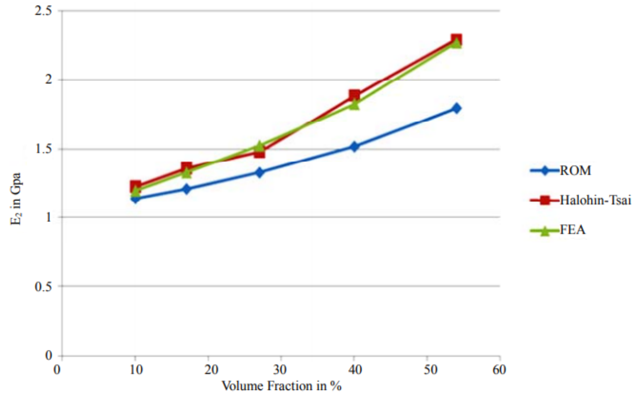

(b) Transverse Young Modulus

Figure 3.1: Comparison between Young Modulus according to different criteria[84]

3.1.6 Mori-Tanaka Model

The Mori-Tanaka model is another homogenization model for predicting the properties of heterogeneous materials, based on microstructural information, as the volume fraction, orientation, constituent properties, among others. The equations for a fibre reinforced composite are expressed in terms of the average strain and stress[86], as are in the following equation:

$$[\sigma] = \mathbf{C}[\varepsilon] \tag{3.17}$$

Where the effective average elastic moduli, **C**, is given by[87]:

$$\mathbf{C} = (V_m\mathbf{C}_m + V_f\mathbf{C}_f\mathbf{A})(V_m\mathbf{I} + V_f[\mathbf{A}])^{-1} \tag{3.18}$$

In this equation, **I** is the forth order identity tensor, V_f and V_m denote the volume fraction of the fibers and matrix, where, assuming perfect manufacturing (no voids), V_f is equal to the previously mentioned FVF and V_m to $1 - FVF$, and $\mathbf{C}_m$ and $\mathbf{C}_f$ are the forth order elasticity tensor of the matrix and the fibre, respectively. The value **A** is the Eshelby strain-concentration tensor which establishes the relation between the average strain in both the fibre and the matrix, through the expression[86]:

$$\varepsilon_f = \mathbf{A}\varepsilon_m \tag{3.19}$$

And is determined by:

$$\mathbf{A} = [\mathbf{I} + \mathbf{S}(\mathbf{C}_m)^{-1}(\mathbf{C}_f - \mathbf{C}_m)]^{-1} \tag{3.20}$$

Where **S** is the Eshelby tensor[88].

This model can be used to predict the elastic modulus of composites whose fibres are randomly distributed. In this case, the orientation and distribution of the fibres can be characterized by a probability density function with two Euler angles, α and β, as shown in figure 3.2 [86]:

$$\int_0^{2\pi}\int_0^{\pi/2} p(\alpha,\beta)\sin\alpha\, d\alpha\, d\beta = 1 \tag{3.21}$$

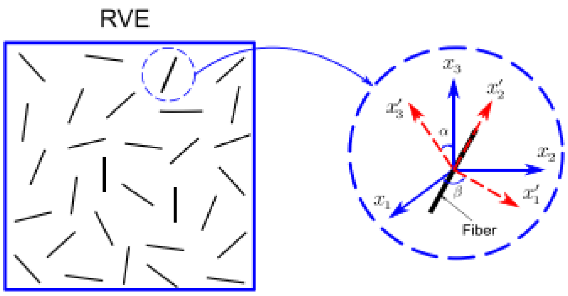

Figure 3.2: Representative Volume Element with completely randomly oriented straight fibres (left), and local coordinate system (right)[86]

If the fibres are completely randomly oriented, the probability density function is $p(\alpha,\beta) = 1/2\pi$[86].

3.1.7 Chamis Model

According to the Chamis model, the transverse tensile strength can be estimated by[82]:

$$\sigma_{1c} = \left[1 - (\sqrt{FVF} - FVF)\left(1 - \frac{E_m}{E_f}\right)\right]\left[1 - \sqrt{\frac{4V_v}{\pi(1-FVF)}}\right]\sigma_m \tag{3.22}$$

In this equation, a new variable is introduced, V_v, which represents the amount of voids present in the composite. This equation can be used to determine both the tensile and the compressive strengths, provided the Young Modulus and the tension used are coherent[82].

For the transverse shear strength, the Chamis model defines this value as[82]:

$$\sigma_{12c} = \left[\frac{1 - \sqrt{FVF}\left(1 - \frac{G_m}{G_f}\right)}{1 - FVF\left(1 - \frac{G_m}{G_f}\right)} \right] \sigma_m \qquad (3.23)$$

It should also be mentioned, in this case, the shear strength defined for the composite is the same as the input from the fibre.

3.1.8 Modified Chamis Model

Following the analysis of the last model, an alternative model has been proposed by Vignoli et al.[82], the modified Chamis model. This model only states an equation for defining the transverse strength, which is as follows:

$$\sigma_c = \left[1 - (\sqrt{FVF} - FVF)\left(1 - \frac{E_m}{E_f}\right) \right]^n \sigma_m \qquad (3.24)$$

A new variable has been introduced, n, which is a correction factor calibrated to the experimental results. This equation can be used for the determination of both transverse tensile and compressive strengths, albeit attention should be given to the variables used, both the Young Modulus, the strength, and the correction factor n should be coherent with the type of solicitation to be determined (compressive or tensile)[82].

Vignoli et al.[82] analysed the error various criteria (Bridging model, Chamis model with $V_v = 0$, Chamis model with $V_v = 0.09$, Chamis modified model with a correction factor of 5, rule of mixtures with stress concentration, and the dilatational energy) provided when calculating the transverse tensile strength. The results achieved in this study are exposed on figure 3.3, where we can see the Modified Chamis Model is the one which provides the lowest error.

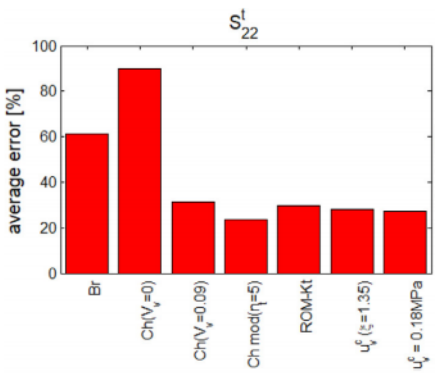

Figure 3.3: Average error provided by different criteria while calculating transverse tensile strength[82]

3.2 Failure Criteria

The subject of failure criteria for FRP composites has long been studied by several researchers, thus a significant number of approaches exist, which demonstrate the extreme importance of this study. Despite the progress made, it does not appear to exist one criterion universally accepted as adequate under general load conditions, so, in this section, various failure criteria will be exposed and discussed. There are two main different types of failure criteria, those associated with failure modes, and those not associated with failure modes[89].

3.2.1 Non-phenomenological Failure Criteria

This type of failure criteria uses mathematical expressions to define the failure surface as a function of the material strengths. These expressions tend to be based on the approximation of an expression to the curve achieved in the experimental tests. These criteria have been defined by extending and adapting criteria for homogeneous isotropic materials, such as maximum principal stress, maximum shear stress (Tresca), or maximum distortional energy (von Mises), to consider the anisotropy in stiffness and strength of the composite. Some theories here exposed do not account for the interaction between stress components, while others consider that interaction through additional data from biaxial testing[89].

3.2.1.1 Maximum Stress Criterion

This criterion establishes the failure of the composite when at least one stress component along the principal material axes surpasses the allowable value, defined as the corresponding strength in that direction. This is a simple and direct way of predicting the composites failure, however the interaction between stresses acting on the lamina that may occur is not considered. This criterion is more suitable to be applied for brittle failure modes. Three different conditions of failure are considered[89]:

- **Fibre**: $\sigma_1 \leq \sigma_{1T}^u \quad \text{or} \quad |\sigma_1| \leq \sigma_{1C}^u$
- **Matrix**: $\sigma_2 \leq \sigma_{2T}^u \quad \text{or} \quad |\sigma_2| \leq \sigma_{2C}^u$
- **Shear**: $|\tau_{12}| \leq \tau_{12}^u$

In the previous equations, the subscript 1 or 2 refers to the direction in which the property is measured, the subscript T refers to tensile loading, while the subscript C refers to compressive loading, and the superscript u refers to the ultimate property[89].

3.2.1.2 Maximum Strain Criterion

This criterion establishes composite failure when the strain component along the principal material axes surpasses the ultimate strain in that direction. It is also a simple and direct method of predicting failure for composites, however, because of the Poisson effect, the interaction of stress components is considered to some degree. The criterion considers three different conditions of failure, the maximum strain in the fibre direction, in the matrix or transverse direction and shear strain[89]:

1. **Fibre**: $\varepsilon_1 \leq \varepsilon_{1T}^u \quad \text{or} \quad |\varepsilon_1| \leq \varepsilon_{1C}^u$

2. **Matrix**: $\varepsilon_2 \leq \varepsilon_{2T}^u \quad \text{or} \quad |\varepsilon_2| \leq \varepsilon_{2C}^u$

3. **Shear**: $|\gamma_{12}| \leq \gamma_{12}^u$

In the previous equations, the subscripts and superscripts have the same meaning as for the maximum stress criterion.

A non-interacting maximum allowable strain criterion is commonly used in phenomenological failure criteria to represent longitudinal tensile failure.

3.2.1.3 Tsai-Hill Criterion

Hill modified the von Mises criterion for the case of ductile metals with anisotropy (e.g. laminated sheet metal) and later Tsai adapted this criterion for unidirectional composite laminae which present transverse isotropy. The Tsai-Hill failure criterion is expressed as a single criterion, and contemplates significant interaction among stress components. Nevertheless, no distinction is made between tensile and compressive strengths. The strength parameters must be specified according to the signs of the normal stresses σ_1 and σ_2. The equations which govern this criteria are[4, 90, 91]:

$$\frac{\sigma_1^2}{(\sigma_1^u)^2} - \frac{\sigma_1\sigma_2}{(\sigma_1^u)^2} + \frac{\sigma_2^2}{(\sigma_2^u)^2} + \frac{\tau_{12}^2}{(\tau_{12}^u)^2} = 1 \tag{3.25}$$

When applying this equation the ultimate properties must be defined as the compressive or tensile ones according to the load the structure is subjected to in that direction.

Tsai-Hill criterion is applied at a lamina level, and it describes a smooth elliptical failure envelope. In order to include stress and strength interactions in the fibre and matrix directions, a modified version has been proposed, the Tsai-Wu criterion[91].

3.2.1.4 Tsai-Wu Criterion

The Tsai-Wu criterion, just as the Tsai-Hill, is a generalization of the tensor failure criterion for orthotropic or transversely isotropic laminae and allows for the distinction between tensile and compressive strengths while accounting for the interaction between the normal stresses[4]. It can be given by[91]:

$$F_1\sigma_1 + F_2\sigma_2 + F3\tau_{12} + F_4\sigma_1^2 + F_5\sigma_2^2 + F_6\tau_{12}^2 + 2F_7\sigma_1\sigma_2 = 1 \tag{3.26}$$

Where,

$$\begin{aligned} F_1 &= \frac{1}{\sigma^u_{1T}} + \frac{1}{\sigma^u_{1C}}; \quad F_2 = \frac{1}{\sigma^u_{2T}} + \frac{1}{\sigma^u_{2C}}; \quad F_3 = 0; \\ F_4 &= -\frac{1}{\sigma^u_{1T}\sigma^u_{1C}}; \quad F_5 = -\frac{1}{\sigma^u_{2T}\sigma^u_{2C}}; \quad F_6 = \frac{1}{(\tau^u_{12})^2}; \\ F_7 &= \frac{1}{2\sigma^u_{2T}}\left[1 - (F_1 + F_2)\sigma^u_{2T} - (F_4 + F_5)(\sigma^u_{2T})^2\right] \end{aligned} \tag{3.27}$$

Alternatively, a simpler version of this equation can be written as Sun et al.[90] did:

$$-\frac{\sigma_1^2}{\sigma^u_{1T}\sigma^u_{1C}} - \frac{\sigma_2^2}{\sigma^u_{2T}\sigma^u_{2C}} + \frac{\tau_{12}^2}{(\tau^u_{12})^2} + 2F_{12}\sigma_1\sigma_2 + \frac{\sigma_1}{\sigma^u_{1T}} + \frac{\sigma_1}{\sigma^u_{1C}} + \frac{\sigma_2}{\sigma^u_{2T}} + \frac{\sigma_2}{\sigma^u_{2C}} \leq 1 \tag{3.28}$$

There is still some doubt in the academic community regarding the interaction term, F_7. The admissible range for this parameter that ensures a closed envelope and acceptable inclinations of the tangents to the failure envelopes is different for different materials, however it is generally between -1 and 0. When this term is -1/2, the classical von Mises failure criterion can be recovered if anisotropy is reduced to isotropy and tensile and compressive strengths are equal. Thus, it is recommended, and considered a good approximation, to use this value as $-1/2$ for all materials. Nevertheless, due to the highly orthotropic strength properties of composite materials, strength predictions are practically insensitive to the value of the interaction term. This criterion cannot identify failure modes[92].

3.2.2 Phenomenological failure criteria

This type of failure criteria provide failure envelopes from relatively simple experimental data, that can be used in the design phase of composite structures. Their applicability reaches structures subjected to complex loading. It is rather common replacing non-phenomenological criteria by phenomenological ones, which have a stronger physical basis[93].

Understanding the micro-mechanical damage mechanisms of composite materials is vital for developing physically-based failure theories, because failure is a consequence of the accumulation of micro-level failure events[93].

3.2.2.1 Hashin Criterion

Hashin proposed a set of interactive failure criteria for unidirectional composites that could model failure modes for both two and three-dimensional cases. These criteria were defined in terms of the stress invariants for a transversely isotropic material, rather than evaluating only a single stress component[94].

Originally the criteria contemplated four different failure modes, distinguishing between fibre and matrix failure in either tension or compression. Additional failure indices were added resulting from the extension of the criteria to 3D problems for the out-of-plane transverse stress components[94].

Hashin developed one criterion for fibre composites under a three-dimensional stress state. The matrix failure mode uses a quadratic approach due to both the underestimation obtained from a linear criterion and to the difficulty of dealing with a higher degree polynomial form. Moreover, the shear stress effect is now taken into account in the tensile fibre mode[89]. The Hashin criterion also considers that two different fibre and matrix failure modes occur along two different fracture planes, and not all stress components on the associated fracture plane for each mode are relevant, as only some will contribute to the failure criteria for the failure mode. So, the failure envelope is piecewise smooth, where each smooth line represents a different failure mode. However, it should be noted that Hashin pointed out the quadratic failure criteria for the matrix mode implies the fracture plane is the maximum transverse shear plane and this may not always be true[91].

Fibre failure in tension:

$$\left(\frac{\sigma_1}{\sigma_{1T}^u}\right)^2 + \frac{\tau_{12}^2 + \tau_{13}^2}{(\tau_{12}^u)^2} \leq 1 \qquad or \qquad \sigma_1 \leq \sigma_{1T}^u \tag{3.29}$$

Fibre failure in compression:

$$(\frac{\sigma_1}{\sigma_{1C}^u})^2 \leq 1 \tag{3.30}$$

Matrix failure in tension, $(\sigma_2 + \sigma_3) > 0$:

$$\left(\frac{\sigma_2 + \sigma_3}{\sigma_{2T}^u}\right)^2 + \frac{\tau_{23}^2 - \sigma_2\sigma_3}{(\tau_{23}^u)^2} + \frac{\tau_{12}^2 + \tau_{13}^2}{(\tau_{12}^u)^2} \leq 1 \tag{3.31}$$

Matrix failure in compression, $(\sigma_2 + \sigma_3) < 0$:

$$\left[\left(\frac{\sigma_{2C}^u}{2\tau_{23}^u}\right)^2 - 1\right]\frac{\sigma_2 + \sigma_3}{\sigma_{2C}^u} + \left(\frac{\sigma_2 + \sigma_3}{2\tau_{23}^u}\right)^2 + \frac{\tau_{23}^2 - \sigma_2\sigma_3}{(\tau_{23}^u)^2} + \frac{\tau_{12}^2 + \tau_{13}^2}{(\tau_{12}^u)^2} \leq 1 \tag{3.32}$$

Where τ_{23}^u is the out-of-plane shear strength while τ_{12} is the in-plane shear strength.

3.2.2.2 Puck Failure Criterion

Among the various phenomenological criteria proposed, the Puck criteria have become extremely popular with other theories being developed as an extension to these criteria[95].

The modified Mohr/Coulomb theory for brittle transversely isotropic materials is the basis for the Puck failure criterion for matrix cracking. This criterion uses tractions acting on the fracture plane to assess failure under both transverse tension or compression[95].

The plane of maximum stress effort, for the discovery of which a maximisation problem needs solving, is the one which defines the orientation of the fracture plane. In practice, the definition of this plane is done by changing the orientation of the fracture plane and calculating the failure index. The plane for which the maximum value is recorded is the plane of maximum stress effort[95].

Puck failure criteria, besides the stress level which leads to failure, also provides important information regarding both the fracture mode and the anticipated fracture angle. This information provides a much better assessment of the consequences that transverse (or inter-fibre) failures may have for the laminate[95].

The governing equations for these criteria are as follows[95]:

- Fibre Failure (FF)
  - Tensile
$$\frac{1}{\varepsilon_{fT}}\left(\varepsilon_1 * \frac{\nu_{f12}}{E_{fl}} m_{\sigma f}\sigma_2\right) = 1 \tag{3.33}$$
  - Compression (kinking)
$$\frac{1}{\varepsilon_{1C}}\left|\left(\varepsilon_1 + \frac{\nu_{f12}}{E_{fl}} m_{\sigma f}\sigma_2\right)\right| = 1-(10\gamma_{21})^2 \tag{3.34}$$
- Inter-Fibre Fracture (IFF)
  - Mode A, $\theta_{fp} = 0$
$$\sqrt{\left(\frac{\tau_{21}}{\tau_{21}^u}\right)^2 + \left(1-p_{\perp\parallel}^{(+)}\frac{\gamma_T}{\tau_{21}^u}\right)^2\left(\frac{\sigma_2}{\sigma_{2T}^u}\right)^2} + p_{\perp\parallel}^{(+)}\frac{\sigma_2}{\tau_{21}^u} = 1-\left|\frac{\sigma_1}{\sigma_{1D}}\right| \tag{3.35}$$
  - Mode B, $\theta_{fp} = 0$
$$\frac{1}{\tau_{21}^u}\left(\sqrt{\tau_{21}^2 + (p_{\perp\parallel}^{(-)}\sigma_2)^2} + p_{\perp\parallel}^{(-)}\sigma_2\right) = 1-\left|\frac{\sigma_1}{\sigma_{1D}}\right| \tag{3.36}$$
  - Mode C, $\cos\theta_{fp} = \sqrt{\frac{f_w R_{\perp\perp}^A}{(-\sigma_2)}}$
$$\left[\left(\frac{\tau_{21}}{2(1+p_{\perp\perp}^{(-)}\tau_{21}^u}\right)^2 + \left(\frac{\sigma_2}{\sigma_{2C}^u}\right)^2\right]\frac{\sigma_{2C}^u}{(-\sigma_2)} = 1-\left|\frac{\sigma_1}{\sigma_{1D}}\right| \tag{3.37}$$

Mode A corresponds to a tensile failure, while Mode B corresponds to a shear failure and Mode C to a compressive one. In the nomenclature of image 3.4, S_{21} and Y correspond to τ_{12} and σ_2^u, respectively, in the previous equations. The parameter $m_{\sigma f}$ is the stress magnification factor of the transverse stress for the fibre, whose value depends on the fibre used and is usually 1.3 for glass fibres or 1.1 for carbon ones. For the fibre compression equation, the parameter $(10\gamma_{21})^2$ is an empirical shear correction term, while the terms $p_{\perp\parallel}^{(+)}$ and $p_{\perp\parallel}^{(-)}$ refer to the slopes of the failure envelope (fitted to the experimentally deduced slope) for both positive and negative values for the normal tension, as demonstrated in figure 3.4. The parameter σ_{1D} refers to the stress value for linear degradation[95].

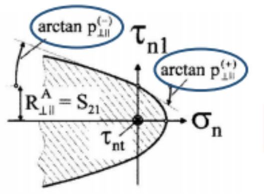

Figure 3.4: Slope of the failure envelope

3.2.2.3 LaRC 05 failure criteria

Another failure criteria developed during World-Wide Failure Exercise (WWFE-II) was LaRC 05. The approach behind this criteria is that failure models and the resulting criteria should include as much information as possible regarding the physics associated with the failure process, however, they should still allow the computing of solutions for laminae and laminates[96].

Matrix Failure

The strengths associated with matrix dominated failure are not material properties, but rather structural ones, as they depend on ply thickness and on the neighboring plies. Indeed, under the same stress state, the conditions for micro-cracks propagation are much more favourable in a unidirectional laminate than in a multi-axial laminate surrounded by 0º plies. Ply thickness and the presence of surrounding plies change the boundary conditions of the fracture mechanics problem for crack growth[96].

Matrix-dominated failure in composites has similarities to that of polymers, however, one difference arises, the need of knowing the fracture angle. Afterwards, an adaptation of Mohr-Coulomb's failure criterion for unidirectional composite plies is used, so the matrix failure index, FI_M, is[96]:

$$FI_M = \left(\frac{\tau_T}{S_T^{is} - \eta_T \sigma_N}\right)^2 + \left(\frac{\tau_L}{S_L^{is} - \eta_L \sigma_N}\right)^2 + \left(\frac{\langle \sigma_N \rangle_+}{Y_T^{is}}\right)^2 \tag{3.38}$$

With failure being predicted when $FI_M = 1$. The terms in equation 3.38 are[96]:

- σ_N, τ_L and τ_T are the traction components in the (potential) fracture plane, according to:

$$\begin{cases} \sigma_N = \frac{\sigma_2+\sigma_3}{2} + \frac{\sigma_2-\sigma_3}{2}\cos(2\alpha) + \tau_{23}\sin(2\alpha) \\ \tau_T = -\frac{\sigma_2-\sigma_3}{2}\sin(2\alpha) + \tau_{23}\cos(2\alpha) \\ \tau_L = \tau_{12}\cos(\alpha) + \tau_{31}\sin(\alpha) \end{cases} \tag{3.39}$$

  Where α is the angle that maximizes FI_M, obtained numerically.

- Y_T^{is}, S_L^{is} and S_T^{is} are the *in situ* transverse tensile strength, longitudinal shear and longitudinal transverse strengths, respectively. These strengths are classified as *in situ*, due to their dependence on the thickness and location of the ply. The formulas for these criteria for the cases in figure 3.5 are on figure 3.6.

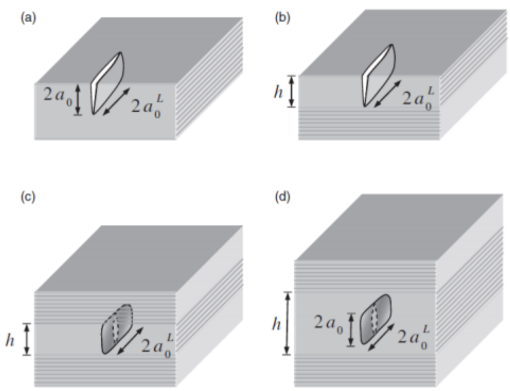

Figure 3.5: Slit crack considered for in-situ effects. (a) Ply in a UD laminate; (b) thin outer ply; (c) thin embedded ply; (d) thick[96]

On figure 3.6, the values G_{IC}, G_{IIc}^L and G_{IIc}^T are the mode I fracture toughness, mode II longitudinal fracture toughness, and mode II transverse fracture toughness, respectively, Y is a geometry-dependent factor, and m is a factor equal to 2 for unstable propagation in the transverse direction, or equal to 4 for unstable propagation in the longitudinal direction. The functions $\xi(\sigma)$ represent the area under the strain versus stress curve up to the point (ε, σ), according to[97]:

$$G_{Ic} = Y\frac{\pi a_0}{m} 4\xi_2(Y_T^{is}) \tag{3.40}$$

$$G_{IIc}^L = Y\frac{\pi a_0}{m} \xi_L(S_L^{is}) \tag{3.41}$$

$$G_{IIc}^T = Y\frac{\pi a_0}{m} \xi_T(S_T^{is}) \tag{3.42}$$

And where[97]:

$$\xi_2(\sigma) = \int_0^{\varepsilon(\sigma)} \sigma_2 d\varepsilon_2 \tag{3.43}$$

$$\xi_L(\tau) = \int_0^{\gamma(\tau)} \tau_L d\gamma_L \tag{3.44}$$

$$\xi_T(\tau) = \int_0^{\gamma(\tau)} \tau_T d\gamma_T \tag{3.45}$$

In which the function $\xi_2(\sigma)$ is achieved through a standard transverse tensile test, $\xi_L(\tau)$ from a longitudinal shear test and $\xi_T(\tau)$ from a transverse compressive one. That being said, these functions are achieved directly from each test rather than from the spline curves with inter- and extrapolation[97].

	Transverse tensile strength		Longitudinal shear strength		Transverse shear strength	
	Linear	Nonlinear	Linear	Nonlinear	Linear	Nonlinear
UD	Y_T		S_L		$S_T = Y_C \cos(\alpha_o)\left(\sin(\alpha_o) + \frac{\cos(\alpha_o)}{\tan(2\alpha_o)}\right)$	
Thick embedded	$1.12\sqrt{2}Y_T$	$\xi_2^{-1}(1.12^2 2\xi(Y_T))$	$\sqrt{2}S_L$	$\xi_L^{-1}(2\xi(S_L))$	$\sqrt{2}S_T$	$\xi_T^{-1}(2\xi(S_T))$
Thin embedded	$\sqrt{8G_{Ic}^L/\pi h\Lambda}$	$\xi_2^{-1}(2G_{Ic}^L/\pi h)$	$\sqrt{8G_{IIc}^L G_{12}/\pi h}$	$\xi_L^{-1}(4G_{IIc}^L/\pi h)$	$\sqrt{8G_{IIc}^L G_{12}/\pi h}$	$\xi_T^{-1}(4G_{IIc}^L/\pi h')$
Thin outer	$\sqrt{4G_{Ic}^T/\pi h\Lambda}$	$\xi_2^{-1}(G_{Ic}^T/\pi h)$	$\sqrt{4G_{IIc}^T G_{12}/\pi h}$	$\xi_L^{-1}(2G_{IIc}^T/\pi h)$	$\sqrt{8G_{IIc}^T G_{12}/\pi h}$	$\xi_T^{-1}(2G_{IIc}^T/\pi h')$

[a]with $\Lambda = 2\left(\frac{1}{E_2} - \frac{\nu_{21}^2}{E_1}\right)$ and $h' = h/\cos\alpha_o$.

Figure 3.6: Formulas for in-situ strengths according to LaRC 05

- The friction coefficients η_T and η_L in equation 3.38 account for the effect of pressure on the failure response, as they increase the shear strengths when a compressive normal load is present, and reduce this parameter when a normal tensile loading is applied in the part. The coefficient η_T is achieved from pure transverse compression test and is dependent of α_0. Several authors observed the fracture angle for glass or carbon composites is typically between 51º and 55º[96].

$$\eta_T = -\frac{1}{\tan 2\alpha_0} \tag{3.46}$$

  Where α_0 is the angle of fracture for uniaxial transverse compression.

  On the other hand, the slope coefficient η_L is an independent material property that must be measured experimentally. That being said, according to LaRC 04 criteria, the relation for η_L proposed is[96]:

$$\eta^L = -\frac{S^L \cos(2\alpha_0)}{Y^C(\cos(\alpha_0))^2} \tag{3.47}$$

  Where S^L is the matrix in-plane shear failure stress.

- The last term represents the effect of the positive normal loading ($\langle\sigma_N\rangle_+$) in opening cracks. The McCauley brackets are defined as $\langle x\rangle_+ = max\{0,x\}$. Therefore, this criterion can be applied for both tensile and compressive matrix failure[96].

Fibre Kinking Failure

When a composite specimen is loaded in compression, matrix splitting can be identified as the result of high shear stresses, which can be induced by failure in the neighbouring plies or due to manufacturing defects, such as fibre misalignments. This splitting is the reason for further bending of the fibres, which, in turn, results in more splitting, until the bent fibres break due to the combination of bending and compressive stresses[96].

According to Grasso[96], before kink bands occur, matrix failure occurs, not necessarily triggered by microbuckling. Fibre kinking results of a shear-dominated matrix failure in a misaligned frame when under significant longitudinal compression. However, if the longitudinal compression is not significant, this failure on the misaligned frame results in fibre splitting, but not necessarily in fibre kinking.

Experimental data for a load combination of longitudinal compression and in plane shear indicate that fibre kinking only takes place if the absolute value of longitudinal compression is greater than $X^C/2$. That being said, for a combination of longitudinal compression and transverse tension, experimental results suggests there is not a formation of kink bands, if the magnitude of the longitudinal compression is lower than X^C[96].

The equation that translates the criteria for fibre kinking and for fibre splitting is[96]:

$$FI_{KINK} = FI_{SPLIT} = \left(\frac{\tau_{23}^m}{S_T^{is} - \eta_T \sigma_2^m}\right)^2 + \left(\frac{\tau_{12}^m}{S_L^{is} - \eta_L \sigma_2^m}\right)^2 + \left(\frac{\langle \sigma_2^m \rangle_+}{Y_T^{is}}\right)^2 \tag{3.48}$$

The two failure modes are then distinguished by the magnitude of longitudinal compression with $\sigma_1 \leq -\frac{X^C}{2}$ resulting in fibre kinking and if this condition is not verified, resulting in fibre splitting. This separation in two failure modes is relevant for the propagation of failure. The parameter X^C is the compressive failure stress[96].

For a better understanding of this phenomena, figure 3.7 provides the physical model for kink-band formation. So, stress rotation equations are for rotation to the kink-band plane ψ[96].

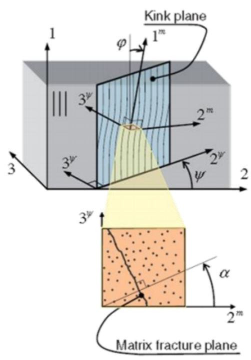

Figure 3.7: Physical model for kink-band formation[96]

$$\begin{cases} \sigma_2^\psi = (\cos\psi)^2\sigma_2 + (\sin\psi)^2\sigma_3 + 2\sin\psi\cos\psi\tau_{23} \\ \tau_{12}^\psi = \tau_{12}\cos\psi + \tau_{31}\sin\psi \\ \tau_{23}^\psi = -\sin\psi\cos\psi\sigma_2 + \sin\psi\cos\psi\sigma_3 + ((\cos\psi)^2 - (\sin\psi)^2)\tau_{23} \\ \tau_{31}^\psi = \tau_{31}\cos\psi - \tau_{12}\sin\psi \end{cases} \tag{3.49}$$

And for the subsequent rotation to the misalignment frame:

$$\begin{cases} \sigma_2^m = (\sin\varphi)^2\sigma_1 + (\cos\varphi)^2\sigma_2^\psi - 2\sin\varphi\cos\varphi\tau_{12}^\psi \\ \tau_{12}^m = -\sin\varphi\cos\varphi\sigma_1 + \sin\varphi\cos\varphi\sigma_2^\psi + ((\cos\varphi)^2 - (\sin\varphi)^2)\tau_{12}^\psi \\ \tau_{23}^m = \tau_{23}^\psi\cos\varphi - \tau_{31}^\psi\sin\varphi \end{cases} \tag{3.50}$$

Where:

- ψ is the angle of the kink band and is in the range $[0,\pi[$ to maximise the failure index[96];
- φ is the misalignment angle, which is defined as the sum of the initial misalignment angle originated from manufacturing defects, φ^0, and the shear strain expressed in a coordinate system aligned with the manufacturing defect, γ_m^0[96].

$$\varphi = sign(\tau_{12}^\psi)\varphi^0 + \gamma_m^0 \tag{3.51}$$

The strain γ_m^0 is a function of the shear stress, τ_m^0, while the initial misalignment angle, φ^0 is a material property obtained from the longitudinal compressive strength:

$$\varphi^0 = \varphi^c - \gamma\left(\frac{1}{2}\sin(2\varphi^0)X_C\right) \tag{3.52}$$

With:

$$\varphi^c = \arctan\left(\frac{1 - \sqrt{1 - 4\left(\frac{S^L}{X^C} + \eta^L\right)\left(\frac{S^L}{X^C}\right)}}{2\left(\frac{S^L}{X^C} + \eta^L\right)}\right) \tag{3.53}$$

Fibre Tensile Failure

The equation for the fibre tensile failure according to this criteria is a non-interactive maximum allowable stress criterion, which, despite its simplicity, provides accurate results[96]:

$$FI_{FT} = \frac{\langle\sigma_1\rangle_+}{X_T} \tag{3.54}$$

Where X_T is the tensile failure stress.

3.3 Materials

In the numerical model, a hybrid fibre was used, so as to answer to Frezite High Performance's client requirements, namely those regarding the modulus of elasticity in compression and the ultimate compressive strength. In order to comply with these requirements one part of a high modulus fibre, Torayca M55J, was mixed with one part of a high strength one, Torayca T1100G.

To define the hybrid fibre's properties, the rule of mixtures was used. This rule was chosen as a result of the celerity with which an accurate result can be achieved, especially for the longitudinal Young Modulus, which was the most important parameter due to the used layup and the stresses to which the tube will be subjected to when in service. Moreover, the error for the transverse tensile strength tends to be by default, and not by excess[84].

The Engineering constants (longitudinal and transverse Young Modulus, Shear Modulus and Poisson Coefficient) defined in the model for Torayca M55J were based both on the data-sheet provided by the manufacturer and on the estimated values for this fibre in ESAComp's database, due to the lack of some information by the manufacturer. For Torayca T1100G, the manufacturer also only provided information about the longitudinal Young Modulus[98], so the transverse Young Modulus, the Shear Modulus and the Poisson Coefficient were estimated based on the relations between each of these properties and the corresponding longitudinal Young Modulus for the various Torayca fibres from the T-series (high strength), whose properties are available in ESAComp (T300, T300J, T400H, T700G, T700S, T800H, T800S and T1000G).

Afterwards, and as already mentioned, the rule of mixtures was applied to both these fibres in order to define the properties of the hybrid fibre. In order to define the out-of-plane shear modulus, an analysis between the ratio of the out-of-plane shear modulus and longitudinal Young's Modulus for fibres with a similar value for Young's Modulus as the hybrid fibre was performed in order to assess an average value for this property for fibres with a high Young's Modulus, due to the lack of information regarding this property. This ratio was then multiplied by the hybrid fibre's longitudinal Young Modulus to achieve the values for the out-of-plane shear modulus. The fibres used for this comparison were: Cytec Thornel T-300, T-650/35, T-650/42 and Torayca T300. The properties of the hybrid fibre and its components are in table 3.1.

Table 3.1: Properties of the fibres [98]

Fibre	**Density** $[Kg/m^3]$	**Longitudinal Young's Modulus [GPa]**	**Transverse Young's Modulus [GPa]**	**In-Plane Shear Modulus [GPa]**	**Poisson Coefficient**	**Out-of-Plane Shear Modulus [GPa]**
M55J	1910	540	8.3	17.5	0.18	-
T1100G	1790	324	30	50	0.22	-
Hybrid	1850	432	19.15	33.75	0.2	8

Regarding the matrix, the value for the Young Modulus was defined according to the data-sheet[15], while the Shear Modulus and the density were defined as being the same as the one available in ESAComp for the same resin (Araldite LY556), but for a different hardener (HY907, as opposed to HY906), and a different accelerator (DY063, as opposed to DY070) than the ones which will be used in the manufactured tubes. The resin properties are exposed in table 3.2.

Table 3.2: Properties of the resin[15]

Matrix	Density $[Kg/m^3]$	Young's Modulus [GPa]	Shear Modulus [GPa]	Poisson Coefficient
Araldite LY556/ HY906/DY070	1260	3	1.24	0.21

3.4 Ply Properties

After defining the fibre and matrix to be used, it was proceeded to defining the ply and its properties. In order to determine the best parameters, a FVF of 65% was chosen, based on previous investigation done by Frezite High Performance, with values in the range 60% to 65% expected to provide the best combination of mechanical properties for a compressive load (Young's Modulus and ultimate strength), which is expected to be the most critical. ESAComp was used for the definition of the ply properties, and the micromechanical model chosen was the Halpin-Tsai, with $\xi = 2$, due to this being a common value for this parameter, however, in the future, validation of this parameter should be done with experimental tests of unidirectional specimen to develop a more accurate model. The ply properties are in figure 3.8.

As a result of the lack of knowledge about the exact mechanical properties of both the fibres, the matrix and the ply properties, the definition of these parameters, and consequently the laminate properties may be affected with significant error, so care must be taken while assessing the results. Owing to this, the results presented in the simulation should be assessed with caution. That being said, these properties should resemble the ones for the manufactured tube, so an analysis regarding the validity of each test can be done, and the results should be valid for that assessment.

```
t = - mm      m_A =        - g/m²      V_f  =    65%
              rho  = 1643.5 kg/m³      f_1/2 = 100/0%

Engineering constants (transv.is.23)

E_1 = 281.85 GPa     G_12 = 6.96378 GPa     nu_12 = 0.203387
E_2 = 11.326 GPa     G_31 = 6.96378 GPa     nu_13 = 0.203387
E_3 = 11.326 GPa     G_23 = 4.66244 GPa     nu_23 = 0.214597
```

Figure 3.8: Ply Properties of Ply with FVF=65%

3.5 Laminate Properties

After defining the ply properties, the laminate ones can be defined, provided the angle and thickness of each ply is defined. In the case considered, the laminate followed the structure [$\pm$10º/$\pm$10º/ $\pm$85º/$\pm$10º/$\pm$10º] relative to the longitudinal direction of the tube, where the plies with an angle of $\pm$10º have a thickness of 0.18 mm, while the plies with an angle of $\pm$85º have a thickness of 0.14 mm. It is important to mention that the tubes provided by Frezite High Performance are rectified in order to achieve an exterior diameter of 16mm. This process is critical, and is impacted by the accuracy of the production, as if the tubes are too uneven before rectification, layers of carbon fibre may be damaged in this process, which, in turn, has a significant impact on the mechanical properties of the tube. During experimental testing this is a factor to be on the look-out for, if one tube presents results significantly lower than the remainders.

3.6 Four-Point Bending

In order to define and simulate this test, an analysis of the ASTM D6272[99] standard was done in order to adapt it for a tubular specimen. This process needed to be done as the standard has been designed for testing flat laminate specimen, so the loading noses and the supports are cylinders, to maintain the distance between supports with the movement of the specimen, while keeping a good contact with the latter. When changing the specimen shape from a flat laminate to a cylinder, several challenges arise, namely the crushing which occurs due to the contact between the loading nose and the tube being done only in one point, assuming geometrically perfect interactions.

With the purpose of solving this issue, some simulation attempts were made, based on the experiments already present in the literature. The first followed the ASTM D6272[99] for laminates, the second followed the same approach as Saggar[100] did while performing his master thesis, and inserted a polymeric "cushion" between the tube and the noses/supports, so that the contact area would increase, thus mitigating crushing and avoid damaging the tube's surface due to stress concentrations during loading. This setup is portrayed in figure 3.9.

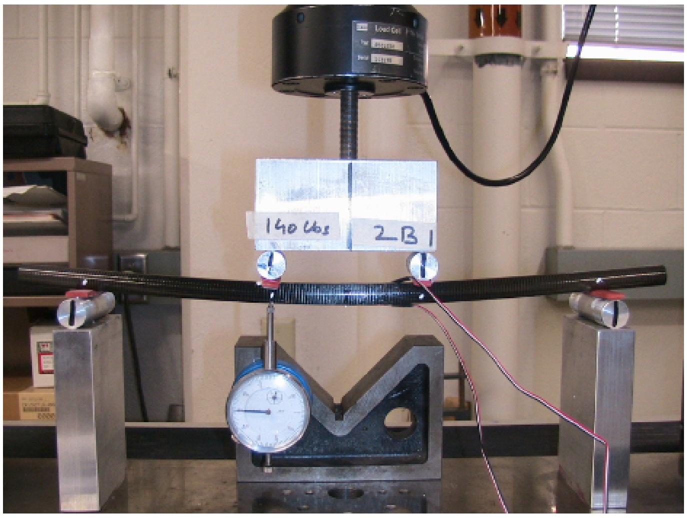

Figure 3.9: Setup developed by Saggar[100]

Afterwards, and as with the latter example the problem was not solved, an experiment with a loading accessory which increased the contact area by replicating the outer geometry of the tube was done, similarly to what Yang[101] studied. The approach followed by Yang[101] is on figure 3.10, while on figure 3.11 it is possible to observe the dimensions of the used support. It should be mentioned the simulation was also done for a four-point bending test, not only for a three-point one, as Yang[101] did.

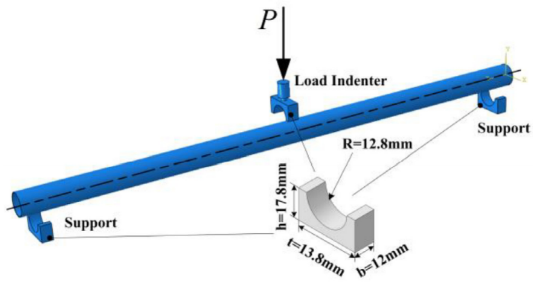

Figure 3.10: Loading noses and supports used by Yang et al.[101]

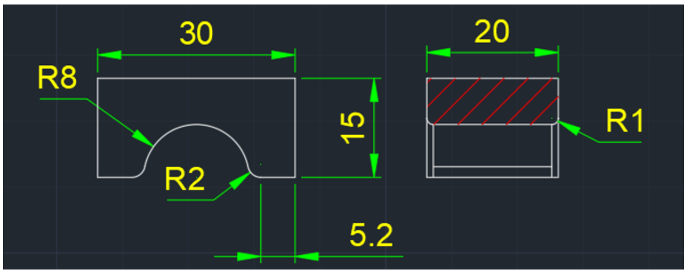

Figure 3.11: 2D Drawing of the used support

One other constraint imposed by the FHP's client was the need of testing the tubes at room temperature and at both extreme operational temperatures, the minimum, -77.5ºC, and the maximum, 90.5ºC. This condition meant the length of the tubes was limited to 300mm, due to the hot/cold chambers' size.

In figure 3.12, it is possible to see the approach taken to solve this problem. It should be mentioned for the second approach only the upper span (US in figure 3.12) of 125mm was considered as the results did not improve enough to justify further simulations. In both first and third approaches, the lower span was 250 mm, and the upper span was alternated between 125 mm (half of 250mm), 83,3mm (one third of 250mm), and a three-point bending test. The choice of these values will be explained in the following paragraphs.

Considering the limit already established for the tube's length of 300mm, the next step was defining the lower and upper spans. In the standard, it is stated there must be an overhang in each side of the tube of at least 10% of the support span. Moreover, the standard also states the span-to-depth ratio should be 16:1 or, if break does not occur in the section where the specimen is subjected to the greater loads, the area between the upper supports, a greater ratio should be chosen, for example 32:1. These ratios apply for specimens whose thickness is equal to or greater than 1.6mm.

On a first analysis, if we consider the depth as the outer diameter of the tube, a span of 256 mm ($16 * 16 = 256$) is achieved. Due to the need of having a 10% overhang, and to comply with the maximum length supported by the chambers, the lower span was corrected to 250mm. An

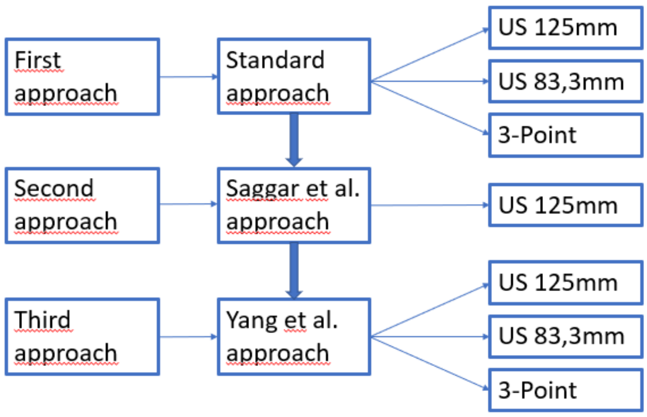

Figure 3.12: Diagram of the analysis sequence

analysis regarding the moment of inertia of our section (hollowed tube with an outer diameter of 16mm and a thickness of 1mm) resulted in a value of $1608.5mm^4$, while the moment of inertia for a rectangular section with a profile of $8mm * 38mm$ is $1621.33mm^4$, similar to the one presented by our tube. Considering this last equivalent specimen, and the support span of 250mm, the span-to-depth ratio is 31.25 ($31.25 * 8mm = 250mm$), a safe value according to the standard. If we change the profile dimensions of the equivalent test specimen to $6.5mm * 70mm$, the inertia moment is $1601.98mm^4$, which, for a support span of 250mm, results in a span-to-depth ratio of 38:1 ($38 * 6.5mm \approx 250mm$). Both these specimen are represented on figure 3.13

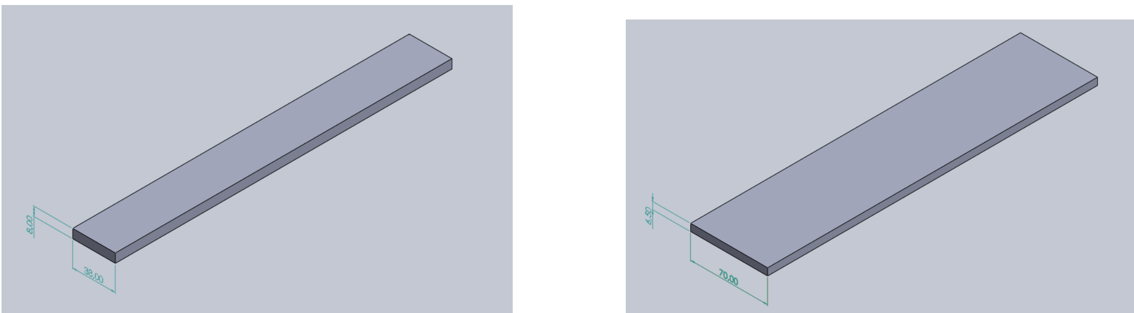

(a) $8mm * 38mm$ Specimen

(b) $6.5mm * 70mm$ Specimen

Figure 3.13: Dimensions for both equivalent specimen

In each of the three models, the loading noses and supports where modelled as being rigid, which is an approximation of reality. However, the material chosen for the loading noses and supports would be extremely rigid, so would result in an acceptable simulation of the test. Furthermore, the friction coefficient used was 0.3 as did Melo[102] in his work when simulating impact tests on carbon reinforced composites. The test was modeled only considering the elastic domain of the material owing to the extreme stiffness and brittleness of the material, which meant the plastic domain could be disregarded, and the failure criterion used was the maximum strain for the high modulus fibre due to:

- **Model Simplicity** - The simplicity of the part considered (tube), and as the load was applied only in one direction, the need for extremely advanced criteria could be disregarded;

- **Ease and rapidness of analysis** - This is a direct method for assessing failure, and as a first approach it provides reasonable results. A more accurate criterion would be used further along.

In order to replicate the test, two boundary conditions were defined. The first was regarding the lower supports, whose displacement was blocked and only a rotation along the axis perpendicular to the plane represented in figure 3.14 was allowed. The second was regarding the upper noses, which experienced a displacement (in the negative direction) of 10 mm whilst only being free to rotate along the same axis the lower supports were able. The remaining displacements and rotations were also blocked. This methodology has already been experimented and proved by Moshir et al.[103] for carbon/PEEK tubes.

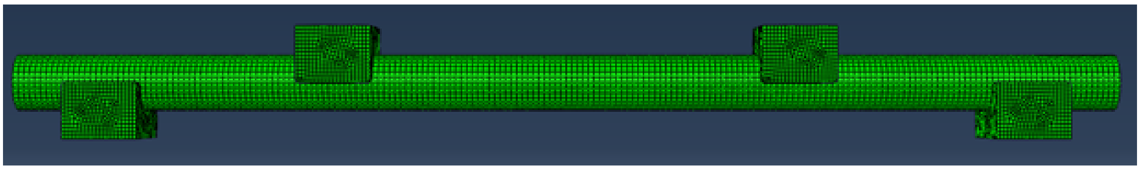

Figure 3.14: Assembly Four-Point Bending

Two meshes where used in order to assess the result's validity and to understand if a smaller one should be used to provide more accurate results that could be replicated in practice. In table 3.3 a summary of the mesh size used in each part is presented. The mesh size used in the supports was not changed due to our focus being the tube, and no contact problems arose. Furthermore, this mesh size used for each part seemed appropriate, considering the convergence of the results. The mesh elements used for both meshes are in table 3.4. It should be mentioned that in both tables the column on the right, regarding the "cushion" mesh size, should only be considered for the second approach.

Table 3.3: Mesh size used

Mesh	**Tube's Mesh Size**	**Support's Mesh Size**	**"Cushion" Mesh Size (Second Approach)**
A	1.5	1	1
B	2	1	1

Table 3.4: Mesh elements used

Mesh	**Tube's Mesh Element**	**Support's Mesh Element**	**"Cushion" Mesh Size (Second Approach)**
A	S4R	R3D4	C3D8R
B	S4R	R3D4	C3D8R

In the analysis that will be performed after each setup is presented several parameters will be mentioned:

- **Force** - This term will refer to the vertical force the supports will apply in the tube. It will be expressed in [N], unless otherwise stated;
- **Displacement** - This term will refer to the displacement measured in the vertical axis in [mm], unless otherwise stated;
- **Stress** - This term will refer to the stress experienced in the tube. It will be measured along the longitudinal axis of the tube in [MPa], unless otherwise stated;
- **Strain** - This term will refer to the strain experienced in the tube. It will be measured along the longitudinal axis of the tube in [%], unless otherwise stated;
- **Tube mid-point** - This designation refers to two different points. Both of them are located halfway between each end of the tube, and both are in the outer layer of the CFRP, where the experienced stress should be the highest. However, one is on the bottom part of the tube (tube mid-point tensile), subjected to a tensile loading (point marked as *RP* on figure 3.15a), and the other is on the upper part of the tube (tube mid-point compressive), subjected to a compressive loading (point marked as *RP* on figure 3.15b);

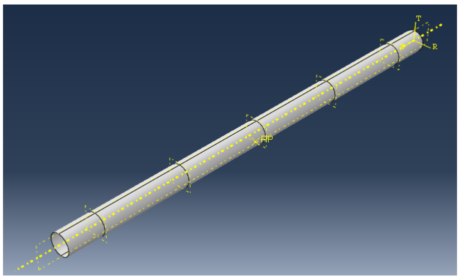

(a) Tube mid-point in a tensile loading

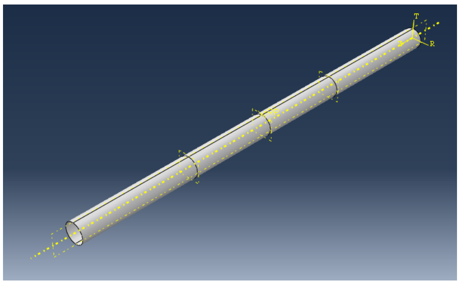

(b) Tube mid-point in a compressive loading

Figure 3.15: Tube mid-point

- **Support/Punch mid-point** - This point corresponds to the one where the load is applied in each support. It is located in the middle of each support. It is the point marked as *RP* on figure 3.16.

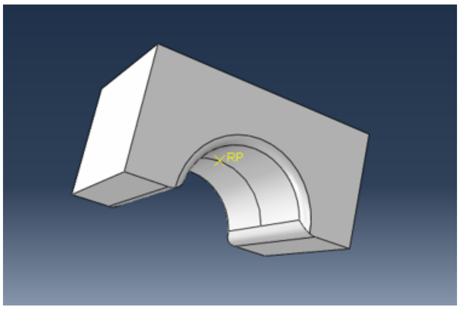

Figure 3.16: Support mid-point

3.6.1 First Approach

The first approach consisted of establishing a setup which was similar to the one presented in ASTM D6272[99], but in which the specimen was a CFRP tube, rather than a flat specimen.

3.6.1.1 First Solution

This solution consisted of establishing the lower span as 250mm, and the upper span as 125mm, which is half of the former, one of the options mentioned in the standard. In figure 3.17, a drawing of the setup is displayed, while in figure 3.18 it is possible to assess a comparison between the strain along the longitudinal direction experienced in the points in which the support contacts with the tube and the tube mid-points with time, as a fraction of the total time of the simulation for both meshes. The strain for the right load application point is not visible due to the overlap between the strain at this node and the one at the left load application point, as well as there is an overlap between the tube mid-points subjected to a compressive loading (upper side of the tube), and to a tensile one (bottom side of the tube). In these graphics, the values labeled as "(Mirror)" inform the reader that despite the strain results being represented as positive, the experienced strain at the node is a compressive one, thus a negative value is measured. These data correspond to the outer layer of CFRP.

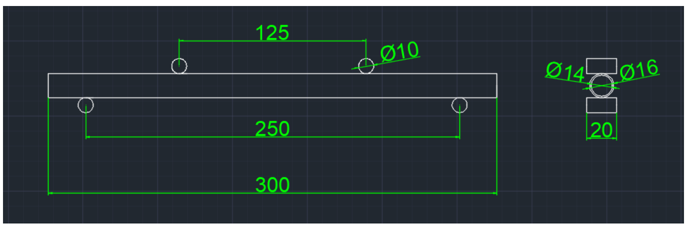

Figure 3.17: Setup for the first solution of the first approach

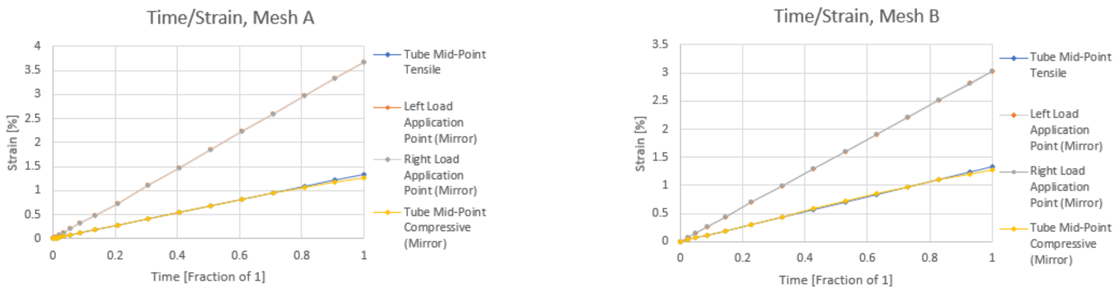

(a) Mesh A (b) Mesh B

Figure 3.18: Comparison between the Engineering Strain for the first solution for the first approach

3.6.1.2 Second Solution

This solution consisted of establishing the upper span as 83.3mm, while keeping the lower one as 250mm, thus establishing a relation between the upper and lower spans of one third. Figure 3.19 portrays this setup and in figure 3.20 a comparison between the strain experienced along the longitudinal direction at the points in which the support contacts with the tube and the tube mid-points with time, as a fraction of the total time of the simulation is presented. These figures portray this relation for the two different meshes used for the outer layer of the composite.

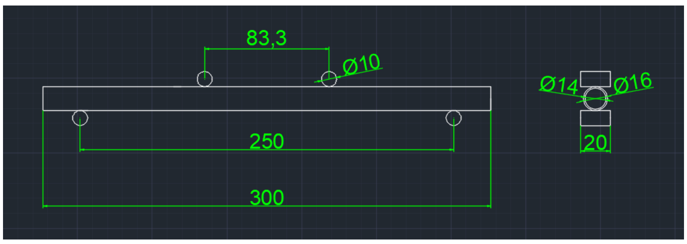

Figure 3.19: Setup for the second solution of the first approach

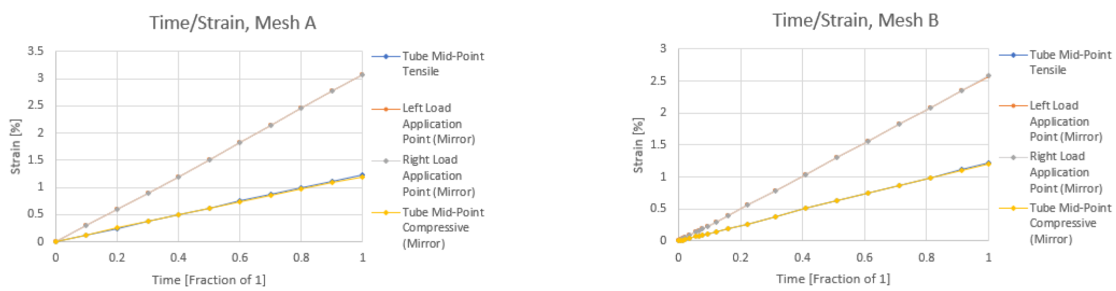

(a) Mesh A (b) Mesh B

Figure 3.20: Comparison between the Engineering Strain for the second solution for the first approach

3.6.1.3 Third Solution

The last solution attempted for this approach was a three-point bending test, rather than a four-point one, in which the lower span was kept the same as before, 250 mm, as is in figure 3.21. In figure 3.22, it is possible to assess a comparison between the strain along the longitudinal direction experienced at the point in which the support establishes contact with the tube, which is the upper tube mid-point, and the bottom tube mid-point, with time, as a fraction of the total time of the simulation for both meshes for the outer layer of the composite.

Figure 3.21: Setup for the third solution of the first approach

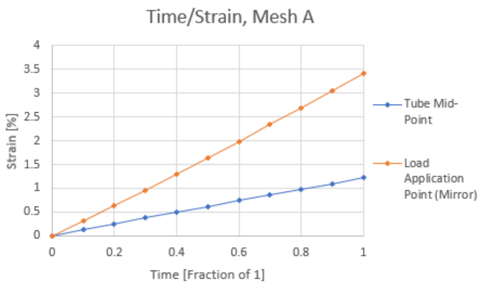

(a) Mesh A

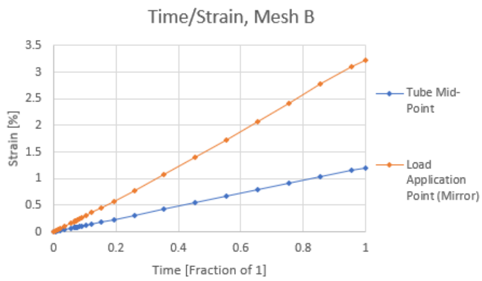

(b) Mesh B

Figure 3.22: Comparison between the Engineering Strain for the third solution for the first approach

3.6.1.4 Results comparison

Through the application of the maximum strain criterion for the high modulus fibre, which has a maximum admissible strain of 0.8%, to figures 3.18, 3.20 and 3.22, it is easy to assess the strain along the loading nodes is much greater than the one experienced at the tube mid-point for any given time-frame, which means, according to the maximum strain criterion, the tube will break at the loading points due to crushing, before breaking at the tube mid-point, thus invalidating this setup. Furthermore, it can be seen that in this approach there is no clear advantage in reducing the support span to reduce crushing.

3.6.2 Second Approach

This approach consisted of modelling a setup similar to the one used by Saggar et al.[100], which consisted of using a polymeric "cushion" that could adapt both to the support's and the tube's geometry, thus improving the force transmission between these two parts and reducing the crushing of the previous approach. The material used for this "cushion" was a thermoplastic resin, Polytetrafluoroethylene, commonly referred to as PTFE or Teflon, filled with glass fibre with a weight percentage of 25%. This was the chosen material due to its low Young Modulus and high service temperature range, which could cope with temperatures as low as -77.5ºC and as high as 90.5ºC, thus not causing problems in any of the tests, and not becoming brittle along the temperature change, despite the matrix being a thermoplastic resin.

Regarding the material properties, the inputted ones were generic, without defining the manufacturer, and consequently without defining the exact properties. This effort would be done afterwards, if the simulation results proved promising. The values which were used as inputs in this simulation were taken from Granta EduPack[104] and are in table 3.5. The remaining properties for the model were kept the same as for the previous approach, namely the properties and the layup of the CFRP, the tube's dimensions and the friction coefficient.

Table 3.5: PTFE (25% Glass Fibre) Properties[104]

Property	Value
Young's Modulus	1650 MPa
Poisson Ratio	0.42
Maximum service temperature	260ºC
Minimum service temperature	-200ºC

The setup used was equivalent to the one in the first solution of the first approach, that is, the lower supports were 250mm apart, while the upper noses had 125mm between themselves. However, between the supports and the tube was the already mentioned "cushion". Naturally these distances are centered at the middle of the tube, as is demonstrated in figure 3.23.

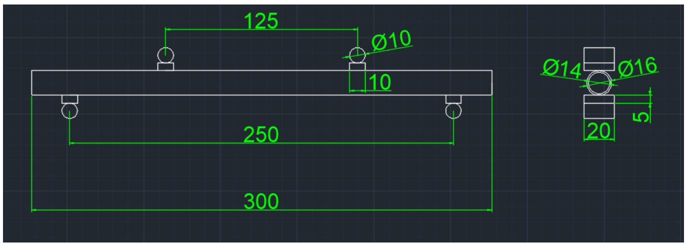

Figure 3.23: Setup for the second approach

In figure 3.25, it is possible to assess the strain experienced at some nodes on the outer layer with time. The label of the nodes referenced in these figures are on figure 3.24. Nevertheless, it should be mentioned the left and right application points are the nodes immediately below the punch mid-point, while the nodes defined with a number are the ones where the outer side of the "cushion" contacts with the tube and, at that point, some stress concentration is verified, as seen in the graphics below. Another important consideration is the fact the curves of the left and right application points overlap each other, thus only one line can be identified in the graphic, despite both being inputted. The same occurs with nodes 107 and 286, and nodes 142 and 383, and with both tube mid-points. In these graphics, the values labeled as "(Mirror)" inform the reader that despite the strain results being represented as positive, the experienced strain at the node is a compressive one, thus a negative value is measured.

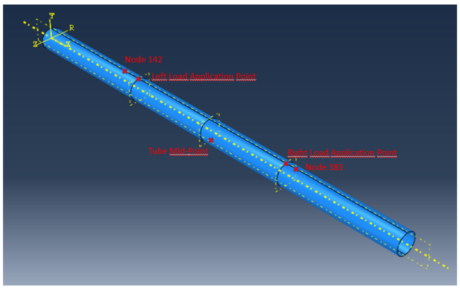

(a) Mesh A

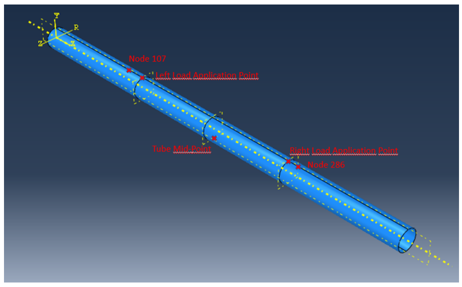

(b) Mesh B

Figure 3.24: Relevant Nodes for the analysis of the second approach

Through the analysis of figure 3.25, and applying the maximum strain criterion, it is clear that for whichever fraction of time we are considering, the strain at the nodes where the contact is greater between the "cushion" and the tube are the ones which experience the larger strain, thus are the ones which fail first. This leads to the conclusion that the approach here discussed is not as promising as previously thought and another one should be elaborated.

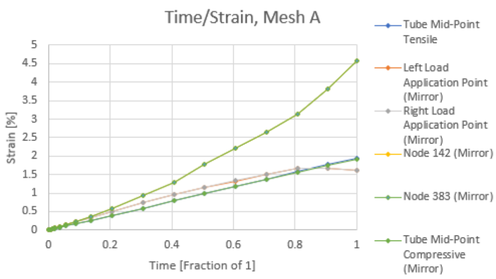

(a) Mesh A

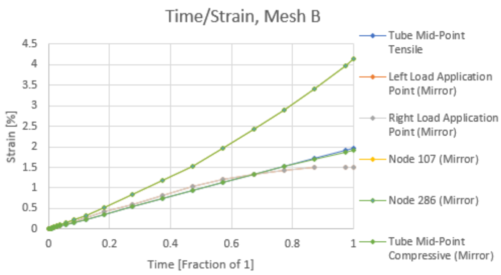

(b) Mesh B

Figure 3.25: Comparison between the Engineering Strain for the first solution of the second approach

3.6.3 Third Approach

This approach consisted of three different solutions, in which the displacement and rotation conditions were applied to the supports represented in figure 3.11. The lower span was kept the same for all three solutions here portrayed, 250mm as did the tube length, which was 300mm.

3.6.3.1 First solution

This solution consisted of establishing the lower span as 250mm and the upper span as 125mm, corresponding to half of the lower one. In figure 3.26, it is possible to observe a drawing of the setup.

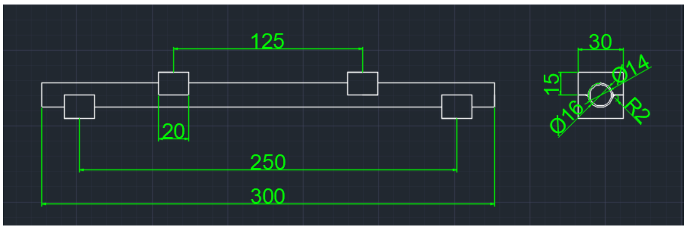

Figure 3.26: Setup of the first solution of the third approach

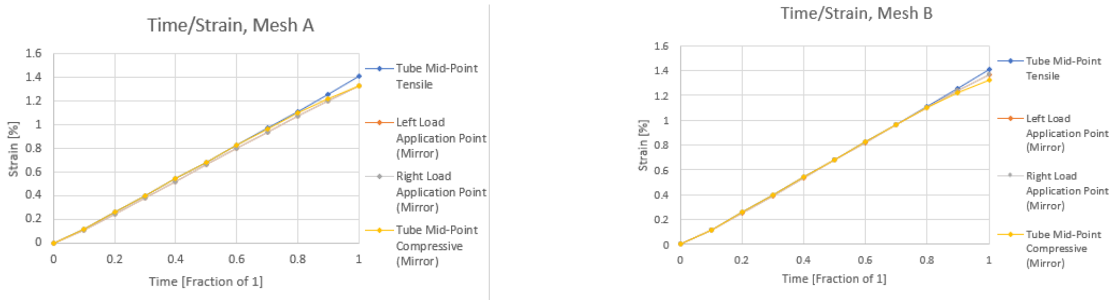

(a) Mesh A (b) Mesh B

Figure 3.27: Results for the relation time-strain for both meshes for the first solution

In figure 3.27, a comparison between the strain experienced at both the tube mid-points and the load application points with time is shown. Here, it can be seen for each time frame the strain experienced at both tube mid-points is higher or similar than the one at the load application points. Despite the difference not being as high as desired, for a greater degree of confidence, according to the maximum strain criterion, the test would be valid. It should also be mentioned that these data correspond to the outer layer of the composite, due to it being the one which fails first and which withstands the greater stress as it is the further away from the neutral axis.

3.6.3.2 Second solution

The second solution, which is portrayed in figure 3.28, consisted of using a lower span of 250mm while the upper span was 83.3mm (one third of 250mm). The tube length was kept the same, 300mm.

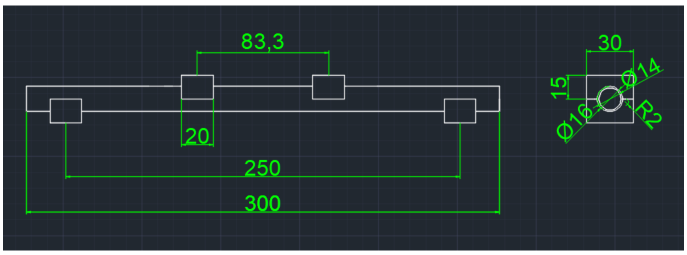

Figure 3.28: Setup of the second solution for the third approach

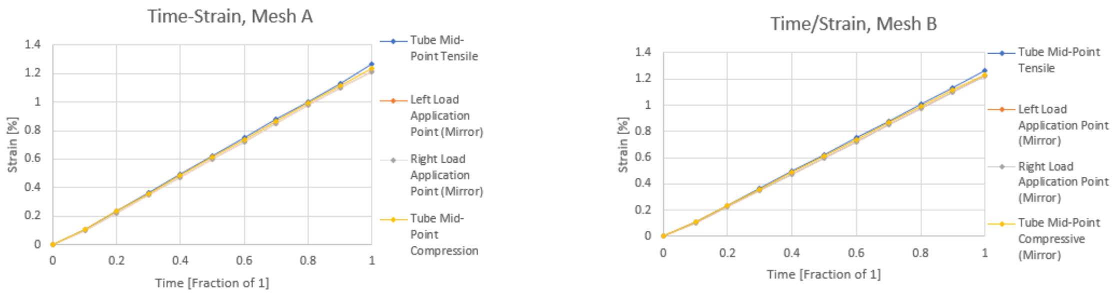

(a) Mesh A (b) Mesh B

Figure 3.29: Results for the relation time-strain for both meshes for the second solution

In figure 3.29, it is possible to analyze a comparison between the strain at both the tube mid-points and the point where the support establishes contact with the tube. Here, it can be seen for each time frame, the strain experienced at the tube mid-points is, again, higher or similar to the one at the load application points. The data here presented has also been collected from the outer layer, as it is the most critical one, and the one which should fail first.

3.6.3.3 Third solution

Finally, and due to the progression of the results, a third solution consisting of a three-point bending setup was simulated. The tube length and the lower span was kept the same.

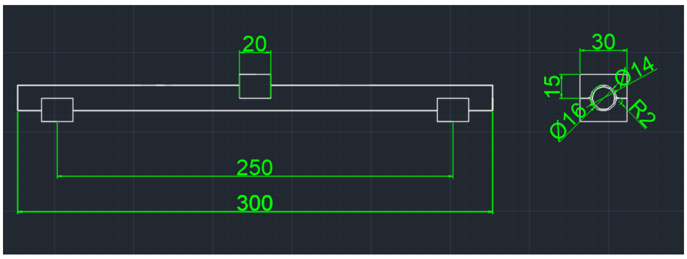

Figure 3.30: Setup of the third solution for the third approach

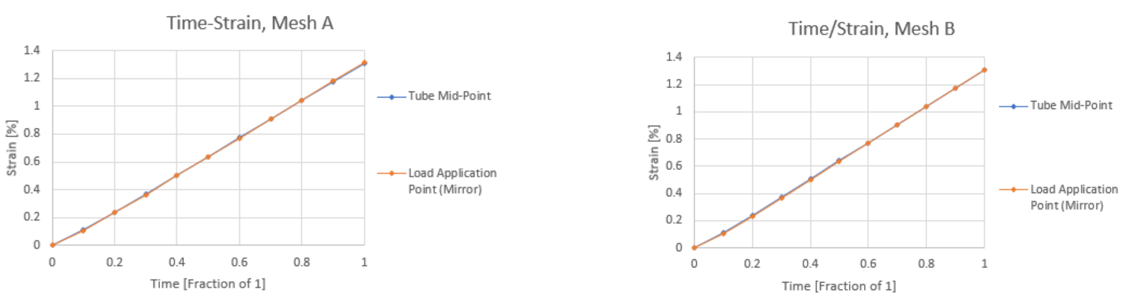

(a) Mesh A (b) Mesh B

Figure 3.31: Results for the relation time-strain for both meshes for the third solution

Figure 3.31 shows the evolution of the strain experienced at both the tube's bottom mid-point and the node where the tube and the support interact with each other, which is also the tube's upper mid-point. Here, there is an overlap between the strain at both the contact point, and at the tube mid-point in the area subjected to tension, thus this setup is less likely to provide the best results. The results here presented are for the outer layer, for the reasons already mentioned.

3.6.3.4 Results comparison

First of all, it is important to understand this approach is portrayed as more viable to provide valid results, in which the specimen breaks between the loading noses, either in the upper or lower side of the tube. This is acknowledged in figures 3.27, 3.29 and 3.31, in which a comparison between the strain experienced at the tube mid-points (both on the area subjected to tension and on the area subjected to compression) and at the load application points with time is shown. It must be stated the time axis is represented as part of the duration of the test, as this is a static analysis. Here, it is clear the tube mid-points experiences a similar or a greater strain (depending on the setup) in each frame than the points where the load is being applied. Thus, and especially in the four-point bending simulations, it is clear that according to the maximum strain criterion, failure would occur at the tube mid-points rather than due to crushing, despite the load needed to achieve each strain value would be greater (see figures 3.32 and 3.33). Furthermore, opting for a four-point bending simulation rather than a three-point one also allows for the maximum stress to be experienced in a greater area, and allows for an easier assessment of valid and invalid (those whose rupture is due to crushing on the application points) tests. One other advantage of choosing the four-point test rather than the three-point one, is that only in the former is possible to evaluate the compressive domain of the tube, as in the three-point bending one, failure by compression and crushing would be indistinguishable. For these reasons, the experimental test will be a four-point bending one.

The following graphics portray the relations between the different solutions for the third approach, which was the most promising one.

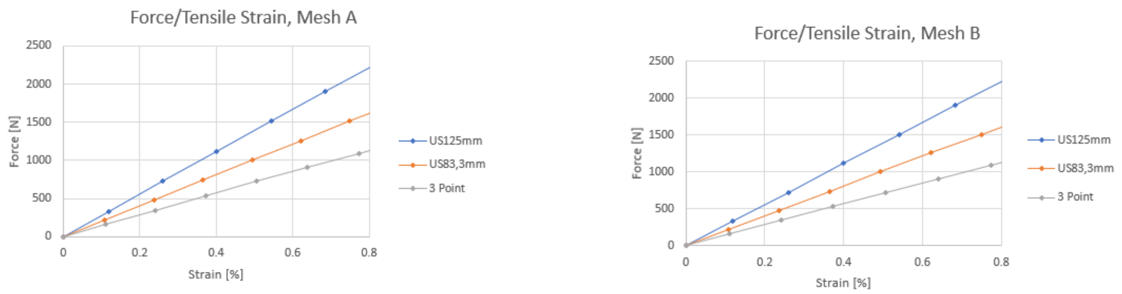

(a) Mesh A (b) Mesh B

Figure 3.32: Force/Tensile Strain

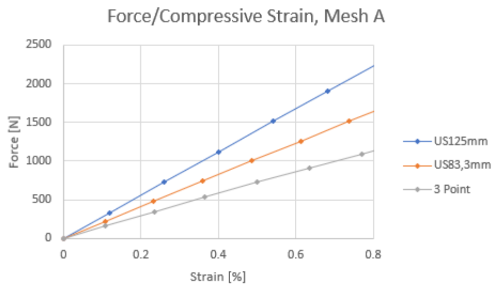

(a) Mesh A

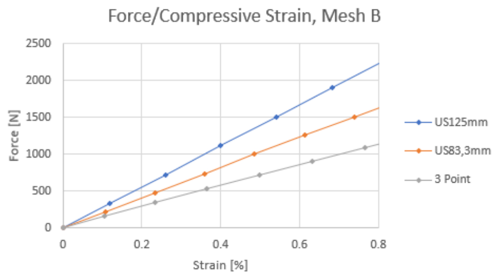

(b) Mesh B

Figure 3.33: Force/Compressive Strain

On figure 3.32 and 3.33, a Force/Strain analysis is done for both meshes and for the areas subjected to either tensile or a compressive loading. It must be said, the points chosen for this measure were the ones on the middle of the tube for the outer layer, so for the three-point bending test the load application point and the point subjected to compressive loading is the same. Here, it can be seen that the higher the loading span, the higher the force needed to break the specimen, however, in every case, the specimen would break before a load of 3 kN is applied.

3.6.4 Experimental Setup

After analysing all the approaches previously exposed, the final setup was developed. It was based on the first solution of the third approach, however, some adjustments were made to further enhance the confidence of having a successful test. The support span was increased from 250mm to 260mm to further enhance the span-to-depth ratio. With this support span, and comparing with the equivalent specimen defined in the beginning of this section, ($8mm*38mm$ and $6.5mm*70mm$), the span-to-depth ratio would be 32.5 ($32.5*8mm = 260mm$) and 40 ($40*6.5mm = 260mm$), respectively, thus increasing the probability of a successful test. It is true that choosing this span violates the condition of at least 10% overhang in each side of the tube (the overhang would be 8% in each side), however, due to our tube's stiffness, this small decrease in overhang is not expected to cause any problem. The previous results and a physical interpretation of the problem proved the test had a greater likelihood of succeeding when the upper span was half of the lower one, thus the upper span was set to 130mm.

The supports also had some modifications compared to the one used for the third approach, so as to establish better contact with the tube and avoid tension concentrations on its side. The 2D drawing of the used setup is portrayed in figure 3.34. The remaining parameters of the simulation were kept the same as for the first solution of the third approach. With this support, the contact area between the tube and the support correspond to an arc of $19.55mm$ (140º) by $19mm$ in length, totalling an area of $371.5mm^2$, as represented in figure 3.35.

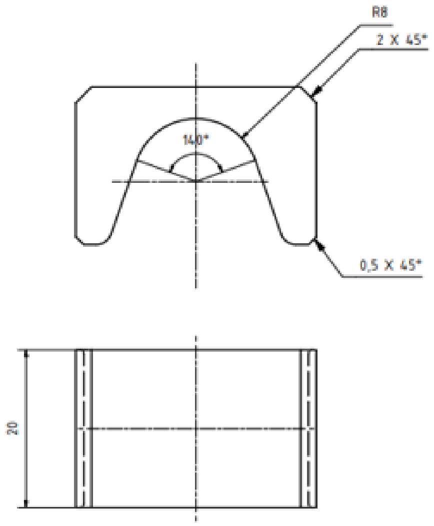

Figure 3.34: Support used in the experimental setup

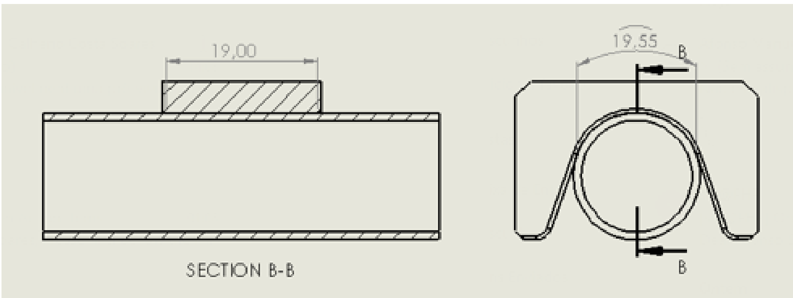

Figure 3.35: Contact area between support and tube

Regarding the material, in order to have a more accurate prediction of the material's behaviour the inverse rule of mixtures with $\alpha = 1$ was used for the definition of the hybrid fibre's properties and afterwards, through ESAComp and the Halpin Tsai model with $\xi = 2$, the properties of the ply were defined, as are in figure 3.36. The layup used was the same as for the other simulations.

t = - mm   V_f = 65%
f_1/2 = 100/0%

No mass data specified!

Engineering constants (transv.is.23)

E_1 = 264.3 GPa	G_12 = 6.79458 GPa	nu_12 = 0.202087
E_2 = 10.009 GPa	G_31 = 6.79458 GPa	nu_13 = 0.202087
E_3 = 10.009 GPa	G_23 = 4.12032 GPa	nu_23 = 0.21459

Figure 3.36: Ply used in the simulation of the experimental setup

Moreover, the Hashin failure criteria were used in ABAQUS^{TM}. This was done to have a more accurate prediction about the failure however, one issue arose, the fact no tests have previously been done by FHP for this composite, and no tests have been found in the literature, thus some adjustments had to be made which, naturally, increased the error of this approach, so the results should be interpreted with caution. The values used for the failure criterion are on table 3.6.

Table 3.6: Failure Properties

Property	**Value [MPa]**
Tensile Longitudinal Stress	2419
Compressive Longitudinal Stress	1155
Tensile Transverse Stress	85
Compressive Transverse Stress	200
Longitudinal Shear Stress	69
Transverse Shear Stress	87

The values for the tensile and compressive longitudinal stresses and for the longitudinal and transverse shear stresses were achieved through the application of the Inverse Rule of Mixtures to the values provided in the data-sheet of each fibre, assuming $\alpha = 1$. However, this methodology poses one inconsistency, as in each data-sheet the matrix is different than the one for our tube. This must be kept in mind, as it could be a reason for some error in the results. Nevertheless, the FVF in both cases was 60%, a value similar to the one which was used in the manufacturing of the tubes where our focus resides, and the cure temperature was 130ºC. The tensile and compressive transverse stresses were taken from the matrix data-sheet for a composite reinforced with Torayca's T300 carbon fibre with a FVF of 64%, an even closer value for this property from our target than the mixture used for the other parameters, with a post-cure of 8h at 140ºC. However, in this data-sheet the hardener used was the HY917, as opposed to HY906. These parameters proved reasonable for the failure predictions, and namely for the prediction of no crushing and of a valid test, as will be discussed further along this thesis, however, in the future, uniaxial tests for the laminate should be developed to provide more accurate results. In this approach, only one mesh was used, whose size was the equal to Mesh A and the element type was S4, to have a more in-depth analysis of the tube's stress state and of the values for the Hashin criteria.

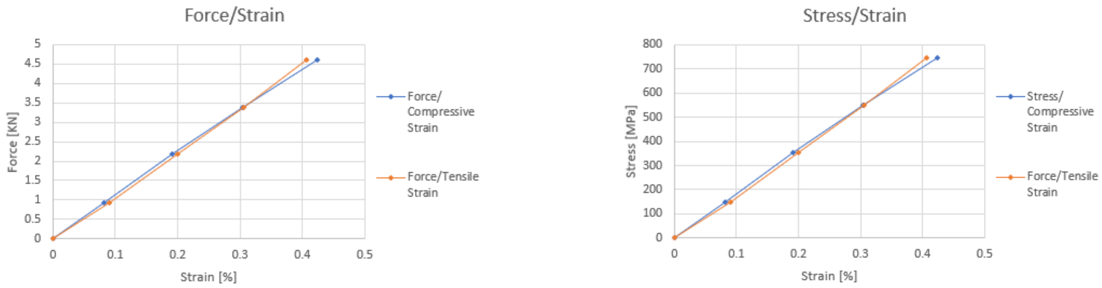

(a) Force/Strain (b) Stress/Tensile Strain

Figure 3.37: Four-Point Bending Simulation Results with Hashin Failure Criterion

Figure 3.37 displays the Force/Strain and Stress/Strain graphics for this approach for both tube's mid-points. The points here portrayed are only the valid ones, this is, the ones in which the values for each parameter for the Hashin criteria are lower than 1.

Through figure 3.37a and the underlying data, the force applied to the tube is expected to be about 4605 N, as at this point the Hashin criterion equation for fibre compression provides a value of 0.96, and for an applied force of 5762 N, the correspondent for the next recorded frame, this parameter far exceeds the unit, reaching 1.6. If we go back to chapter 2, it is clear that rupture occurs when one of the four parameters of these criteria exceeds the unit. It should be mentioned that all the remaining criteria in all relevant nodes are bellow 1, when the applied force is either 4605 N or 5762 N, so the failure is expected to be due to compression in the fibres.

In figure 3.37b, the stress/strain graphic for this simulation is portrayed. The strain of this graphic, as for the one on figure 3.37a was measured along the tube's longitudinal direction in both the upper and lower tube mid-points. The stress has been calculated based on the load applied by both supports, according to equation 3.55. Regarding the elasticity modulus, it can be assessed through figure 3.37b, and is rather similar for both the lower and upper areas of the tube. It is 176 GPa for the point subjected to compressive loading, and 184 GPa for the one subjected to a tensile loading.

$$S = \frac{PL}{2\pi d^2 e} \tag{3.55}$$

Where,

- S is the stress at the outer fibre throughout the load span, in [MPa];
- P is the load at any given point on the load/deflection curve in [N];
- L is the support span in [mm], 260mm for this case;
- d is the outer diameter of the tube in [mm], 16mm for this case;
- e is the tube's thickness in [mm], 1mm for this case;

In figure 3.38, the distribution of the values for the equations of the Hashin criterion for both matrix and fibre compression are displayed, while in figure 3.39, the distribution along the tube of the values for both fibre and matrix tension according to the Hashin criteria are displayed. Both these figures reassure the reader about the most critical nodes for failure. Attention should be given to the scale of these images, as it is not the same for the different images, which can induce the reader in error, moreover, both images (3.38, and 3.39) were taken in the frame immediately before the value of 1 was reached for any equation of the Hashin criteria.

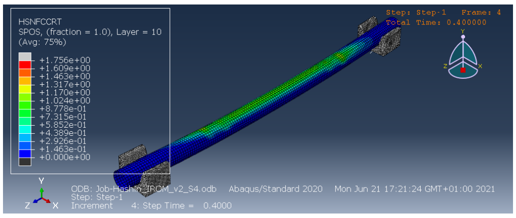

(a) Fibre Compression

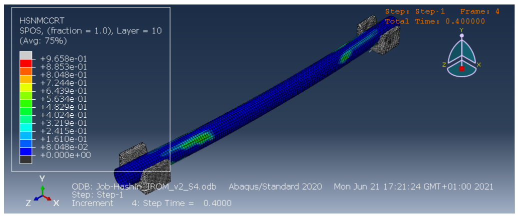

(b) Matrix Compression

Figure 3.38: Hashin criteria for compressive stresses

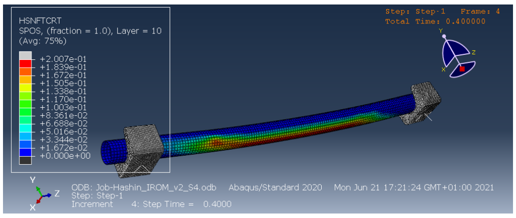

(a) Fibre Tension

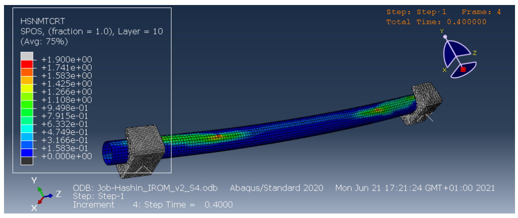

(b) Matrix Tension

Figure 3.39: Hashin criteria for tensile stresses

3.7 Compression Testing

3.7.1 First Approach

Afterwards, a simulation regarding the compressive test was modeled in ABAQUS^{TM}, in order to predict the point where rupture would occur. This simulation and this test procedure were based on ASTM D695-15 [105], although some changes needed to be made to avoid crushing on the tube top-ends.

For this test, an end-fitting must be created so that no crushing occurs in the extremities of the tube, thus, being possible to assess its compressive properties. An image portraying the end-fitting assembled in the tube is shown in figure 3.40. On the section-view of this figure (on the left), it is possible to see both the exterior part of the end-fitting and the cylinder, which is placed inside the tube to provide support, minimizing the crushing probability at the tube's far ends. Both pieces which comprise the end-fitting are glued to the tube.

Establishing the interactions is an important step in this modelling, as a tie must exist between the end-fitting and the tube, to simulate the effect of the glue, and both parts of the end-fitting should also be tied together through a multi-point constraint so that they move alongside each

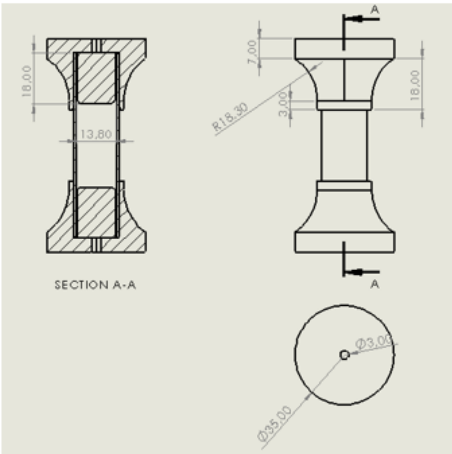

Figure 3.40: Setup used in the compression test modelling

other. Moreover, the friction coefficient was kept the same as the one used in four-point bending simulations (0.3), due to the reasons previously explained.

The boundary conditions applied to one end-fitting consisted of blocking all movement, while on the other, all rotations were also blocked, but regarding displacement, one of 0.5mm was defined in the tube's longitudinal axis, to replicate what would occur in a testing environment, while the displacement in the other directions was blocked. The mesh sizes used are displayed in table 3.7. It should be mentioned although the end-fittings consist of two different parts, they were modelled with the same mesh size and element.

Table 3.7: Mesh size used

Mesh	Tube's Mesh Size	End-fittings' Mesh Size
A	1.5	2
B	2	2

Table 3.8: Mesh element used

Mesh	Tube's Mesh Size	End-fittings' Mesh Size
A	S4R	R3D4
B	S4R	R3D4

Regarding the tube's properties, first the material was defined with the properties specified in figure 3.8, and the failure criterion to be used was the maximum strain criterion for the high modulus fibre, which is 0.8%.

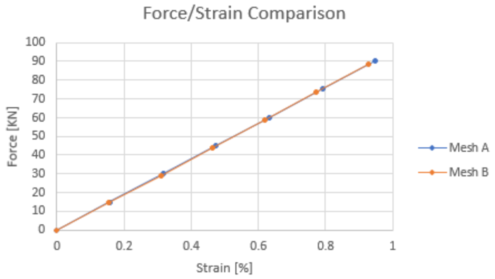

(a) Force/Strain

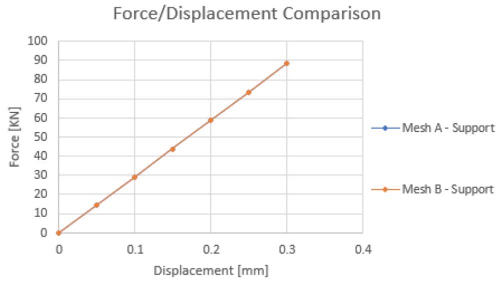

(b) Force/Displacement

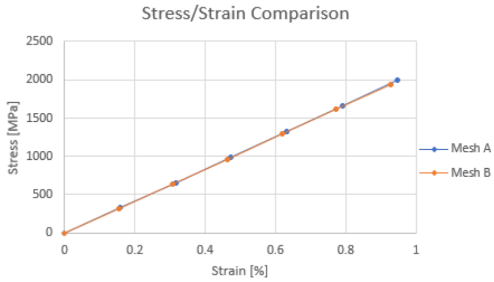

(c) Stress/Strain

Figure 3.41: Comparison between meshes for compression testing

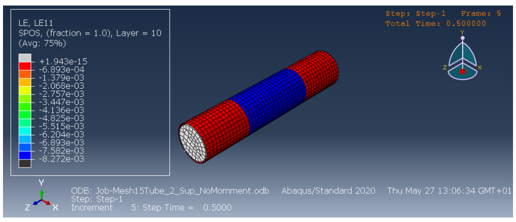

(a) Mesh A

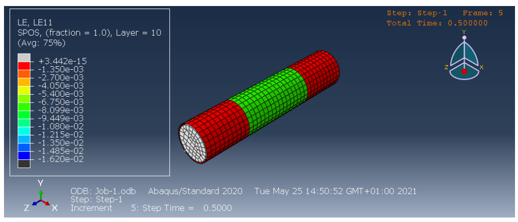

(b) Mesh B

Figure 3.42: Overall strain in the longitudinal direction for the compressive simulation

Through the analysis of figure 3.41, it can be said the mesh size chosen is appropriate due to the convergence between results especially seen in figure 3.41b, where the values for Mesh A cannot be distinguished from those for Mesh B, as they overlap.

Through the analysis of figures 3.41a and 3.42, the underlying data, and through the application of the maximum strain criterion for a strain at break of 0.8%, it is easily estimated the force at which break would occur to be 73.5 kN, and, at that point, the displacement of the end-fitting would be 0.25mm. More importantly, figure 3.42 also provides information about the validity of the proposed end-fittings and confirm no crushing is expected to occur at the interface between those and the tube. It should be noted, these images refer to the frame immediately before the strain of 0.8% is achieved at the central part of the tube (the maximum strain in these figures is 0.79% for Mesh A and 0.78% for Mesh B), but the same strain distribution is verified when a greater displacement is applied, even though that would not be physically possible due to the fibre's limitations.

Figure 3.41c, provides information about the Elasticity Modulus of the tube for a compressive stress, with the layup and materials used, which, for both meshes, is 211 GPa.

3.7.2 Experimental Setup

After this analysis, a more in-depth one was carried out using a more accurate definition of the material properties and using the Hashin criteria as the one which predicts failure, as opposed to the maximum strain criterion, with the parameters displayed in figure 3.36 and on table 3.6. This analysis was done to try to have a more accurate prediction of the load needed to break the specimen, and to further validate the setup, to have a higher degree of confidence the setup would provide valid results. One other difference this analysis posed when compared to the previous was the mesh element used for the tube, S4, as opposed to S4R, for a better and more in-depth analysis of the values experienced at the tube.

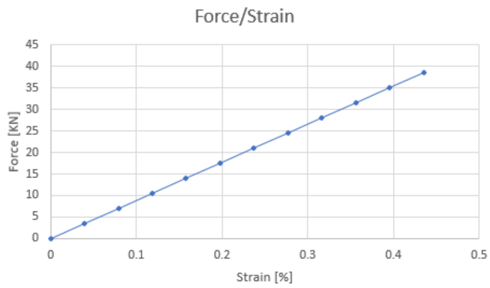

(a) Force/Strain

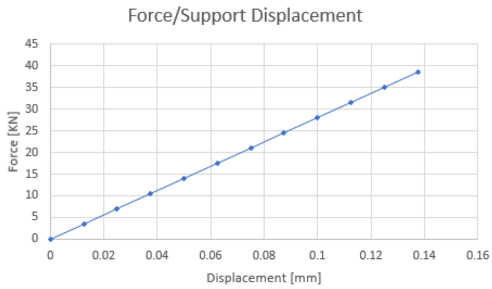

(b) Force/Displacement

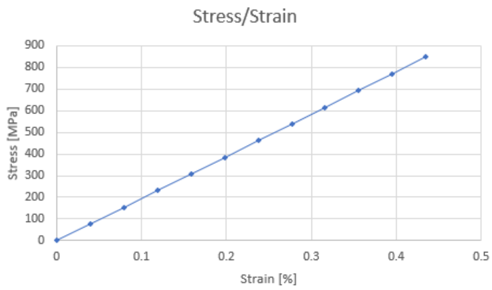

(c) Stress/Strain

Figure 3.43: Results of simulation of compressive test with experimental setup

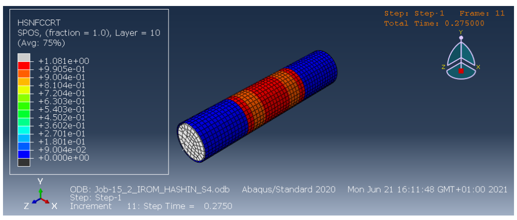

(a) Fibre Compression

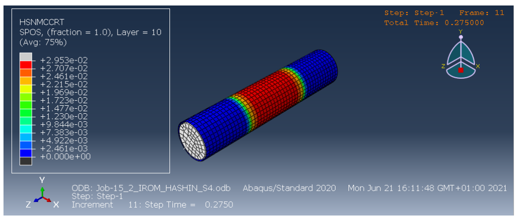

(b) Matrix Compression

Figure 3.44: Results for the Hashin criteria parameters for compression

Through the analysis of 3.43 and the underlying data, the force applied to the tube is expected to be about 39 kN, as at this point the Hashin criterion equation for fibre compression provides a value of 0.998, and for an applied force of 42 kN this parameter far exceeds the unit, reaching 1.18. If we go back to chapter 2, it is clear that rupture occurs when one of the four parameters of these criteria exceeds the unit. It should be mentioned that all the remaining criteria in all relevant nodes are bellow 1, when the applied force is either 39 kN or 42 kN. These results predict the failure would occur due to a compressive rupture in the fibre. Through figure 3.43c, the compressive Young's Modulus can be calculated, which is 195 GPa. It should be mentioned in figure 3.43 the input for these graphics was only for the frames at which every parameter of the Hashin criteria was below 1, this is, only the portion of the simulation with physical meaning was drawn. Figure 3.44 represents the distribution of the compressive parameters of the Hashin criteria for the frame immediately before any parameter (in this case it would be the one for fibre compression) reaches 1.

Moreover, and arguably more important, the simulation predicts failure would occur at the mid-zone of the tube and not due to crushing at the extremities where the end-fitting and the tube establish contact, as for the time frame at which rupture is predicted according to Hashin criterion, all the remaining equations for all the nodes where there is contact between the tube and the end-fitting display a value significantly smaller than 1.

Chapter 4

Experimental Tests

In this section, the experimental tests and their results will be developed, and a comparison with those achieve numerically will be performed. Due to the framing of this project, its inclusion in a corporate project, and the accuracy needed for the project, these were not performed by the student, but rather were performed in a certified test house named APPLUS, in Barcelona. Due to this fact, the student did not have the opportunity of being physically present during testing. However, the fact the tests have been done in a company with several years of experience in the area guarantee a minimization of the handling error which could have been caused by the lack of experience the student has in these situations.

The material from which the tube is made is the one developed on section 3.3, a hybrid fibre with 50/50 % volume between the Torayca T1100G and Torayca M55J, mixed with a FVF of 65% with an epoxy matrix, Araldite LY556/HY907/DY070, with the layup developed in section 3.5.

4.1 Bending Test

The test for assessing the tubes' bending strength has been pursued similarly to the one which has been simulated in subsection 3.6.4. This is, the tube has an external diameter of 16mm and is 1mm thick. Its length is 300mm and rests on two supports, 260mm apart, whose dimensions are on figure 3.34, while being loaded at two loading points, 130mm apart, as is shown in figure 4.1. Both these lengths are centered with the tubes' mid-point. The samples were cut from 14 CFRP tubes, originally 1.8m long, each. All test specimen were labelled with a reference which allows the identification of the respective batch number, tube number and the position in length from which they were cut from the original CFRP tube.

An universal testing machine that incorporates a load indicator and controls the crosshead speed has been used to perform the test. This speed, which is the speed of the punch, has been set to 0.5mm/min. The supports have been manufactured in steel and due to the dimensional characteristics of the test specimen, its high flexural rigidity, and to avoid uneven load distribution

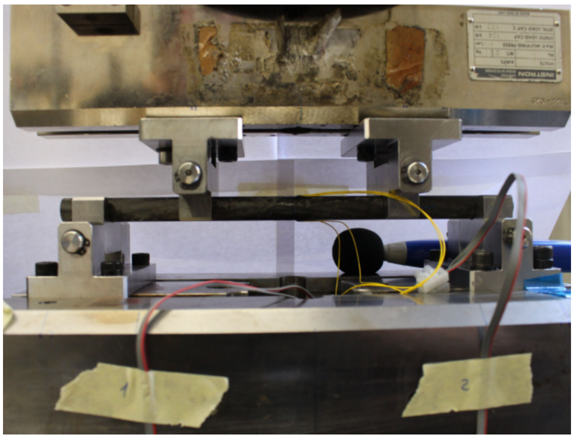

Figure 4.1: Bending test setup

at the four load points, a rotation degree of freedom (perpendicular to the sample axis and centered with the crosshead axis) is allowed to the loading accessory. A 5 kN load cell calibrated according to ISO 7500 and ASTM E4 was used with a pre-load of 25 N at the beginning of each test. The data acquisition rate was 50 Hz.

As already seen, the failure could be a tensile one, which would occur at the bottom of the tube, or a compressive one, developed at the upper part of the tube. Owing to this, both load solicitations were analysed, this is, the strain was measured both at the top and at the bottom of the tube along the longitudinal direction. As already explained, for the tests to be deemed valid, rupture must occur between the upper supports.

According to the standard, and as has already been stated, the flexural strength is defined as the maximum stress at the outer fibres at the moment of break independently of the failure being a compressive or a tensile one, and is calculated according to equation 4.1.

$$S = \frac{PL}{2\pi d^2 e} \tag{4.1}$$

Where,

- S is the stress at the outer fibre throughout the load span in [MPa];
- P is the load at a given point on the load/deflection curve in [N];
- L is the support span in [mm], 260mm in this case;
- d is the outer diameter of the tube in [mm], 16mm in this case;
- e is the tubes' thickness in [mm], 1mm in this case.

The equation 4.1 is developed from the classic bending equation.

For the stiffness calculation, strain gauges were used, as an analysis through the deflection is not adequate for a specimen with such high flexural rigidity. The points recorded for this calculation for each specimen were the ones immediately before the strain of 0.00025 [m/m] (0.025%)

and 0.00200 [m/m] (0.2%) were reached for both tensile and compressive loading. These values were chosen due to them being on the initial part of the graphic, but after the initial oscillations the graphic portrays both due to the adjustments between the support and the tube and due to the pre-load.

After performing the previous calculations for the samples which originated valid tests, the results on table 4.1 are achieved. In figure 4.2, the stress/strain graphics are displayed for both the upper part of the tube, subjected to compression (4.2a), and for the bottom one, subjected to a tensile loading (4.2b).

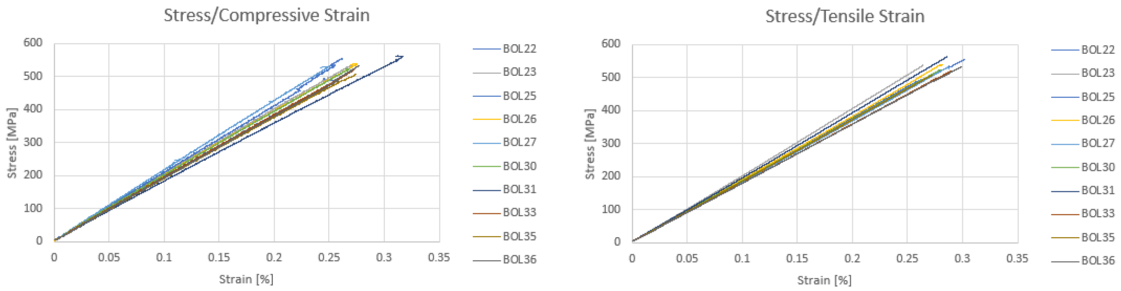

(a) Stress/Strain for the area in compression (b) Stress/Strain for the area in tension

Figure 4.2: Stress/Strain relations for all tested specimen

Table 4.1: Four-Point Bending Test Results

Sample	**Bending Strength [MPa]**	**Compressive Bending Modulus [GPa]**	**Tensile Bending Modulus [GPa]**	**Bending Modulus (Mean) [GPa]**
BOL22	494	189	189	189
BOL23	538	199	198	199
BOL25	555	204	204	204
BOL26	540	196	196	196
BOL27	532	211	213	212
BOL30	525	195	195	195
BOL31	563	177	177	177
BOL33	521	191	190	190
BOL35	509	186	187	187
BOL36	533	188	189	189
Maximum	563	211	213	212
Minimum	494	177	177	177
Mean	531	194	194	194
Standard Deviation	20	9	9	9

Figure 4.3 shows the rupture of the specimen BOL29 for the bending test. Here we can assess what has been said about the failure being between the upper supports, so the test can be valid, and in this case the failure was a compressive one.

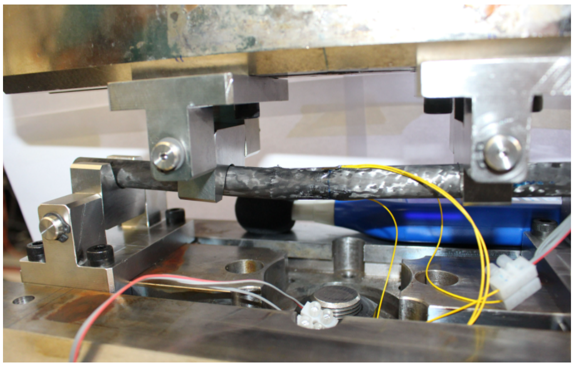

Figure 4.3: Rupture of BOL29 for Bending Tests

Furthermore, a comparison between the experimental and the simulation results for the last simulation done, the one which more accurately represents the test, should be done to assess its validity. This comparison is on figure 4.4 and it is clear the bending modulus for both the tested tubes and the numerically simulated ones is rather similar, as a difference of less than 10% has been found. That being said, regarding the ultimate stress, the differences are much greater. The differences mentioned can also be seen on table 4.2 and may be due to the approximations done to define the parameters for the Hashin criteria, the fact the curing temperature and time for which these properties were studied in the data-sheets are different from those of the manufactured tube, or the different matrix or fibre used in the data-sheets, accordingly.

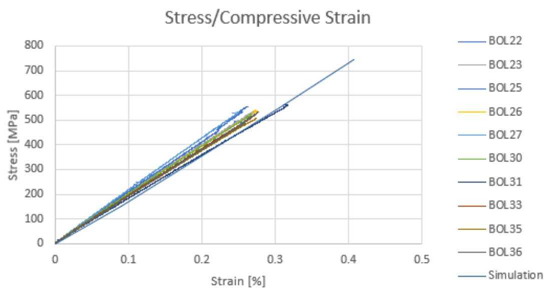

(a) Stress/Strain for the area in compression

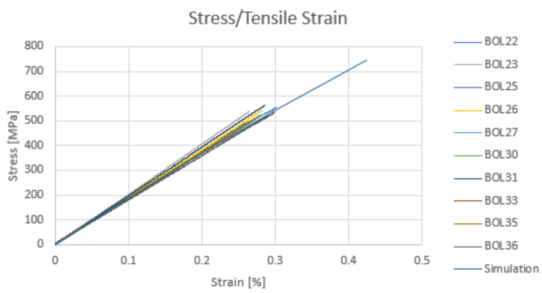

(b) Stress/Strain for the area in tension

Figure 4.4: Stress/Strain relation for bending testing for both experimental tests and simulation results

4.2 Compression Testing

The purpose of this test was assessing the tube's compressive strength, for that, a setup similar to the one presented in section 3.7 was used, with the only difference being the tube's length, here

Table 4.2: Simulation and Experimental Results Comparison for Bending Testing

	Tensile Bending Modulus [GPa]	**Compressive Bending Modulus [GPa]**	**Bending Strength [MPa]**
Experimental Results	194	194	531
Numerical Results	184	176	744
Error	5.1%	9.2%	40.1%

65.4mm, as is shown in figure 4.5, as opposed to 70mm on the simulation. Both parts of the end-fitting used were manufactured in aluminium and were used to guarantee no crushing would occur at the tube top ends. The load was applied through a controlled movement of the upper plate at a crosshead speed of 0.5mm/min, while the lower plate was fixed. This setup aimed to achieve an uniform load distribution at the specimen end-fitting and also ensuring the specimen is axially aligned with the machine axis, crucial in compressive tests to avoid buckling. The machine used had a load cell of 50 kN calibrated according to ISO 7500 and ASTM E4, and used a pre-load of 100N. The data-acquisition rate was the same as the one used for the bending test, 50Hz.

Regarding the specimen, these were cut from 14 tubes, distributed between 7 batches and were cut from different positions along each tube to ensure the validity of the results. Their specimen number identifies these parameters, so as to understand the results if some of them fall outside the range observed on the remaining ones.

This test's purpose is to define the tube's compressive strength, so only the load application mentioned was needed however, for further characterization of the tube, some specimen were equipped with two strain gauges to allow the calculation of the compressive modulus. Both strain gauges were oriented along the specimen's longitudinal direction and on opposite sides of the tube.

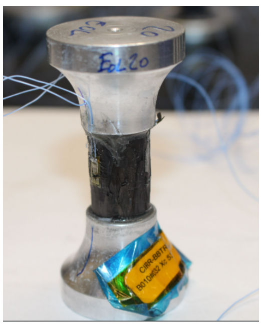

(a) With strain gauges

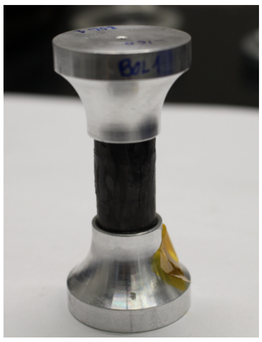

(b) Without strain gauges

Figure 4.5: Compression test specimen

In this test only a compressive failure is admissible and attention should be given so as to not have a buckling failure, which is the main reason for having such short specimen. As an end-fitting was needed to improve the load transfer between the machine and the tube, the compressive failure must also be outside the contact area between the tube and the end-fitting.

Before starting each test, both the internal and external diameters of the tube were measured to allow for the calculation of the area, which would be used to calculate the stress experienced by the tube, according to equation 4.2.

$$\sigma = \frac{P}{A} \tag{4.2}$$

With,

$$A = \pi \left[\left(\frac{d_{ext}}{2} \right)^2 - \left(\frac{d_{int}}{2} \right)^2 \right] \tag{4.3}$$

For the specimen equipped with strain gauges, a stress/strain graphic was compiled where the stress was the one calculated according to equation 4.2 for each frame, and the strain was the average of the one measured by each strain gauge for each frame, resulting in the graphic on figure 4.6b.

The compressive modulus is calculated similarly to the bending one, this is, the ratio between the difference of the stress in two points and their respective strain. For the calculation of this parameter, the same procedure as the one used for the bending modulus was followed, this is, using the points where the strain was immediately lower than 0.00025 [m/m] (0.025%) and 0.002 [m/m] (0.2%), and the corresponding stresses. These were the chosen values due to them being on the first straight portion of the stress/strain curve but would allow to disregard the initial variation that arises from the pre-load application, and the adjustment between the specimen and the tube. For an ideal calculation of this parameter, a longer specimen should be used, however, as the most important property to be measured was the strength, a shorter specimen needed to be used in order to avoid buckling. The results are on table 4.3.

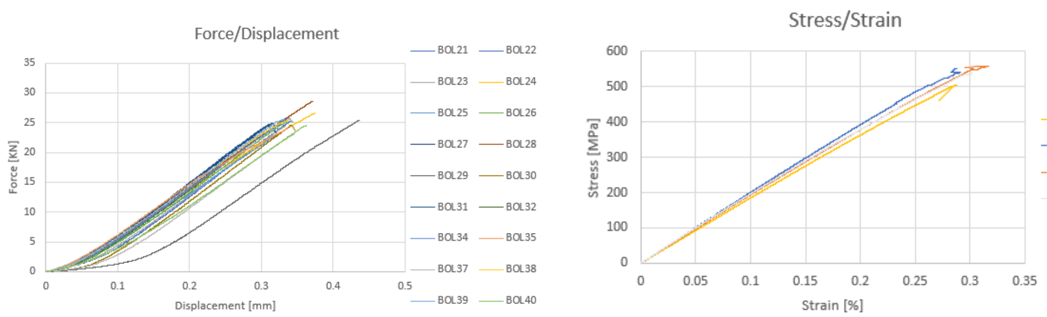

(a) Force/Displacement

(b) Stress/Strain

Figure 4.6: Compressive test results

While analysing the results, the validity of the tests is clear, not only due to the place where rupture occurred, but also due to the similarities portrayed between the several curves in figures 4.6a and 4.6b. The only curve in the force/displacement graphic that presents some discrepancy regarding the remaining ones, albeit not too great, is the one for specimen BOL29, which presents a similar value for the force and stress at break when compared to the other specimen, but the displacement for each load value is greater. However, in the first portion of the graphic, it can be

Table 4.3: Compression Test Results

Sample	**Compressive Strength [MPa]**	**Compressive Modulus [GPa]**	**Internal Diameter [mm]**	**External Diameter [mm]**
BOL21	568	-	14.04	15.98
BOL22	559	-	14.04	15.96
BOL23	532	-	14.04	15.99
BOL24	588	-	14.05	15.97
BOL25	517	-	14.05	15.97
BOL26	567	-	14.05	15.97
BOL27	544	-	14.04	15.99
BOL28	631	-	14.04	15.97
BOL29	554	-	14.04	15.99
BOL30	538	-	14.04	15.98
BOL31	543	-	14.05	15.99
BOL32	545	-	14.05	15.97
BOL34	568	-	14.05	15.99
BOL35	587	-	14.05	16.00
BOL37	508	181	14.04	15.97
BOL38	554	196	14.03	15.99
BOL39	560	188	14.05	15.99
BOL40	540	188	14.05	15.98
Maximum	631	196	14.05	16.00
Minimum	508	181	14.03	15.96
Mean	556	188	14.04	15.98
Standard Deviation	27	5	0.006	0.01

seen the load value barely changes, while the displacement increases significantly. This may be due to a longer movement by the loading cell before compressing the specimen, an error while calibrating the zero of the machine, or a deformation of the adhesive that holds the end-fitting and the tube together. Another similarity this curve shows with the others, is after the first initial portion of the graphic, the slope of the curve is similar to the remaining specimen.

While interpreting these results, the reader must be wary the end-fitting was made from aluminium, a material which cannot be assumed rigid, so the deformation this accessory experiences during loading may have an impact in the graphics as the force and displacement have been measured at the machine, and the stress has been mathematically calculated from the load, while the strain was measured at the tube.

Furthermore, an analysis comparing the results of both the experimental tests and the numerical simulation ones should be done. This comparison is on figure 4.7 and on table 4.4. In figure 4.7, it is clear the compressive Young's Modulus for both the experimental results and the numerical simulations results is extremely similar, as its difference is less than 4%. That being said, the compressive strength achieved from the experimental tests is significantly different from that achieved by the numerical simulation. This may be due to the approximations done while defining the parameters for the Hashin criteria, the fact the curing temperature and time for which these properties were defined in the data-sheets are different from those of the manufactured tubes, or the different matrix or fibre used in the data-sheets, accordingly.

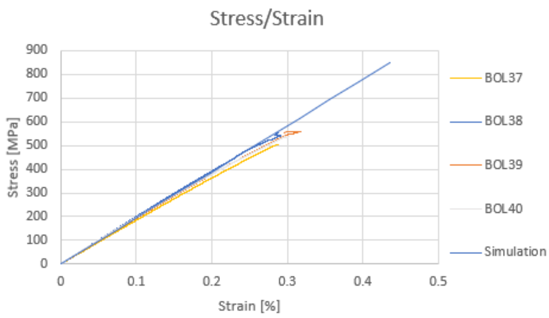

Figure 4.7: Stress/Strain relation for compressive testing for both experimental tests and simulation results

Table 4.4: Simulation and Experimental Results Comparison for Compressive Testing

	Compressive Modulus [GPa]	**Compressive Strength [MPa]**
Experimental Results	188	556
Numerical Results	195	847
Error	3.7%	52.3%

Chapter 5

Conclusions and Future Work

The main objective of this work was to mechanically characterize the CFRP tube, namely in bending and compression, and develop the necessary changes to the standards that already exist to accomplish a successful testing campaign. To reach this objective, some accessories needed to be designed to ensure a correct load transfer between the loading cell and the tube. Assessing the validity of these accessories and changes through a numerical simulation was also a point which turned out to be of great importance from the early stages of this work, due to the existing constraints for testing, namely cost, whether manufacturing the tubes or actually testing the specimen, and the fact the test house was not near the company's facilities.

5.1 Numerical Simulation

From the numerical models, several conclusions of great importance were achieved, first the attention that should be given to the crushing effect, which played a major role in the test with the loading noses as are in the standard. Afterwards, especially with the third approach and with the one designated "Experimental Setup", it was realized that a support with significant contact area with the tube and with a shape that was tailored to the specimen is of great importance and would allow to reduce crushing. This conclusion was of the utmost importance to create a valid setup.

That being said, this process posed one severe limitation, the fact the exact elastic properties of the lamina were unknown, which culminated in the need of defining these values through approximation models, as the ones exposed in section 3.1, a process which could have culminated in a bad approximation of the tube's mechanical properties and not provide accurate results. Despite this fact, the values proved accurate when compared to the experimental ones, so the results for this tube's elastic properties can be looked at with a significant degree of confidence. Having said this, tests should be done for a unidirectional laminate to characterize the different ultimate stresses needed for the definition of the Hashin criteria, as the difference for these properties between the experimental and numerical results cannot be neglected.

The approach taken with the various numerical simulations also allowed to further confirm what has been stated about the accuracy of the maximum strain criterion. This is, the maximum allowable strain for the high modulus fibre was 0.8% and this parameter for both the high stress fibre and the matrix was significantly higher. However, if we assess both the experimental stress/strain curves and the numerical ones in which the Hashin criteria was used, the strain at break is significantly lower than 0.8%, about 0.4% in the numerical models and 0.3% on the experimental tests. That being said, this criterion has been useful to estimate crushing and to design a valid setup.

5.2 Experimental Results

Concerning the accessories designed to ensure the validity of the tests and a correct load transfer between the loading cell and the tube, these proved useful as the tests performed were valid. This means, the rupture was given on the desired area for each test, rather than by crushing in the load application points. With this in mind, we can state the accessories proposed were successful in their implementation and these generic shapes are suitable to be used for uniaxial compressive and bending tests for tubular specimen.

Regarding the experimental campaign, it can also be considered a successful one as the results present a great degree of similarity between each other, proved by the small standard deviation, which suggests the validity of the campaign. When it comes to the manufacturing quality, it seems to be validated through these results, however, this statement cannot be made adamantly. For this to be the case, more tests should be made. These tests culminated in a bending strength of 531 MPa and a bending modulus of 194 GPa, for either the zone subjected to compression or to a tensile load, and an uniaxial compressive strength of 556 MPa with a compressive modulus of 188 GPa.

That being said, regarding the actual results achieved, a careful analysis should be done as on a first approach these may not look too promising when compared to the values advertised in each of the data-sheets, as is represented in table 5.1. However, the values in each data-sheet are for unidirectional laminates, which was not the case for the tube here considered due to other required properties. Naturally, if no other requirement rather than strength and stiffness in the longitudinal direction existed, the layup could have been different, which would result in different values for the measured properties. Moreover, the resin's service temperature range also needed to be great due to the different conditions the product would be subjected to while in service.

Table 5.1: Comparison between experimental results and value in the data-sheets

	Bending Strength [MPa]	**Bending Modulus [GPa]**	**Compressive Strength [MPa]**	**Compressive Modulus [GPa]**
T100G	1920	159	1870	-
M55J	1180	274	890	-
Results	531	194	556	188

5.3 Further Work

For a more accurate characterization of the tube's behaviour in service, a bending creep test and a compressive creep test are suggested, as the loads the tube will be subjected to in service are expected to remain during a long period of time, as opposed to the single loading which is experienced in these tests, thus an analysis of the tube's behaviour with time should be done to further validate their structural integrity.

Furthermore, and for a more extensive mechanical characterization of the tube, other tests should be done, namely a torsion test, to assess the tube's strength and resistance to torsion, and a tensile test to evaluate both its tensile strength, as well as its tensile modulus. These tests were not performed as they were outside of this project's scope, due to the application this tube has been designed for. However, these properties are important to establish a full characterization of the tube, which may be important for other applications. Moreover, the testing of these properties can also be used as a process to control the quality of the manufactured tubes, for the case of mass production.

Moreover, a fracture mechanics approach could have been undertaken, with tests regarding the crack propagation according to either Mode I or Mode II. That being said, as has been said on chapter 2, no standard exist for this approach for filament wound tubes, so the development of these methodologies also needs to be done. Hence, after the definition of the testing methodologies, it may also be a suitable approach to assess the manufacturing quality of the tubes, or for implementation in quality control processes for mass production.

On the other side, the simulation can also be further developed to have a more accurate forecast of the elastic and failure properties. For this to be the case, tests for a unidirectional lamina should be conducted. These tests should evaluate the elastic properties to corroborate those achieved through mathematical models, despite the similarities achieved for both the bending and the compressive moduli, but should also evaluate the failure strengths needed for the Hashin criteria (the ultimate longitudinal and transverse tensile stresses, the ultimate longitudinal and transverse compressive stresses and the ultimate longitudinal and transverse shear stresses). One other approach to enhance the accuracy of the simulation results which could be valuable is to use the LaRC 05 failure criteria, instead of the Hashin one, as described in section 3.2.2.3. However, this model may only be meaningful for complex loading of more complex parts, due to its increased complexity and required detailing of the lamina's properties. Naturally, for this model to be applied, tests must be done to define each of the parameters needed.

Besides this, an inverse methodology for parameter identification program to be incorporated in the ABAQUS^{TM} simulations already created could be built to have simulations which more accurately replicated the testing results. This software would arbitrate initial values for each material property, for example the ones used in these simulations, and would assess the difference found between numerical and experimental results. It would then repeat this procedure in an iterative way until values coincident with those achieved experimentally are achieved.

References

[1] European Union. Copernicus programme. Available at https://www.copernicus.eu/en/about-copernicus, Accessed last time in February 2021, 2021.

[2] HPS GmbH The team to trust. Lea - large european antenna (status report 09/2019). Available at https://www.youtube.com/watch?v=8DF9V2JDSsg, Accessed last time in July 2021, 2020.

[3] Harry Jones. The recent large reduction in space launch cost. 48th International Conference on Environmental Systems, 2018.

[4] Chiara Colombo and Laura Vergani. Optimization of filament winding parameters for the design of a composite pipe. *Composites Part B: Engineering*, 148:207–216, 2018.

[5] Louis A Pilato and Michael J Michno. *Advanced composite materials*. Springer Science & Business Media, 1994.

[6] Stephen J Pickering. Recycling technologies for thermoset composite materials—current status. *Composites Part A: applied science and manufacturing*, 37(8):1206–1215, 2006.

[7] Yu Jiangtao, Wang Yichao, Hu Kexu, Yu Kequan, and Xiao Jianzhuang. The performance of near-surface mounted cfrp strengthened rc beam in fire. *Fire Safety Journal*, 90:86–94, 2017.

[8] Milad Bazli and Milad Abolfazli. Mechanical properties of fibre reinforced polymers under elevated temperatures: An overview. *Polymers*, 12(11):2600, 2020.

[9] Friederike Fleischhaker, Alexander P Haehnel, Andrea M Misske, Mathieu Blanchot, Sylke Haremza, and Christopher Barner-Kowollik. Glass-transition-, melting-, and decomposition temperatures of tailored polyacrylates and polymethacrylates: General trends and structure–property relationships. *Macromolecular Chemistry and Physics*, 215(12):1192–1200, 2014.

[10] Castro Composites. Resoltech 1080s. Available at https://www.castrocompositesshop.com/img/cms/Resoltech1080S_1.pdf, Accessed last time in March 2021.

[11] Resoltech. Resoltech 1080s. Available at https://www.resoltech.com/en/markets/1000-detail.html, Accessed last time in March 2021.

[12] Resoltech. Resoltech htg160. Available at https://www.resoltech.com/en/markets/htg160-detail.html, Accessed last time in March 2021.

[13] Sabic. Cycoloy fr resin cs9610. Available at https://www.sabic.com/en/products/specialties/cycoloy-resins/cycoloy-fr-resin, Accessed last time in March 2021.

[14] Sabic. Extrem resin vh1003. Available at https://www.sabic.com/en/products/specialties/extem-resins/extem-resin, Accessed last time in March 2021.

[15] Huntsman. Advanced materials: Araldite ly 556/aradur 906/accelerator dy 070. Available at https://samaro.fr/pdf/FT/Araldite_FT_LY_556_Aradur_906_Accelerator_DY070_EN.pdf, Accessed last time in March 2021.

[16] Mathieu Robert and Brahim Benmokrane. Behavior of gfrp reinforcing bars subjected to extreme temperatures. *Journal of Composites for Construction*, 14(4):353–360, 2010.

[17] Gurit. Gurit guide to composites. Gurit. Available at https://www.gurit.com/-/media/Gurit/Datasheets/guide-to-composites.pdf, accessed last time in February 2021.

[18] Simona Naseva, Vineta Srebrenkoska, Svetlana Risteska, Maja Stefanoska, and Sara Srebrenkoska. Mechanical properties of filament wound pipes: effects of winding angles. *Quality of Life*, 6(1-2):10–15, 2015.

[19] Gerson Marinucci, Eduardo da S Leitão, and Osni de Carvalho. Mechanical characterization of carbon fibre composites with the reinforcement at different orientation.

[20] A.M. Datta and B.P. Hatua. Influence of winding angle on the physical properties of filament wound composite pipe. *Proceedings of the 3rd National conference on Emerging Trends in Textile, Fibre and Apparel Engineering*, 2016.

[21] Mahoor Mehdikhani, Larissa Gorbatikh, Ignaas Verpoest, and Stepan V Lomov. Voids in fiber-reinforced polymer composites: A review on their formation, characteristics, and effects on mechanical performance. *Journal of Composite Materials*, 53(12):1579–1669, 2019.

[22] Hansong Huang and Ramesh Talreja. Effects of void geometry on elastic properties of unidirectional fiber reinforced composites. *Composites Science and Technology*, 65(13):1964–1981, 2005.

[23] Mahoor Mehdikhani, Ilya Straumit, Larissa Gorbatikh, and Stepan V Lomov. Detailed characterization of voids in multidirectional carbon fiber/epoxy composite laminates using x-ray micro-computed tomography. *Composites Part A: Applied Science and Manufacturing*, 125:105532, 2019.

[24] Nathan K Fritz, Reed Kopp, Abigail K Nason, Xinchen Ni, Jeonyoon Lee, Itai Y Stein, Estelle Kalfon-Cohen, Ian Sinclair, S Mark Spearing, Pedro P Camanho, et al. New interlaminar features and void distributions in advanced aerospace-grade composites revealed via automated algorithms using micro-computed tomography. *Composites Science and Technology*, 193:108132, 2020.

[25] Linqi Zhuang. Effects of voids on delamination growth in composite laminates under compression. Master's thesis, 2012.

[26] Pınar Karpuz. Mechanical characterization of filament wound composite tubes by internal pressure testing. Master's thesis, 2005.

[27] L Carrino, W Polini, and L Sorrentino. Influence of winding speed on winding tension in robotized filament winding of complex-shape parts. *Composites Science and Technology*, 65(10):1574–1581, 2005.

[28] W Polini and L Sorrentino. Influence of winding speed and winding trajectory on tension in robotized filament winding of full section parts. *Composites science and technology*, 65(10):1574–1581, 2005.

[29] Jose Humberto S Almeida Jr, Marcelo L Ribeiro, Volnei Tita, and Sandro C Amico. Damage and failure in carbon/epoxy filament wound composite tubes under external pressure: Experimental and numerical approaches. *Materials & Design*, 96:431–438, 2016.

[30] P Carrara and L De Lorenzis. A coupled damage-plasticity model for the cyclic behavior of shear-loaded interfaces. *Journal of the Mechanics and Physics of Solids*, 85:33–53, 2015.

[31] G Perillo and AT Echtermeyer. Mode i fracture toughness testing of composite pipes. *Applied Composite Materials*, 20(6):1135–1146, 2013.

[32] Fernando José Moura Martins de Brito. *Caracterização do comportamento dos plásticos reforçados com vista a aplicações estruturais*. PhD thesis, LNEC, 1985.

[33] Mark McElroy, Wade Jackson, Robin Olsson, Peter Hellström, Spyros Tsampas, and Mark Pankow. Interaction of delaminations and matrix cracks in a cfrp plate, part i: A test method for model validation. *Composites Part A: Applied Science and Manufacturing*, 103:314–326, 2017.

[34] Chiara Colombo and Laura Vergani. Influence of delamination on fatigue properties of a fibreglass composite. *Composite Structures*, 107:325–333, 2014.

[35] P Maimi, H Rodríguez, N Blanco, and JA Mayugo. Numerical modeling of matrix cracking and intralaminar failure in advanced composite materials. In *Numerical Modelling of Failure in Advanced Composite Materials*, pages 175–192. Elsevier, 2015.

[36] Andrejs Pupurs. Fiber failure and debonding in composite materials. In *Modeling Damage, Fatigue and Failure of Composite Materials*, pages 173–196. Elsevier, 2016.

[37] Serge Abrate. Matrix cracking in laminated composites: a review. *Composites engineering*, 1(6):337–353, 1991.

[38] Syafiqah Nur Azrie Bt Safri, MTH Sultan, and Mohammad Jawaid. Damage analysis of glass fiber reinforced composites. In *Durability and Life Prediction in Biocomposites, Fibre-Reinforced Composites and Hybrid Composites*, pages 133–147. Elsevier, 2019.

[39] Linda Sawyer, David T Grubb, and Gregory F Meyers. *Polymer microscopy*. Springer Science & Business Media, 2008.

[40] A Krishnamoorthy, J Lilly Mercy, KSM Vineeth, and Manoj Kumar Salugu. Delamination analysis of carbon fiber reinforced plastic (cfrp) composite plates by thermo graphic technique. *Materials Today: Proceedings*, 2(4-5):3132–3139, 2015.

[41] MR Wisnom. The role of delamination in failure of fibre-reinforced composites. *Philosophical Transactions of the Royal Society A: Mathematical, Physical and Engineering Sciences*, 370(1965):1850–1870, 2012.

[42] Wilfried V Liebig, Christian Leopold, Thomas Hobbiebrunken, and Bodo Fiedler. New test approach to determine the transverse tensile strength of cfrp with regard to the size effect. *Composites Communications*, 1:54–59, 2016.

[43] Adrian P. Mouritz. *Introduction to Aerospace Materials*. Woodhead Publishing, first edition, 2012.

[44] Daniel Adams. Notched testing of composites. Available at https://www.compositesworld.com/articles/notched-testing-of-composites, Accessed last time in February 2021, 2016.

[45] C Barile and C Casavola. Mechanical characterization of carbon fiber-reinforced plastic specimens for aerospace applications. In *Mechanical and physical testing of biocomposites, fibre-reinforced composites and hybrid composites*, pages 387–407. Elsevier, 2019.

[46] Dominick V Rosato. *Plastics engineered product design*. Elsevier, 2003.

[47] Myer Kutz. *Mechanical engineers' handbook, volume 1: Materials and engineering mechanics*. John Wiley & Sons, 2015.

[48] E Alfredo Campo. *Selection of polymeric materials: how to select design properties from different standards*. William Andrew, 2008.

[49] Robert J Asaro, Brian Lattimer, and William Ramroth. Structural response of frp composites during fire. *Composite Structures*, 87(4):382–393, 2009.

[50] Tanguy Messager. Buckling of imperfect laminated cylinders under hydrostatic pressure. *Composite structures*, 53(3):301–307, 2001.

[51] Chul-Jin Moon, In-Hoon Kim, Bae-Hyeon Choi, Jin-Hwe Kweon, and Jin-Ho Choi. Buckling of filament-wound composite cylinders subjected to hydrostatic pressure for underwater vehicle applications. *Composite Structures*, 92(9):2241–2251, 2010.

[52] Yu Bai and Thomas Keller. Delamination and kink-band failure of pultruded gfrp laminates under elevated temperatures and compression. *Composite structures*, 93(2):843–849, 2011.

[53] Milad Bazli, Hamed Ashrafi, Armin Jafari, Xiao-Ling Zhao, Hamed Gholipour, and Asghar Vatani Oskouei. Effect of thickness and reinforcement configuration on flexural and impact behaviour of gfrp laminates after exposure to elevated temperatures. *Composites Part B: Engineering*, 157:76–99, 2019.

[54] Daniel Adams. Shear testing of high-shear strength composite laminates. Available at https://www.compositesworld.com/articles/shear-testing-of-high-shear-strength-composite-laminates, Accessed last time in February 2021, 2018.

[55] Mohammad Shekarchi, Emadoddin Majdabadi Farahani, Mohammad Yekrangnia, and Togay Ozbakkaloglu. Mechanical strength of cfrp and gfrp composites filled with app fire retardant powder exposed to elevated temperature. *Fire Safety Journal*, 115:103178, 2020.

[56] Jinlian Hu. *3-D fibrous assemblies: properties, applications and modelling of three-dimensional textile structures*. Elsevier, 2008.

[57] Ammar N Hanoon, Ali A Abdulhameed, Haider A Abdulhameed, and Saad K Mohaisen. Energy absorption evaluation of cfrp-strengthened two-spans reinforced concrete beams under pure torsion. *Civil Engineering Journal*, 5(9):2007–2018, 2019.

[58] Amir Hamzeh Keykha. Structural performance evaluation of deficient steel members strengthened using cfrp under combined tensile, torsional and lateral loading. *Journal of Building Engineering*, 24:100746, 2019.

[59] Yu-Hang Wang, Yu-Yan Wang, Xu-Hong Zhou, Ran Deng, Yong-Sen Lan, Wei Luo, Peng Li, Qing-Shan Yang, and Ke Ke. Coupled ultimate capacity of cfrp confined concrete-filled steel tube columns under compression-bending-torsion load. 31:558–575, 2021.

[60] Saravanan Panchacharam and Abdeldjelil Belarbi. Torsional behavior of reinforced concrete beams strengthened with frp composites. 1:01–110, 2002.

[61] J Loughlan. The buckling of cfrp composite plates in compression and shear and thin-walled composite tubes in torsion–the effects of bend-twist coupling and the applied shear direction on buckling performance. *Thin-Walled Structures*, 138:392–403, 2019.

[62] Rodrigo Gonçalves and Dinar Camotim. Buckling behaviour of thin-walled regular polygonal tubes subjected to bending or torsion. *Thin-Walled Structures*, 73:185–197, 2013.

[63] Daniel Adams. Glass transition temperature testing of composites. Available at https://www.compositesworld.com/articles/glass-transition-temperature-testing-of-composites, Accessed last time in March 2021, 2018.

[64] Leif A Carlsson, Donald F Adams, and R Byron Pipes. *Experimental characterization of advanced composite materials*. CRC press, 2014.

[65] John Eric Little, Xiaowen Yuan, and Mark Ian Jones. Characterisation of voids in fibre reinforced composite materials. *NDT & E International*, 46:122–127, 2012.

[66] David K Hsu and Kevin M Uhl. A morphological study of porosity defects in graphite-epoxy composites. pages 1175–1184, 1987.

[67] J Rousseau, D Perreux, and N Verdiere. The influence of winding patterns on the damage behaviour of filament-wound pipes. *Composites Science and Technology*, 59(9):1439–1449, 1999.

[68] DEW Stone and B Clarke. Ultrasonic attenuation as a measure of void content in carbon-fibre reinforced plastics. *Non-destructive testing*, 8(3):137–145, 1975.

[69] W N Reynolds and SJ Wilkinson. The analysis of fibre-reinforced porous composite materials by the measurement of ultrasonic wave velocities. *Ultrasonics*, 16(4):159–163, 1978.

[70] Oleg D Sherby and Peter M Burke. Mechanical behavior of crystalline solids at elevated temperature. *Progress in materials science*, 13:323–390, 1968.

[71] Laboratory Testing Inc. Stress rupture and creep testing. Laboratory Testing Inc.. Available at https://www.labtesting.com/services/materials-testing/mechanical-testing/stress-rupture/, accessed last time in May 2021.

[72] Lucideon. Creep and rupture testing. Lucideon. Available at https://www.lucideon.com/testing-characterization/creep-and-rupture-testing, accessed last time in May 2021.

[73] Leif Jilkén, Göran Mälhammar, and Ragnar Seldén. The effect of mineral fillers on impact and tensile properties of polypropylene. *Polymer Testing*, 10(5):329–344, 1991.

[74] Daniel Adams. Can flexure testing provide estimates of composite strength properties? Available at https://www.compositesworld.com/articles/can-flexure-testing-provide-estimates-of-composite-strength-properties, Accessed last time in March 2021, 2017.

[75] F Ozdil and LA Carlsson. Characterization of mode i delamination growth in glass/epoxy composite cylinders. *Journal of composite materials*, 34(5):398–419, 2000.

[76] P Davies and F Rannou. The effect of defects in tubes: Part 1. mode i delamination resistance. *Applied composite materials*, 1(5):333–349, 1994.

[77] B Lauke and K Friedrich. Evaluation of processing parameters of thermoplastic composites fabricated by filament winding. *Composites Manufacturing*, 4(2):93–101, 1993.

[78] James P Lucas. Delamination fracture: effect of fiber orientation on fracture of a continuous fiber composite laminate. *Engineering fracture mechanics*, 42(3):543–561, 1992.

[79] A Laksimi, ML Benzeggagh, G Jing, M Hecini, and JM Roelandt. Mode i interlaminar fracture of symmetrical cross-ply composites. *Composites science and technology*, 41(2):147–164, 1991.

[80] RF Foral. Delamination failures in curved composite laminates. In *Key Engineering Materials*, volume 37, pages 137–148. Trans Tech Publ, 1989.

[81] C Marco-Ayala, CJ Marco, and E Salete. New formulas for calculating mode ii fracture energy of several typologies of grp pipes under impact. *Composites Part B: Engineering*, 92:242–251, 2016.

[82] Lucas L Vignoli, Marcelo A Savi, Pedro MCL Pacheco, and Alexander L Kalamkarov. Micromechanical analysis of transversal strength of composite laminae. *Composite Structures*, 250:112546, 2020.

[83] Y Cao, W Wang, and Q Wang. Application of mechanical model for natural fibre reinforced polymer composites. *Materials Research Innovations*, 18(sup2):S2–354, 2014.

[84] Pal Bhaskar and Riyazuddin Haseebuddin Mohamed. Analytical estimation of elastic properties of polypropylene fiber matrix composite by finite element analysis. *Advances in Materials Physics and Chemistry*, 2012, 2012.

[85] Sanjay Palsule, BO Ogunsile, Anshu Anjali Singh, et al. Natural hardwood fiber reinforced chemically functionlized polyethylene composites with in-situ fiber/matrix interfacial adhesion. *Applied Polymer Composites*, 1(1):57–74, 2013.

[86] Pattabhi Ramaiah Budarapu, Xiaoying Zhuang, Timon Rabczuk, and Stephane PA Bordas. Multiscale modeling of material failure: Theory and computational methods. *Advances in Applied Mechanics*, 52:1–103, 2019.

[87] Yakov Benveniste. A new approach to the application of mori-tanaka's theory in composite materials. *Mechanics of materials*, 6(2):147–157, 1987.

[88] John Douglas Eshelby. The determination of the elastic field of an ellipsoidal inclusion, and related problems. *Proceedings of the royal society of London. Series A. Mathematical and physical sciences*, 241(1226):376–396, 1957.

[89] Pedro Ponces Camanho. Failure criteria for fibre-reinforced polymer composites. *Secção de Mecânica Aplicada, Departamento de Engenharia Mecânica e Gestão Industrial, Faculdade de Engenharia da Universidade do Porto*, 2002.

[90] CT Sun. Strength analysis of unidirectional composites and laminates. 2000.

[91] Chun Hui Wang and Cong N Duong. *Bonded joints and repairs to composite airframe structures*. Academic Press, 2015.

[92] Stephen W. Tsai and José Daniel D. Melo. *Composite Materials Design and Testing*. JEC Group, 2015.

[93] Pedro P Camanho and Stephen R Hallett. *Numerical modelling of failure in advanced composite materials*. Woodhead Publishing, 2015.

[94] Umar Farooq and Peter Myler. Ply level failure prediction of carbon fibre reinforced laminated composite panels subjected to low velocity drop-weight impact using adaptive meshing techniques. *Acta Astronautica*, 102:169–177, 2014.

[95] MJKA Hinton, PD Soden, and Abdul-Salam Kaddour. *Failure criteria in fibre reinforced polymer composites: the world-wide failure exercise*. Elsevier, 2004.

[96] Amedeo Grasso. *Implementation of classical and advanced failure criteria for composite layered structures in FEMAP and assessment of results*. PhD thesis, Politecnico di Torino, 2018.

[97] ST Pinho, R Darvizeh, P Robinson, C Schuecker, and PP Camanho. Material and structural response of polymer-matrix fibre-reinforced composites. *Journal of Composite Materials*, 46(19-20):2313–2341, 2012.

[98] Torayca. High-strength and high-modulus carbon fibre torayca t1100g. Available at https://www.torayca.com/en/download/pdf/torayca_t1100g.pdf, Accessed last time in March 2021.

[99] PA ASTM International, West Conshohocken. Astm d6272-17e1, standard test method for flexural properties of unreinforced and reinforced plastics and electrical insulating materials by four-point bending. Available at http://www.astm.org/cgi-bin/resolver.cgi?D6272-17e1, 2017.

[100] Puneet Saggar. Experimental study of laminated composite tubes under bending. 2007.

[101] Zengqin Yang, Hui Wang, Xiaofei Ma, Fulin Shang, Yu Ma, Zhenwei Shao, and Demen Hou. Flexural creep tests and long-term mechanical behavior of fiber-reinforced polymeric composite tubes. *Composite Structures*, 193:154–164, 2018.

[102] David Ramos Benfica de Melo. Composite structures impact simulation behavior. 2014.

[103] Saeid Khadem Moshir, Suong V Hoa, Farjad Shadmehri, Daniel Rosca, and Ashraf Ahmed. Mechanical behavior of thick composite tubes under four-point bending. *Composite Structures*, 242:112097, 2020.

[104] Granta Design Limited. Granta edupack software, Cambridge, UK 2020.

[105] PA ASTM International, West Conshohocken. Astm d695-15, standard test method for compressive properties of rigid plastics. Available at http://www.astm.org/cgi-bin/resolver.cgi?D695, 2015.